Fabrizio Aloschi

Analysis of nonlinear metamaterials and metastructures for mitigation and control of elastic waves

Ph.D. Thesis

UNIVERSITÀ DI TRENTO

UNIVERSITY OF TRENTO - Italy
Department of Civil, Environmental and Mechanical Engineering

Doctoral School in Civil Environmental and Mechanical Engineering
Modelling and simulation - Cycle XXXV
2019/2022

ANALYSIS OF NONLINEAR METAMATERIALS AND METASTRUCTURES FOR MITIGATION AND CONTROL OF ELASTIC WAVES

Ph.D. Candidate:
Fabrizio Aloschi

Supervisor:
Prof. Oreste S. Bursi

University of Trento
Doctoral School in Civil, Environmental and Mechanical Engineering
http://web.unitn.it/en/dricam
Via Mesiano 77, I-38123 Trento
Tel. +39 0461 282670 / 2611 - dicamphd@unitn.it

Acknowledgements

First and foremost, I would like to express my sincere gratitude to my advisor, Prof. Oreste Bursi, for providing invaluable guidance throughout my PhD journey. I could not have hoped for someone better. Your reprimands have certainly kept me on my toes, but I will not forget the valuable lessons I have learned from them.

I extend my heartfelt thanks to Prof. Antonio Palermo and Prof. Chiara Daraio, for their brilliant insights and stimulating discussions. I also express my thanks to Dr. Günter Fischbach for providing me with all the necessary resources and for placing a great deal of trust in me.

I am tremendously grateful to the guys from Trento and the Caltech group for their collaboration and support. I will not name anyone, nor will I thank family and friends in this formal context, as there are too many of you and too few words to express my gratitude in a meaningful way.

On a more serious note, I would like to acknowledge all those who tirelessly fight and struggle to uncover the truth. I hope to one day contribute to this pursuit myself.

Abstract

The mechanical and structural engineering community are increasingly resorting to the use of periodic metamaterials and metastructures to mitigate high amplitude vibrations; and nonlinearities are also an active area of research because they potentially provide different methods for controlling elastic waves. While the theory of propagation of linear elastic waves seems to be fairly complete and has led to remarkable discoveries in a variety of disciplines, there is still much to investigate about nonlinear waves, both in terms of their dispersion analytical description and their numerical characterization. This thesis mainly relies on the latter aspect and focuses on the analysis of nonlinear metamaterials and metastructures for both the mitigation and control of elastic waves. In particular, the thesis covers four main topics, each associated with a different nonlinearity: i) dispersion curves and mechanical parameters identification of a weakly nonlinear cubic 1D locally resonant metamaterial; ii) manipulation of surface acoustic waves (SAWs) through a postbuckling-based switching mechanism; iii) seismic vibration mitigation of a multiple-degrees-of-freedom (MDoF) system, the so-called metafoundation, by means of hysteretic nonlinear lattices; iv) seismic vibration mitigation of a periodic coupled system pipeline-pipe rack (PPR), by means of a vibro-impact system (VIS).

To identify the dispersion curves of a cubic nonlinear 1D locally resonant metamaterial, a simple experimentally-informed reference subsystem (RS) which embodies the unit cell is employed. The system identification relies on the Floquet–Bloch (FB) periodic conditions applied to the RS. Instead, the parametric identification is carried out with a revised application of the subspace identification (SSI) method involving harmonic, non-persistent excitation. It is remarkable that the proposed methodology, despite the linearization caused by the FB boundary conditions, is responsive to the amplitude of the excitation that affects the dispersion curves. The FB theorem, in fact, is often adopted to reduce the computational burden in calculating the dispersion curves of metamaterials.

In contrast, the experimental dispersion reconstruction requires multiple velocity measurements by means of laser Doppler vibrometers (LDVs), as for the case of SAWs. To manipulate SAWs, a proof-of-concept experiment was performed for a postbuckling-based mechanical switching mechanism. Precompressed beams are periodically arranged on one face of an elastic plate to manipulate the dispersion of the SAWs propagating as edge waves. By compressing the columns over their Euler critical load, in fact, it is possible to manipulate the surface wave dispersion: the dispersion curve's dispersive branches, originally caused by the beams in the undeformed configuration, are cleared, and the original path of the group velocity is restored. This concept is introduced analytically and numerically in this thesis, and a novel device is proposed for controlling the SAWs.

With regard to the mitigation of seismic waves, this thesis presents the application of two nonlinear dissipative devices to periodic components and structures of industrial facilities. Firstly, a finite locally resonant metafoundation of an MDoF fuel storage tank is equipped with fully nonlinear hysteretic devices to mitigate absolute accelerations and displacements in the low-frequency regime. Secondly, for mitigating the vibrations in PPRs, spatial periodicity and internal damping are combined to obtain an enhancement in the attenuation rate of the system. At the same time, the seismic performance of the PPR is improved by means of an external nonlinear VIS. These investigations show the characterization of the structures' responses due to the stochastic nature of the input; and for the case of the VIS, a chaotic behavior is sometimes observed and demonstrated.

In conclusion, this thesis investigates the nonlinear response of different periodic structures and their potential for wave control and mitigation in various applications. The results of this research contribute to the understanding of the nonlinear behavior of these periodic structures and provide insights into the design, the optimization, and the identification of metamaterials and metastructures performance.

Publications

Journal Papers

- Francesco Basone, Oreste S Bursi, Fabrizio Aloschi, and Günter Fischbach. Vibration mitigation of an MDoF system subjected to stochastic loading by means of hysteretic nonlinear locally resonant metamaterials. *Scientific reports*, 11(1):1–15, 2021, *doi: 10.1038/s41598-021-88984-0*.

- Fabrizio Aloschi, Roberto Andreotti, Oreste S Bursi. Pipe vibration attenuation through internal damping and optimal design of vibro-impact systems. *Scientific reports*, 13(1):6510, 2023, *doi: 10.1038/s41598-023-33640-y*.

- Fabrizio Aloschi, Oreste S Bursi, Antonio Palermo, Alessandro Marzani. Procedure for the identification of dispersion curves in nonlinear periodic structures. *Journal of Sound and Vibration*, *in preparation*.

- Fabrizio Aloschi, Antonio Palermo, Chiara Daraio. Postbuckling-based mechanical switching of surface acoustic waves; *Applied Physics Letters*, *in preparation*.

Conference Papers

- Fabrizio Aloschi, Oreste S Bursi. A novel identification procedure of mass-in-mass metamaterials endowed with cubic oscillators. *EMI 2022 – Engineering Mechanics Institute Conference 2022*, Baltimore, Maryland (USA).

- Fabrizio Aloschi, Roberto Andreotti, Oreste S Bursi. Optimal design of impact-based nonlinear energy dissipation mechanism in pipeline systems. *ENOC2022 – 10^{th} European Nonlinear Dynamics Conference*, Lyon, France.

- Fabrizio Aloschi, Brian Kim, Oreste S Bursi, Chiara Daraio. Postbuckling-based mechanical switching for the propagation of surface acoustic waves. *MIMS2022 – 2022 International Workshop on Multiscale Innovative Materials and Structures*, Cetara, Italy.

- Fabrizio Aloschi, Oreste S Bursi, Antonio Palermo, Alessandro Marzani. Dispersion analysis of periodic structures by performing experimental Floquet-Bloch conditions to the unit-cell. *EACS 2020 - 7th European Conference on Structural Control*, Warsaw, Poland.

Deliverables/Milestones/Others

- Fabrizio Aloschi, Miltiadis Kontogeorgos, Maria Antoniou, Robine Sabat, Slimane Ouakka, Moris Kalderon, Ioannis Antoniadis, Marianna Loli. Report on the progress of ERS10, ERS11, ERS12, ERS13, ERS14, and ESR15 at the end of first, second and third year. *Deliverables D4.2, D4.10 and D4.11*, **ITN-INSPIRE**.

- Fabrizio Aloschi, Oreste S Bursi, Marianna Loli. Design of a metamaterial concept for pipes and associated structures - Final report. *Deliverable D4.3*, **ITN-INSPIRE**.

Teaching activities

- Fabrizio Aloschi, Oreste S Bursi, 2nd Online International Summer School on MECHANICS AND PERFORMANCE OF RESILIENT STRUCTURES AND INFRASTRUCTURES (MECHRES20) - *DICAM - University of Trento*, September 10, 2020, Tutorial-Lecture: Flexural band gaps in periodic piping systems.

List of acronyms or abbreviations

- CCD - Central composite design
- COR - Coefficient of restitution
- CMS - Condensed mass system
- DM - Damage state
- EDP - Engineering demand parameters
- ELT - Equivalent (stochastic) linearization technique
- EoM - Equation of motion
- FB - Floquet–Bloch
- FEM - Finite element model
- FRF - Frequency response function
- ID - Identification
- IM - Intensity measure
- IDA - Incremental dynamic analysis
- LDV - Laser Doppler vibrometer
- MDoF - Multi degree of freedom
- MEMS - Microelectromechanical systems
- PGA - Peak ground acceleration
- PPR - Pipeline periodically supported by rack structure

- PSD - Power spectral density
- PTMD - Pounding tuned mass dampers
- PVC - Polyvinyl chloride
- RS - Reference subsystem
- RSM - Response surface methodologies
- SSE - Safe shutdown earthquakes
- SDoF - Single degree of freedom
- SEREP - System equivalent reduction expansion procedure
- SS - Single span
- SSI - Subspace identification
- SAW - Surface acoustic wave
- THA - Time history analysis
- UHS - Uniform hazard spectrum
- VIS - Vibro-impact system
- WFEM - Wave-finite-element model
- WP - Work package
- WN - White noise
- SNR - Signal to noise ratio
- KTCP - Kanai–Tajimi Clough–Penzien

Contents

List of Figures

List of Tables

1.0 Introduction

The term *metamaterial* was first used in a scientific paper by the Russian physicist Victor Veselago [1] who, in 1968, introduced the concept of materials with negative refractive index for manipulating light and electromagnetic radiation. Analogously, in the early 2000s, the first attempts to apply the concepts of metamaterials to mechanics were devoted to the development of materials with negative Poisson's ratio [2], negative stiffness [3], negative mass density [4], and negative bulk modulus [5], which revealed a tremendous potential in manipulating acoustic and elastic waves; in addition, phononic crystals suggested that the periodic orientation of structures, and the phenomena of local resonance and Bragg scattering, could be exploited to generate bandgaps. And from the very first moment, it was clear that these phenomena could be extended to a broad range of frequencies [6], from the very-high frequency range of ultrasounds to the very ultra-low frequency range of seismic waves. Moreover, the potential of nonlinearities to enhance the control of elastic waves has been gaining attention in recent years. It is believed that incorporating nonlinearities into metamaterials can enhance their effectiveness, both in terms of analysis accuracy and harnessing nonlinear phenomena such as amplitude-gaps [7, 8], solitons [9], multi-resonances [10], bifurcations, and chaos.

1.1 Background and motivation

Within this thesis, a clear distinction can be made between two primary areas of focus: i) the identification and manipulation of dispersion properties in nonlinear periodic structures in free oscillation, and ii) the attenuation of seismic waves using nonlinear finite lattices and metastructures.

Dispersion curves or band structures define the relationship between the temporal frequency of a wave and its spatial frequency, namely the wavenumber. A nonlinearity can cause the dispersion curve to deviate from the linear relationship; this deviation can result in the curve becoming more complex or distorted, possibly exhibiting features which are not present in materials with linear responses [11]. These complexities have brought many researchers to develop analytical methods devoted to the prediction of band structures. Among others, we recall those based

on perturbation methods [12], on the homotopy method [13] and those based on the factorization of the spatial and temporal parts of the solution [14]. Some inconveniences of the existing identification procedures that operate on finite lattices [15, 16, 17], like wave reflections or the need of using perfectly-matched layers, etc., might be avoided with techniques operating on the single unit cell. Obviously, all these methods are based on some approximations, such as those in which the propagation of nonlinear waves is justified by the Floquet–Bloch (FB) condition [18, 19]. Another topic covered in this thesis is the control of elastic waves, with particular regard to the surface acoustic waves (SAWs). SAW is a term used to generally define a type of mechanical wave that propagates along the surface of an elastic solid. Acoustic devices that control the propagation of SAWs range over widely different length scales, from microelectromechanical systems (MEMS) microphones at the microscale, to nanomechanical resonators at the nanoscale, to metabarriers and metasurfaces at the scale of geophysical phenomena such as earthquakes. In many applications, phononic crystals and metamaterials were designed to interact with SAWs [20, 21, 22]. One interesting and relatively recent way to control SAWs is by tuning the medium response via external compression [23, 24, 25, 26]. Truly fascinating, yet not sufficiently explored, is the tunability by using external, noncontact, interaction forces [27]. In addition, the development of acoustic devices analogous to electronic systems like switchers [28], transistors and rectifiers [29], suggests the use of nonlinear phonons to control phonons. For example, Bilal and Daraio [28] realized a phononic transistor-like device that can switch and amplify vibrations with vibrations, i.e., operating in the phononic domain. Geometric or material nonlinearities have been utilized to exploit phenomena such as localization [30], breathers [31], bifurcation, and chaos [29]; the softening induced by buckling, and the consequent amplitude reduction of the frequency response function, might represent a valid alternative due to its ease of realization and versatility.

The second main strand of this thesis examines seismic wave attenuation, which can be considered a branch of passive wave control. Specifically, this thesis focuses on the use of finite lattices and metastructures to reduce high-amplitude vibrations, which has gained significant attention over the last two decades. Early attempts were dedicated to developing novel seismic isolation systems [32] that could attenuate waves from the foundations. Nowadays, a vast literature exists on the so-called metafoundations, metabarriers, and metasurfaces. Metafoundations have been studied for isolating nuclear power plants [33, 34] and high-risk industrial structures [35, 36], including against vertical components of ground motion [37]. Nonetheless, the engineering of metafoundations

can be economically challenging and their installation beneath an existing structure is certainly not feasible. Some researchers investigated the metabarriers [38, 39], which are analogously composed of resonating arrays of unit cells, but are installed next to the foundation rather than beneath it. More precisely, when the resonators are arranged along the surface of an elastic medium, they are said to form a seismic metasurface [40, 41] that, however, is primarily designed to mitigate the effects of surface waves. Although these systems have different applications, they share the same basic principle: the resonant behavior of the masses, and phenomena like mass and stiffness nagativity, or antiresonance, due phase opposition, allow for strong dissipation of seismic energy in a localized area, which drastically reduces the transmission of waves on the structure. In this sense, metafoundations, metasurfaces, and metabarriers can be thought as novel isolation/dissipation systems. In metastructures, on the other hand, the periodic arrangement of unit cells is designed to achieve interference and scattering of incoming waves for specific frequency ranges, known as bandgaps. For example, periodically supported structures like bridges or pipelines can have wide bandgaps [42, 43]. Within these frequency regions, even undamped structures exhibit a significant wave attenuation due to local resonances or Bragg scattering. Nevertheless, conventional passive dissipation systems used for pipes, such as tuned mass dampers (TMDs), are not always recommended for vibration mitigation due to their low performance under certain conditions caused by detuning effects [44]. Moreover, they may not be sufficient to mitigate the abrupt flow-induced increases of velocity and may have limitations in terms of their ability to suppress multiple frequencies [45, 46], and as such, nonlinear systems have become the preferred choice for this purpose.

1.2 Research objectives

Four applications involving nonlinearities are explored in this thesis, including: i) the identification of dispersion characteristics and mechanical properties of a weakly nonlinear cubic 1D locally resonant metamaterial; ii) the control of surface acoustic waves (SAWs) through a postbuckling-based switching mechanism; iii) the reduction of seismic vibrations in a finite lattice metafoundation utilizing hysteretic nonlinear devices; and iv) the application of a vibro-impact system (VIS) for seismic vibration mitigation in a pipeline-pipe rack (PPR) system. All topics are treated starting from the analytical definition of the dispersion properties and the dispersion curves to the numerical validation of the different periodic

systems investigated, with special regard toward the nonlinear effects; regarding the attenuation of seismic waves, finite lattices are utilized, and their dispersion behavior is compared with periodic arrangements.

With regard to i), Chapter 2 shows that the application of FB to nonlinear metamaterials leads to a loss of information about the superharmonics, despite the vast use in literature of such analytical technique for nonlinear systems. Therefore, the proposed identification procedure cannot be performed for the frequencies of higher order, yet it maintains the amplitude dependency of the first harmonic upon the amplitude of the excitation. A simple experimentally-informed reference subsystem (RS) which embodies the unit cell is proposed for applying the FB conditions in displacements control, in order to obtain the numerical/experimental dispersion curve of the infinite periodic metamaterial. The proposed procedure is validated both in the linear and the nonlinear regime; in the latter condition, the wave transmission or FRF of the identified weakly nonlinear cubic metamaterial is compared with the analytical predictions provided by the first-order Lindstedt–Poincaré method. Moreover, the identification of the imaginary part of the wavenumber permits the quantification of the attenuation properties of the analyzed periodic system.

With respect to ii), Chapter 3 proposes a tunable platform made of precompressed beams mounted on one face of an elastic plate to showcase a novel postbuckling-based mechanical switching mechanism for manipulating the dispersion of the SAWs. By compressing the beams over their Euler critical load, in fact, it is possible to manipulate the surface wave dispersion; the dispersion curve's dispersive branches, originally caused by the beams in the prebuckling regime, are cleared, and the original path of the group velocity is restored. This novel postbuckling-based mechanism represents a promising alternative to control SAWs, among other geometric nonlinearities, due to its ease of realization and reversible nature. Shifting between prebuckling and postbuckling without inducing plastic deformation allows for greater control and versatility.

Concerning iii), Chapter 4 treats the usage of nonlinear hysteretic devices to enhance the attenuation capacity of an MDoF metafoundation system. In this context, nonlinear features highlight the need for additional techniques to take into account the dependency of the metafoundation's dispersion characteristics upon the intensity of the seismic event. A novel analytical dispersion analysis that considers the intensity of the stochastic input is developed in combination with the stochastic linearization technique: in the frequency domain, the records are modeled with the power spectral density (PSD) S_0 and modified with a Kanai–Tajimi filter, and the dispersion relations of the relevant periodic metafoun-

dation are dependent upon S_0. A good comparison between the dispersion of the linearized periodic metafoundation and the FRF of the nonlinear finite lattice is also observed in terms of attenuation zones.

With respect to iv), a PPR is investigated in Chapter 5: it presents large bandgaps due to local resonances and Bragg scattering and its attenuation rate is further increased through the use of internal material damping. Moreover, Chapter 5 investigates an alternative nonlinear impact-based dissipation system called a VIS: two bumpers rigidly connected to the ground constrain the amplitude displacement of the pipe. Chapter 5 presents a new optimization procedure that maximizes the seismic performance of the VIS and minimizes the seismic risk associated with exceeding a certain number of impacts.

1.3 ITN-INSPIRE

The topics covered in this thesis have been developed within the framework of the Marie Skłodowska-Curie ITN-INSPIRE research and innovation program; this ambitious project aimed to foster a new generation of researchers and engineers through an ensemble of research, training and dissemination actions. As a whole, the research aimed to implement a holistic and novel soil-foundation-structure concept for the efficient protection of structures from all ground-induced hazards, including earthquakes and all other sources of low-frequency noise and vibration excitations.

From a management point of view, the INSPIRE training program has equipped researchers with innovative and creative skills and has implemented a joint multidisciplinary research training program focused on the growth of scientific and technological knowledge and professional skills through research on individual and personalized projects. The project also aimed to improve the European innovation capacity as each one of the eleven participating companies had directly supported a specific high-impact technological application; we believe that in the near future some of these applications can lead to new technological products or patented design concepts for structure protection, tools and procedures in a market the global size of which is expected to reach USD 11.72 trillion by 2025. To date, we can certainly claim that INSPIRE has created a legacy for the future generations of researchers, with training material and relationships with companies that offered secondment opportunities for further cohorts of students outside of the project. Furthermore, apart from their research and development leadership in Europe, the Fellows have maintained their connection to the program by developing parallel

training for researchers in their organization and, in some cases, even made this program part of the graduate training scheme for industrial partners.

From the perspective of research, the key concept investigated in the project is that of metamaterials: the project specifically targeted the peculiarities of those artificial materials or structures generated by periodically repeated unit blocks, to exhibit and exploit properties for inhibiting and controlling wave propagation in all spatial directions over broad frequency bands. To reach these targets, three work packages were dedicated to research: i) WP2 - "METASOIL", Design and demonstration of novel metamaterial concepts for wave mitigation in soil; ii) WP3 - "METABASES", Design and demonstration of novel structure support and foundation concepts; iii) WP4 - "METASTRUCTURES", Design and demonstration of novel integrated design concepts for innovative high impact applications. Specifically, several investigations have been carried out to develop novel anti-vibration protection concepts, new techniques for the control of elastic waves, or wave conditioning, and to envisage novel metastructures. Pile arrays and foundation blocks were developed to trap low frequency waves and to have wide bandgaps. Efthymiou and Vrettos [47] investigated the potential reduction of vibrations caused by moving loads in the vicinity of pile group foundations for different layout geometries. They found out that the pile group reduced the free-field vibrations mainly due to the redirection of the energy toward greater depths and as a result of the wave diffraction through the front pile rows. Instead, Kanellopoulos et al. [48] propose resonant metamaterials, as a metabarrier, for mitigating the effect of vertically propagating seismic shear waves in nonlinear soil.

A novel concept for redirecting elastic waves in the soil is that of cloak. Chatzopoulos, Palermo and Marzani [49] are investigating cloaking strategies for controlling Love waves; and in the same lab, Pu [41, 50, 51, 52] produced a remarkable number of useful analyses of metamaterials for the seismic surface wave mitigation: interactions between Rayleigh waves and metasurfaces in real site conditions have been analytically defined [41]; in [51, 52], ad-hoc multiple scattering formulations are adopted to this aim. Nevertheless, metasurfaces have been used also for the purpose of sound isolation: Sabat and Pennec [53] employed Helmholtz resonators to manipulate the sound at targeted frequencies and demonstrated the coupling between sub-wavelength units. A class of novel absorption and isolation concepts have been investigated, like negative stiffness dampers [54, 55], directional inertial amplifiers [56], micro-structured materials under buckling [57, 58] and Rocking-like motion [58]. Kalogerakou et al. [54] propose a vertical stiff dynamic ab-

sorber combined with a quasi-zero stiffness design and introduce a design method based on a general objective function that is independent on the specific excitation spectrum; instead, Mantakas and Antoniadis [55] propose the use of a negative stiffness-based passive vibration absorber for seismic retrofitting purposes. To obtain an artificial increase of the inertia which results in an amplification of the resonant properties of locally resonant metamaterials, Kalderon et al. [56] investigated a simple dynamic directional amplification mechanism realized by imposing kinematic constraints to the model's degrees of freedom. All the works produced in this framework [54, 55, 56] have confirmed an enhancement in wave damping, but also an enlargement of the bandgaps, especially for seismic and low-frequency acoustic applications. In this framework, Chondrogiannis, Dertimanis and Chatzi [59] show the potential of a geometrically nonlinear design for lowering of the low-frequency bandgaps. With regard to micro-structured materials, Koutsogiannakis, Bigoni and Dal Corso [57] propose an innovative structural system that is based on tensile and compressive buckling of an elastic rod. This novel system can be envisaged as a passive mechanical system encompassing multistable behavior, with possible applications in the field of force-limiters and soft mechanisms. In the same lab, and with purpose of vibration attenuation and energy harvesting, Hima [58] investigated an elastic planar metainterface that showed strong similarities with the rocking motion of rigid blocks.

There exist many ground-borne vibrations in the structures, and in a very interesting review article Ouakka [60] reported on the ones coming from the rail transit systems and described the different mitigation systems reported in the literature; but certainly seismic events have gained more attention, and in the thread of seismic wave attenuation, the ITN-INSPIRE has envisaged novel paradigms for the protection of structures, like metafoundations for industrial facilities [61], or metapipes [62, 63] for long distributed components. Aloschi and Bursi [61] employed hysteretic nonlinear resonant metamaterials at the base of MDoFs to mitigate vibrations induced by stochastic loadings; and to mitigate vibrations in pipelines and pipe-racks, Aloschi [62] investigated a vibro-impact system (VIS) applied to the interface of an unburied pipe. Kontogeorgos [63], instead, reported on preliminary studies about the concept of metamaterials for the protection of buried gas transmission pipelines. Finally, Antoniou and Anastasopoulos [64] combined the actions of earthquakes and wind, and studied the performance of offshore wind turbines founded on suction bucket jackets in clay.

1.4 Thesis organization

The thesis is organized as follows.

Chapter 2 is dedicated to a novel identification procedure for determining the dispersion curves and mechanical parameters of a cubic nonlinear resonant metamaterial. The research was carried out in collaboration with Antonio Palermo and Alessandro Marzani from the University of Bologna within the ITN-INSPIRE project. Firstly, the model problem, namely the RS, is introduced, and the premises of the identification procedure are elucidated. Then, the identification of the dispersion curves for a linear undamped resonant metamaterial is discussed, with the aim of describing the basic concepts of the identification procedure using a simple undamped application. Damping and nonlinearity are then considered, and the related identification method is validated.

Chapter 3 is dedicated to the manipulation of SAWs. The concept of postbuckling-based mechanical switching is introduced within the context of the existing literature. The results of a computer simulation and a wave-finite-element model (WFEM) are then discussed to validate the proposed device. The device was conceived in collaboration with Antonio Palermo, Brian Kim, and Chiara Daraio, and partially tested at Daraio's LAB at the California Institute of Technology (CalTech), Pasadena.

Chapter 4 reports a publication for *Scientific reports*, titled *Vibration mitigation of an MDoF system subjected to stochastic loading by means of hysteretic nonlinear locally resonant metamaterials*, authored by *Fabrizio Aloschi, Oreste S. Bursi, Francesco Basone,* and *Günter Fischbach*. After introducing the structural model of the nonlinear metafoundation and the Bouc–Wen model for the nonlinear hysteretic devices, Chapter 4 elucidates the stochastic linearization technique applied to the nonlinear differential equations of the Bouc–Wen model. The metafoundation is then optimized to minimize the interstorey displacement and absolute acceleration of the upper structure. The optimized system is verified against natural seismic records by means of nonlinear transient time history analyses, and these numerical results are compared with the dispersion relations of the relevant periodic metafoundation.

Chapter 5 reports a further publication for *Scientific reports*, titled *Pipe vibration attenuation through internal damping and optimal design of vibro-impact systems*. The work was carried out in collaboration with Roberto Andreotti from the University of Trento and concerned an industrial metapipe periodically supported by a pipe rack (PPR). Internal material damping and external viscous damping are introduced; the former is applied to the analytical model of the metapipe to show an enhancement of the attenuation rate of the periodic system. A single span

of the infinite periodic metapipe is then provided with a vibro-impact device (VIS). A design optimization procedure is set to maximize the dissipation energy and minimize the number of impacts of the VIS. All optimization results, as well as a fragility assessment of the metapipe performed through incremental dynamic analysis (IDA), are presented and discussed.

Chapter 6 provides conclusions in terms of a discussion about the results and critical issues, along with future perspectives.

Finally, this dissertation includes three appendices that provide supplementary information for the work described in the preceding chapters. Appendix A offers additional details about the identification procedure presented in Chapter 2. Specifically, Appendix A.1 provides a detailed explanation of the perturbation approach, while Appendix A.2 demonstrates a simple example of identifying a linear damped metamaterial and revises the subspace identification (SSI) technique for identifying the nonlinear stiffness of a cubic nonlinear metamaterial. Appendix B describes the calculation of the transfer function of the nonlinear hysteretic resonator for the metafoundation discussed in Chapter 4. Lastly, Appendix C reports a few chaotic trajectories of the VIS investigated in Chapter 5 to prove the existence of chaos with positive Lyapunov exponents.

2.0 Dispersion curves and mechanical parameters identification of metamaterials based on a discrete reference subsystem

This chapter contains the pre-print of:

Fabrizio Aloschi, Oreste S Bursi, Antonio Palermo, and Alessandro Marzani. Procedure for the identification of dispersion curves in nonlinear periodic structures; in preparation for *Journal of Sound and Vibration*,

as it will be submitted for the Journal *Journal of Sound and Vibration*, differing only in terms of layout and formatting.

A procedure for identifying the dispersion curves for linear and nonlinear one-dimensional locally resonant periodic systems is here proposed. The procedure exploits the application of Floquet–Bloch (FB) boundary conditions to a reference subsystem (RS) extracted from the periodic structure. The dispersion curves (frequency vs. wavenumbers) are estimated from the computation of the frequency response functions (FRFs) of the subsystem for different wavenumbers in the input. The proposed procedure is applied and validated on a mono-dimensional mass-in-mass chain equipped with linear and nonlinear springs. In the latter scenario, the identification procedure is responsive to the amplitude of the excitation, which affects the dispersion curves. The proposed method is particularly suitable for the experimental characterization of periodic materials because it exploits a single measurement point to identify FRF based dispersion curves. The identification procedure is completed with an application of the subspace identification (SSI) method, reported as supplementary material, to identify the nonlinear stiffness parameter.

2.1 Introduction

In recent years, both mechanical and structural engineering communities have proposed the use of periodic metamaterials or systems to mitigate the effects of low-frequency vibrations [65, 39, 61]. Periodic and locally resonant structures support the propagation of waves with strong dispersive features, namely with wave speeds; therefore, wavenumbers that significantly change with the frequency of excitation eventually lead to frequency band gaps [66, 67, 68]. Therefore, methods that allow for the identification of wave dispersion and attenuation are critical for the experimental characterization of these structures [69].

This need is more evident for nonlinear periodic media, which have garnered the attention of researchers only in the last decade. For such periodic structures, a number of approximate analytical methods have been devoted to the prediction of band structures. Among others, we recall those based on perturbation methods [12], the homotopy method [13] and the factorization of the spatial and temporal parts of the solution [14]. The aforementioned methods are advantageous because they provide analytical solutions that can be easily compared with numerical predictions in the validity range of linearization.

Alternatively, the dispersion properties of nonlinear metamaterials can be computed from the numerical responses of finite lattices. In particular, several methods employ the integration of the equations of motion (EoM) of sufficiently long finite chains, eventually employing absorbing boundaries to avoid wave reflection. Fang et al. [70] compared the results of numerical simulations with predictions obtained from the harmonic averaging approach and Lyapunov exponents. Additionally, they computed a linearized estimation obtained by applying the Floquet–Bloch (FB) theorem [71]. Indeed, the FB theorem is a classical tool for computing dispersion curves in periodic 1D, 2D, and 3D periodic systems [72, 73]. The FB theorem was also used by Campana et al. [19] in the context of nonlinear systems; they computed the dispersion relationships of a linearized periodic structure using a first-order perturbation approach.

In addition to the aforementioned methodologies (analytical and numerical) for computing the dispersive properties of periodic structures, only a few tools are available to identify wavevectors and dispersion curves from experimental/numerical responses of linear finite lattices [15, 16, 17]. For example, Junyi et al. [74] developed an inverse method to calculate the band structure of 1D periodic structures. The method is based on FB periodic conditions and employs the superposition of forward and back waves. The solution of the wavevectors was obtained by

solving a polynomial equation derived from the solution of a system of EoMs. Similarly, Zhang et al. [75] used system identification to calibrate an FE model of a periodic structure by exploiting free-wave characteristics to solve a least-squares problem.

Thus, to the best of our knowledge, the identification of dispersion curves for linear and nonlinear periodic systems deserves further study. Hence, we propose a reliable numerical method based on FRF data provided by a reference subsystem (RS) to define the dispersion laws of periodic linear and nonlinear resonant metamaterials. In particular, we employ a reference subsystem extracted from a mass-in-mass spring chain to represent the archetype of an experimentally informed model. In this respect, the FB periodic conditions are applied to the relevant RS, and the identification of the dispersion curves that include the imaginary part of the wavenumber is accomplished using peculiar FRFs. Although the discrete mass-in-mass system may appear simple, the generality of both the FRF and FB techniques allows for a straightforward extension to more complex periodic systems.

2.2 System identification strategy

The model under consideration is an infinite chain of mass-in-mass units with an external mass m encasing a resonating mass m_R connected by means of a damper c_R and spring k_R, as shown in Fig. 2.1 (a). An RS, consisting of a single mass-in-mass and connecting springs k and dampers c, is highlighted in Fig. 2.1 (b). Both the linear k and nonlinear k_{NL} springs were considered. The elastic internal force F between the two adjacent external masses is assumed as follows:

$$F(\delta_i) = k\,\delta_i + k_{NL}\delta_i^3 \tag{2.1}$$

where $\delta_i = u_{n\pm1} - u_n$ denotes the relative displacement between the two masses. The u_n displacement of the n^{th} external mass can be written as [76]

$$u_n(t) = U(\kappa,\omega)\; exp\big[i(n\kappa d + \omega t)\big], \tag{2.2}$$

where ω is the circular frequency of the harmonic motion, κ is the wavenumber, U is the amplitude of the wave motion at a specific wavenumber and frequency, d represents the distance between the unit cells, and i is the imaginary unit.

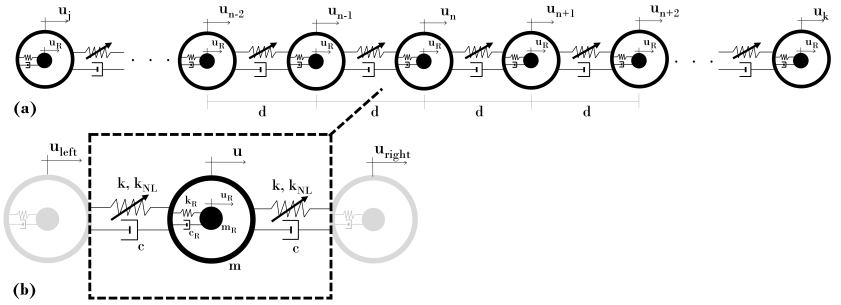

Figure 2.1: (a) 1D mass-in-mass nonlinear monoatomic system, and (b) reference subsystem (RS) delimited by the dashed rectangle.

The exponential term defines the periodicity of the solution in space and time, as $|exp\big[i(n\kappa d+\omega t)\big]| \leq 1$ [71]. The real part of the wavenumber describes the phase change as the wave propagates from one mass to the next, whereas its imaginary part defines the amplitude decay of the wave.

To replicate the dynamics of the infinite chain using an RS, we impose FB boundary conditions on the left- and right-hand bounds of the RS, namely, $u_{n-1} = u_{left}$ and $u_{n+1} = u_{right}$, as shown in Fig. 2.1 (b), and monitor the displacement output of the reference mass $u_n = u$. Indeed, when the cubic nonlinearity in (2.1) is significant, the application of the FB conditions to the RS, as depicted in Fig. 2.1 (b) is roughly accurate; however, its effects are much less severe than expected for large-amplitude waves, as it will be shown in Section 2.4.

The identification of the 1D mass-in-mass dispersion curve is based on the FRF of the RS excited by imposed displacements of the FB type. According to (2.2), the output displacement $u(t)$ should fulfill the following conditions:

$$u(t) = u_{left}(t)\, exp(i\kappa d) = u_{right}(t)\, exp(-i\kappa d), \tag{2.3}$$

From Eq.(2.3), we derive a system of equations.

$$\begin{cases} FRF_{left} = \dfrac{U}{U_{left}} = exp(i\kappa_r d)\, exp(-\kappa_i d) \\ \\ FRF_{right} = \dfrac{U}{U_{right}} = exp(-i\kappa_r d)\, exp(\kappa_i d) \end{cases} \tag{2.4}$$

where κ_r and κ_i are the real and imaginary part of the wavenumber, respectively. U_{left} and U_{right} are the amplitudes of the displacements imposed on the left and right boundaries of the RS that satisfy (2.2).

Consequently, the transmission ratios of (2.4) describe the output of a one-dimensional infinite periodic chain.

In summary, we can identify the dispersion curves of an infinite 1D mass-in-mass system with unknown parameters using a simple RS. As shown in detail in Section 2.4, to identify a nonlinear system, we solve the system of equations (2.4), which can be further simplified when a linear undamped system is identified, as shown in the following. Similarly, the parametric identification of the linear system is a straightforward process that only requires solving a linear system of four equations, while identifying the parametric nonlinear stiffness requires a revised application of the subspace identification technique (SSI), which is detailed in Appendix A.2.

2.3 Case of linear undamped systems

This section reports on the application of the proposed method to linear undamped 1D chains. The RS of interest is shown in Fig. 2.2.

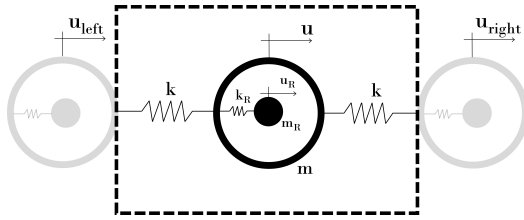

Figure 2.2: Reference subsystem (RS) for a linear resonant undamped 1D chain.

The equations of motion (EoM) for the external mass and resonator are as follows:

$$\begin{cases} m\ddot{u} + k\big(2u - u_{left} - u_{right}\big) + k_R\big(u - u_R\big) = 0 \\ m_R\ddot{u}_R + k_R\big(u_R - u\big) = 0 \end{cases} \tag{2.5}$$

where u and u_R denote the displacements of the external mass m and resonator m_R, respectively; k and k_R are the stiffnesses; and the dot indicates the derivative with respect to time. Based on the FB boundary conditions, the imposed displacements u_{left} and u_{right} are selected as follows:

$$u_{left} = U_{left}\, exp(i\bar{\omega}t), \tag{2.6}$$

$$u_{right} = u_{left}\, exp(2i\bar{\kappa}d), \tag{2.7}$$

where U_{left} is the amplitude of the imposed motion and $\bar{\kappa}$ and $\bar{\omega}$ are the input wavenumber and circular frequency, respectively; d is the distance

between the unit cells. For an undamped periodic system, the wavenumber is real in the passband, with no amplitude decay, and purely imaginary in the bandgap. Therefore, the identifying propagating waves requires finding the frequency $\bar{\omega}$ for which the output satisfies the following equations:

$$\begin{cases} \left|FRF\right| = \left|\frac{U}{U_{left}}\right| = \left|exp(i\bar{\kappa}d)\right| = 1 \\ \Delta\phi = \tan^{-1}\frac{\Im(U/U_{left})}{\Re(U/U_{left})} = \bar{\kappa}d \end{cases} \tag{2.8}$$

where U is the amplitude of the output and $\Delta\phi$ the relative phase between the left input displacement and the output.

Thus, the dispersion curves can be identified according to the following steps:

- Step I: the RS is excited in displacement control with (2.6) and (2.7) for a fixed amplitude U_{left}, a given $\bar{\kappa}$ and a first trial frequency $\bar{\omega}$, selected to be close to zero;
- Step II: the output amplitude U is evaluated in the steady state regime, and the ratio $|\frac{U}{U_{left}}|$ is then computed;
- Step III: Steps I and II are repeated for increasing values of $\bar{\omega}$ until the first solution to (2.8) is found. This solution ($\bar{\kappa}$, $\bar{\omega}$) lies on the acoustic branch;
- Step IV: the input frequency $\bar{\omega}$ is further increased, and Step III is repeated until a second solution that satisfies (2.8) is found. The second solution ($\bar{\kappa}$, $\bar{\omega}$) lies on the optical branch;
- Step V: Steps I–IV are repeated for the desired $\bar{\kappa}$ in the range $0, \pi/d$.

A short sampling value of $\bar{\omega}$ is recommended to avoid the accidental passage of the acoustic or optical branch. Note that the two branches can be discriminated by considering the relative phase between the external mass and resonator; the two masses vibrate in-phase along the acoustic branch and in the antiphase along the optical branch.

Once the dispersion curves are obtained, parameter identification of the linear chain is straightforward. In particular, each point of the dispersion curve $\bar{\kappa} - \bar{\omega}$ satisfies the following eigenproblem:

$$det(\mathbf{K}(\bar{\kappa}) - \bar{\omega}^2\mathbf{M}) = 0, \tag{2.9}$$

where $\mathbf{K}(\bar{\kappa})$ is the wavenumber-dependent stiffness matrix of the linear infinite lattice and $\mathbf{M}$ is the mass matrix [66]. Therefore, it is possible to identify the four unknown mechanical parameters of the system, namely, m, m_R, k, and k_R, by solving a system of four equations (2.9):

$$det\left(\begin{bmatrix} 2k^{ID}\big(1 - cos\,(\bar{\kappa})\big) + k_R^{ID} & -k_R^{ID} \\ -k_R^{ID} & k_R^{ID} \end{bmatrix} - \bar{\omega}^2 \begin{bmatrix} m^{ID} & 0 \\ 0 & m_R^{ID} \end{bmatrix} \right) = 0, \tag{2.10}$$

where the upper script, *ID*, denotes the parameters to be identified. Consequently, we retrieved a system of four equations for the four unknowns m^{ID}, m_R^{ID}, k^{ID} and k_R^{ID}.

2.3.1 Application

The mechanical properties of RS are shown in Fig. 2.2: $m = 2450\,\text{kg}$, $k = 155\,\text{kN/m}$, $m_R = 3170\,\text{kg}$, $k_R = 1080\,\text{kN/m}$, $d = 1\,\text{m}$. These values describe the system investigated by Zivieri et al. [14] for an increase in the masses. To compare the numerical results of the identification, the FRF of the system of interest was obtained in closed form by combining Eqs. (2.6) and (2.7) with the linear system of EoMs (2.5):

$$FRF = \frac{k\,(1 + e^{2i\kappa d})}{-m\omega^2 + 2k - \frac{k_R^2}{k_R - m_R\omega^2} + k_R}. \tag{2.11}$$

Analogously, the application of the FB theorem to the EoMs (2.5) and a few manipulations leads to the well-known analytical dispersion relation of a mass-in-mass periodic lattice [66].

The FRF values computed using (2.11) for $\bar{\kappa} = 1$ and $\bar{\kappa} = 2$ rad/m are shown in Fig. 2.3 (a) and (b), respectively. In the same plot, the frequency values $\bar{\omega}$ satisfying (2.8) are marked with circles. As expected, the transmissions shown in Fig. 2.3 (a) and (b) decrease after each resonance, with $FRF \to 0$ for $lim\ \omega \to \infty$. This may be considered as a warning when the optical branch accidentally passes during the identification process. Note also that the wavenumber is nonzero; therefore, the transmission does not equal 1 for a zero frequency. On the other hand, Eq. (2.11) confirms that $\frac{U}{U_{left}} = 1$ for $\omega = 0$ and $\kappa = 0$.

The amplitudes of the transmissions $|\frac{U}{U_{left}}|$ for those solutions that satisfy (2.8) are compared with the analytical $|FRF|$ of (2.11) in Fig. 2.4 (a); the same set of solutions is plotted in Fig. 2.4 (b) in terms of relative phase.

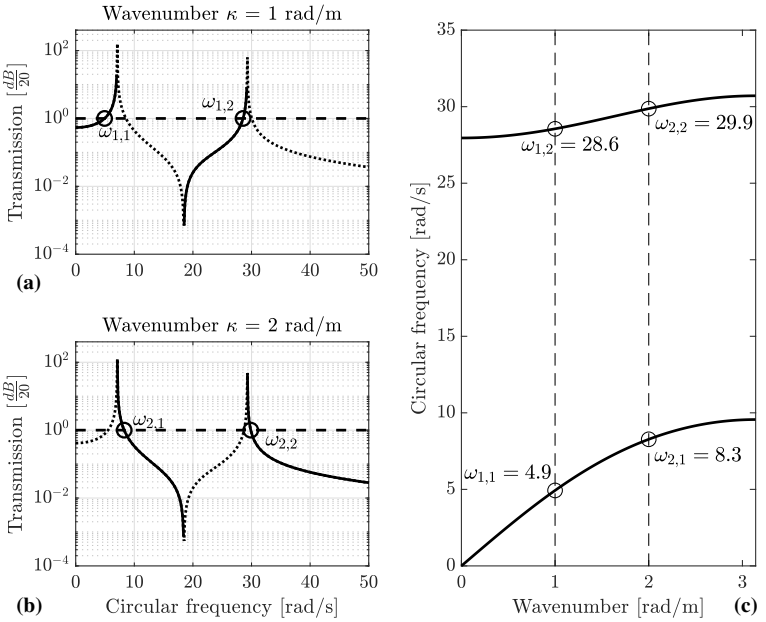

Figure 2.3: Analytical $|FRF|$ (2.11) for (a) a wavenumber $\kappa = 1$ rad/m and (b) a wavenumber $\kappa = 2$ rad/m; (c) analytical dispersion curves of the linear periodic undamped chain. The dotted curves in (a) and (b) indicate the range where $\Im(U) < 0$, whereas the solid lines are for $\Im(U) > 0$. The black circles represent the identified numerical solutions.

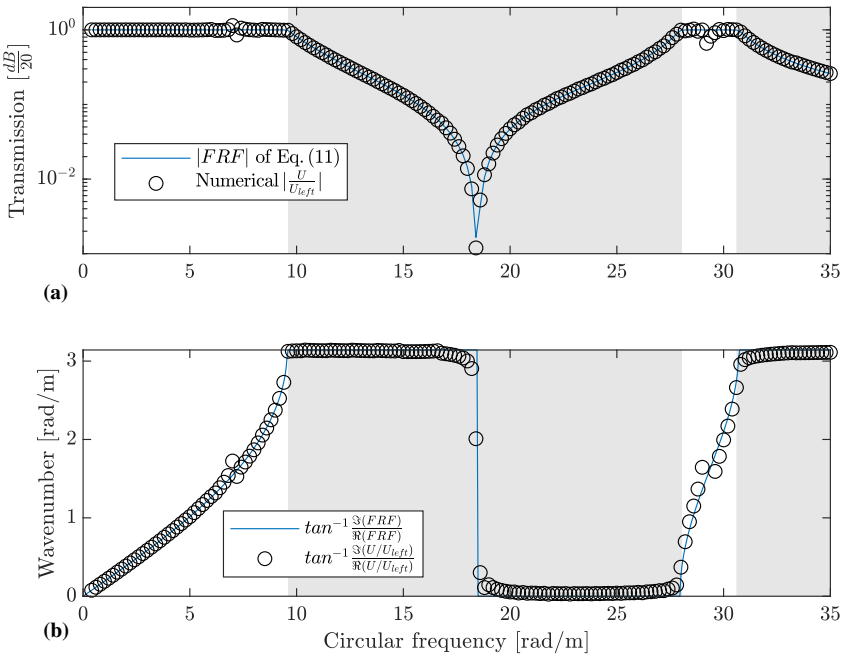

Figure 2.4: Comparison between the analytical and numerical solutions: (a) absolute value of the transmissions, and (b) the relative phases $\Delta\phi$ between the output and the input. The gray areas highlight the bandgaps.

As predicted by (2.8), the transmission is equal to 1 outside the bandgaps, namely where purely propagative waves exist.

Finally, identification of the four aforementioned mechanical parameters completes the linear application. We arbitrarily selected two wavenumbers and the corresponding two pairs of frequencies from the identified dispersion curve; see, for example, the circles in Fig. 2.3 (c). Thus, the inverse eigenproblem of Eq. (2.10) leads us to the identification of four unknowns.

2.4 Case of nonlinear damped system

In this section, we describe the application of the proposed dispersion curve identification procedure to the nonlinear system depicted in Fig. 2.1. For the sake of conciseness, the parametric identification of the linear and nonlinear stiffnesses is reported in Appendix A.2.

The spring nonlinearity is of the cubic-hardening type, as expressed by (2.1), and the relevant RS is depicted in Fig. 2.5.

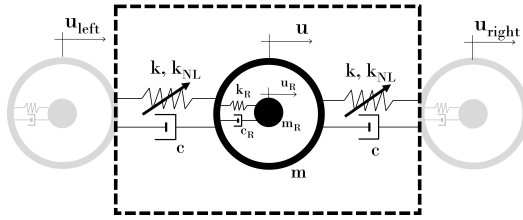

Figure 2.5: Reference subsystem (RS) for the 1D mass-in-mass nonlinear metamaterial.

The system of EoMs reads

$$\begin{cases} m\ddot{u} + c\big(2\dot{u} - v_{left} - v_{right}\big) + k\big(2u - u_{left} - u_{right}\big) + c_R\big(\dot{u} - \dot{u}_R\big) \\ +k_R\big(u - u_R\big) + k_{NL}(u - u_{left})^3 + k_{NL}(u - u_{right})^3 = 0 \\ m_R\ddot{u}_R + c_R\big(\dot{u}_R - \dot{u}\big) + k_R\big(u_R - u\big) = 0 \end{cases} \tag{2.12}$$

where k_{NL} denotes the nonlinear spring constant.

To characterize wave propagation in nonlinear periodic systems, the FB theorem has often been applied to linearized systems [70, 19, 18] with the aim of capturing the fundamental dependency of the dispersion laws on the excitation amplitude [77]. To achieve this, we utilize a procedure devoted to identifying the complex wavenumber $\bar{\kappa} = \bar{\kappa}_r + i\bar{\kappa}_i$ associated with a set circular frequency $\bar{\omega}$ for waves propagating along the nonlinear

chain. Specifically, the input was imposed using Eqs. (2.6) and (2.7) for a given frequency $\bar{\omega}$ and amplitude U_{left}. The dispersion law depends on two unknowns, $\bar{\kappa}_r$ and $\bar{\kappa}_i$. Using (2.4), we derive the following system.

$$\begin{cases} f_1(\bar{\kappa}_r, \bar{\kappa}_i) = \Phi_{left} - exp(i\bar{\kappa}_r d)\, exp(-\bar{\kappa}_i d) \\ f_2(\bar{\kappa}_r, \bar{\kappa}_i) = \Phi_{right} - exp(-i\bar{\kappa}_r d)\, exp(\bar{\kappa}_i d) \end{cases} \tag{2.13}$$

where Φ is the numerical FRF computed as the ratio between the Fourier transform (FT) of the output and input, the subscripts $left$ and $right$ refer to the input, and d is the distance between the unit cells. The Levenberg-Marquardt algorithm was employed to solve (2.13) as a least-squares problem. This optimization algorithm minimizes both f_1 and f_2 by using a search direction that can be considered a combination of the Gauss–Newton direction and the Cauchy steepest descent, and is quite convenient because the Jacobian has full rank at each iteration [78]. The pseudo-code in Fig. (2.6) describes the identification process.

begin
1: **input**: $\bar{\omega}$, U_{left}, first guess ($\bar{\kappa}_{r,0}$, $\bar{\kappa}_{i,0}$), max num of iter (N), tolerance (tol)
2: ***for*** $\bar{\omega} = 0$ to the maximum frequency of interest
3: n←1
4: ***while*** (n ⩽ N)
5: $\Phi_{left} \leftarrow \dfrac{FT\big[u(\bar{\kappa}_{r,n-1},\, \bar{\kappa}_{i,n-1})\big]}{FT\big(u_{left}\big)}$
6: $\Phi_{right} \leftarrow \dfrac{FT\big[u(\bar{\kappa}_{r,n-1},\, \bar{\kappa}_{i,n-1})\big]}{FT\big(u_{right}\big)}$

7: ***if*** (n = N)
8: j←1
9: $\bar{\kappa}_{i,j-1} = \bar{\kappa}_{i,n}$

10: ***while*** (j ⩽ N)
11: $|\Phi_{left}| \leftarrow \left|\dfrac{FT\big[u(\bar{\kappa}_{r,N},\, \bar{\kappa}_{i,j-1})\big]}{FT\big(u_{left}\big)}\right|$
12: ***if*** $\big(\|\nabla f_1(\bar{\kappa}_{r,N}, \bar{\kappa}_{i,j})\|_\infty\big) \leqslant tol$
13: m←1
14: $\bar{\kappa}_{r,m-1} = \bar{\kappa}_{r,N}$

15: ***while*** (m ⩽ N)
16: $\Phi_{left} \leftarrow \dfrac{FT\big[u(\bar{\kappa}_{r,m-1},\, \bar{\kappa}_{i,j})\big]}{FT\big(u_{left}\big)}$
17: ***if*** $\big(\|\nabla f_1(\bar{\kappa}_{r,m}, \bar{\kappa}_{i,j})\|_\infty\big) \leqslant tol$
18: ***break***
19: ***end if***
20: ***end while***

21: ***end if***
22: ***end while***

23: ***end if***

24: ***if*** $\big(\|\nabla f_1(\bar{\kappa}_{r,n}, \bar{\kappa}_{i,n})\|_\infty$ & $\|\nabla f_2(\bar{\kappa}_{r,n}, \bar{\kappa}_{i,n})\|_\infty\big) \leqslant tol$
25: ***break***
26: ***end if***
27: ***end while***
28: ***end for***

Figure 2.6: Pseudo-code for the dispersion curves identification of a nonlinear damped periodic system.

The first guess ($\bar{\kappa}_{r,0}$, $\bar{\kappa}_{i,0}$) is arbitrary. For the selected $\bar{\omega}$, the RS is interrogated at each n iteration with inputs $\bar{\kappa}_{r,n}, \bar{\kappa}_{i,n}$. If the least-squares problem (2.13) is not solved after $n = N$ iterations, that is, if row 24 is not satisfied for ($\bar{\kappa}_{r,N}, \bar{\kappa}_{i,N}$), the last solution $\bar{\kappa}_{r,N}$ is imposed, as known

in a further least-squares problem (see row 10), where only the first of the equations in (2.13) is employed in the only unknown $\bar{\kappa}_{i,j}$. Then, the while loop in row 15, with the last solution $\bar{\kappa}_{i,j}$ and an initial condition $\bar{\kappa}_{r,N}$ for the unknown $\bar{\kappa}_{r,m}$, completes the identification process.

2.4.1 Application

The aforementioned procedure was performed for the system examined in Subsection 2.3.1, where a nonlinear stiffness $k_{NL} = 200\,\text{MN/m}^3$ was added. Damping will be introduced later.

The RS is shown in Fig. 2.5. For the undamped case, with $c = 0$ and $c_R = 0$, we compared the numerical results with the approximate nonlinear dispersion relation proposed by Zivieri et al. [14]:

$$\begin{aligned} & mm_R\omega^4 \\ -\big[k_R(m+m_R) + 2m_Rk\big(1-cos(\kappa d)\big) + 2m_RU^2k_{NL}\,G(\kappa d)\big]\omega^2 \\ & +2k_R\big[k\big(1-cos(\kappa d)\big) + k_{NL}U^2G(\kappa d)\big] = 0, \end{aligned} \tag{2.14}$$

where $G(\kappa d) = \frac{1}{3!}[1-cos(3\kappa d)+3cos(2\kappa d)-3cos(\kappa d)]$ is a wavenumber-dependent series, U defines the amplitude, and the distance d between the masses is equal to 1. A comparison between the identified and approximate solutions is shown in Fig. 2.7, for an amplitude $U_{left} = 10$ mm, which can be interpreted to a certain extent as a medium-high amplitude [14].

Fig. 2.7 shows that the identification process has not been impaired by the initial guesses; however, some outliers appear in the first pass-band due to failures in the integration of (2.13) around the first natural frequency of the unit cell of the RS. The solutions agree well with the approximate relation (2.14) derived by Zivieri et al. [14]. We recognize that the dependence of the dispersion curves on the amplitude is not evident in Fig. 2.7, and the nonlinear solutions seem to be pairing the linear ones. To better highlight the dependency of the dispersive properties on the input amplitude, we computed and reported in Fig. 2.8 the identified nonlinear solutions $\bar{\kappa}$, nondimensionalized over the linear solution κ_l, for several amplitudes $U_{left} = [1.1, 1.2, 1.3, 1.4, 1.5]$ mm in the frequency range $\bar{\omega} = [28-29]$ rad/s . Here, the input amplitudes are intentionally small for a better comparison with the linear solutions.

To further corroborate the results of our approach, we compared the numerical values of the transmission function Φ_{left} with an analytical

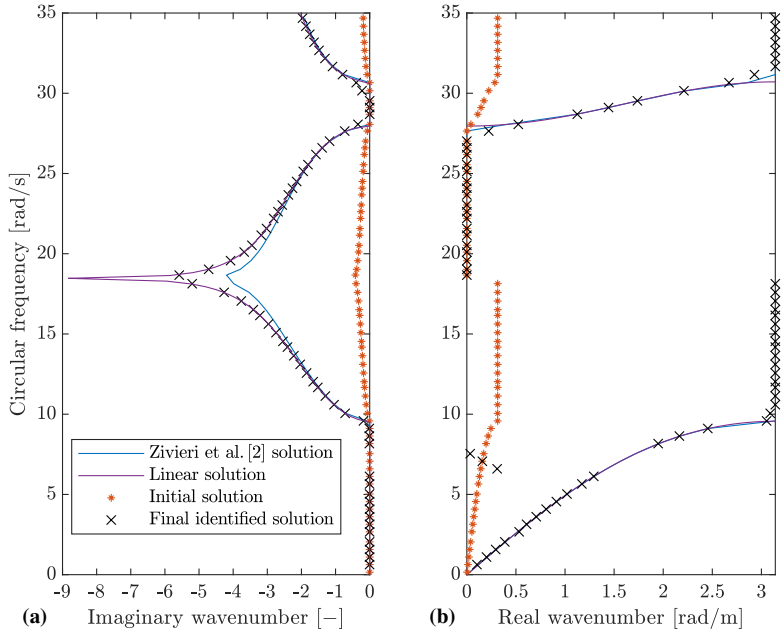

Figure 2.7: Identification of the undamped periodic system: (a) plot of the imaginary components κ_i and (b) plot of the real components κ_r of wavenumbers. The identified solutions are compared to the approximate solution of (2.14) *whilst the red stars indicate the initial guess.*

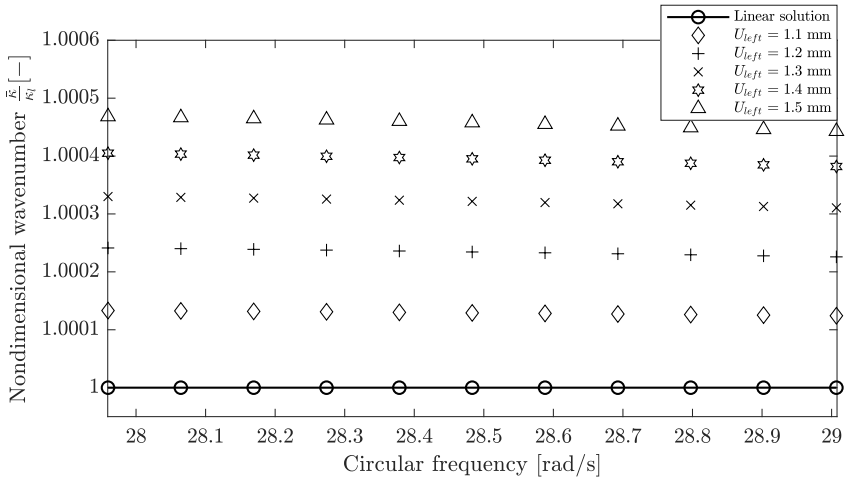

Figure 2.8: Ratio between the identified nonlinear solutions $\bar{\kappa}$ and the linear solutions κ_l, for several amplitudes of excitation.

expression for the FRF. For this purpose, we consider a harmonic solution for the displacements u and u_R in (2.12), and before linearization, we apply the FB theorem. We obtain the expression for nonlinear transmission as follows:

$$\frac{U}{U_{left}} = \frac{k\,(1+e^{2i\kappa d})}{-m\omega^2+2k+k_R-\frac{k_R^2}{k_R-\omega^2 m_R}} - \frac{K(e^{ji\kappa d})\,k_{NL}\,e^{2i\omega t}}{U_{left}\left(-m\omega^2+2k+k_R-\frac{k_R^2}{k_R-\omega^2 m_R}\right)}, \tag{2.15}$$

where i is the imaginary unit, and the function $K(e^{ji\kappa d})$ comprises higher orders j of the wavenumber, as follows:

$$\begin{aligned} K(e^{ji\kappa d}) = &- U_{left}^3 + 3UU_{left}^2 e^{i\kappa d} - 3U^2 U_{left} e^{2i\kappa d} + 2U^3 e^{3i\kappa d} \\ &- 3U^2 U_{left} e^{4i\kappa d} + 3UU_{left}^2 e^{5i\kappa d} - U_{left}^3 e^{6i\kappa d}. \end{aligned} \tag{2.16}$$

The relationship (2.15) indicates that for a given frequency, the output of the RS depends on the wavenumbers $j\kappa$, with $j \geq 2$, which are naturally associated with superharmonics. Similarly, the dependence on input amplitude U_{left} is evident. Because the identification procedure proposed in this work relies on (2.4), this implies that a single complex wavenumber is associated with a given frequency; hence, (2.4) ignores the components associated with higher-order wavenumbers $j\kappa$.

For this reason, we utilize a perturbation approach, based on the Lindstedt–Poincaré technique, to understand the effects of the aforementioned approximation. Based on the asymptotic expansion reported in Appendix A.1, we obtain

$$FRF_p = FRF^{(0)} + \epsilon\, FRF^{(1)} + O\,(\epsilon^2), \tag{2.17}$$

where $FRF^{(0)}$ and $FRF^{(1)}$ read

$$FRF^{(0)} = \frac{k\,(1+e^{2i\kappa d})}{-m\omega_{(0)}^2+2k+k_R-\frac{k_R^2}{k_R-m_R\omega_{(0)}^2}},$$

$$FRF^{(1)} = \left(\frac{8\,m_R\,\omega_{(0)}\,\omega_{(1)}\left({k_R}^2\,m_R+m\,{k_R}^2-2\,m\,k_R\,m_R\,\omega_{(0)}^2+m\,{m_R}^2\,\omega_{(0)}^4\right)}{3\,k_{NL}\,m\left(k_R-m_R\,\omega_{(0)}^2\right)^2(1-e^{2i\kappa d})^2\left|U_{left}\right|^2}\right)^{\frac{1}{2}}. \tag{2.18}$$

The order ϵ^0 equation defines the FRF of the linear system and equates the first term on the right-hand side of (2.15). The expansion of Eq. (2.17) is instead arrested at order-ϵ^1, and the relevant order-ϵ^1 equation is an

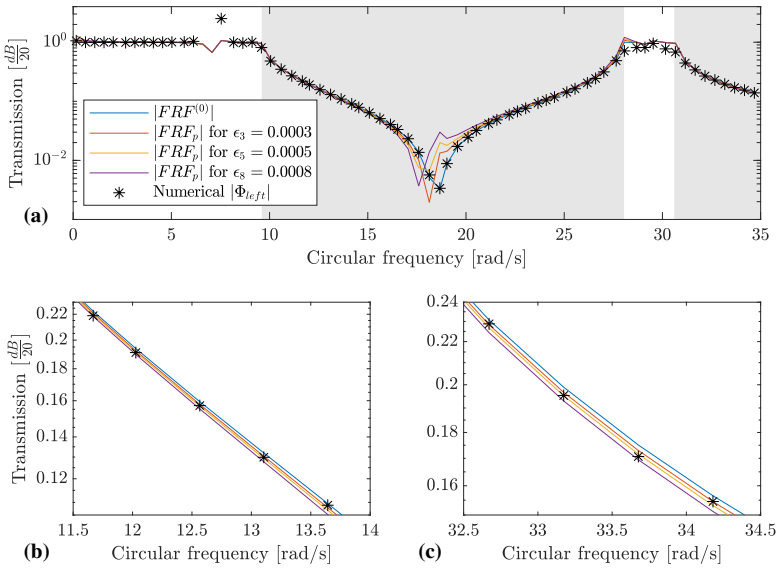

Figure 2.9: Comparison between the numerical transmission and the analytical $|FRF_p|$ of Eq. (2.17): in (a) the gray areas highlight the bandgaps, (b) zoom in the range of frequencies in the first bandgap and (c) in the second bandgap.

expression that does not depend on the linear stiffness k. It also contains high wavenumbers associated with the frequency $\omega = \omega_{(0)} + \epsilon\,\omega_{(1)}$, which was stopped at the first ϵ^1 order. A comparison between the aforementioned FRF and the transmission obtained as the outcome of the identification process based on (2.4) is shown herein and indicates that the involved approximation is favorable. The numerical values of Φ_{left} that satisfy the tolerance of the identification procedure described in the pseudocode in Fig. 2.6 are plotted in Fig. 2.9; they correspond to the set of solutions already presented in Fig. 2.7, for $U_{left} = 10$ mm.

Fig. 2.9 (a) clearly shows that the numerical values of Φ_{left} and the approximate solutions of (2.18) are close. Precisely, we have estimated

$$\begin{aligned} err^{\epsilon_3} &= 4.75\%, \\ err^{\epsilon_5} &= 5.05\%, \\ err^{\epsilon_8} &= 5.43\%, \end{aligned} \tag{2.19}$$

where err is the mean error wrt the numerical Φ_{left} for all frequencies. As expected, outside the bandgap the absolute value of the transmission is equal to 1.

We now consider the case of a damped chain with $c = 929.83$ N·s/m and $c_R = 7.83{\cdot}10^3$ Ns/m. To measure the degree of approximation of the proposed identification procedure, we derive an approximate expression

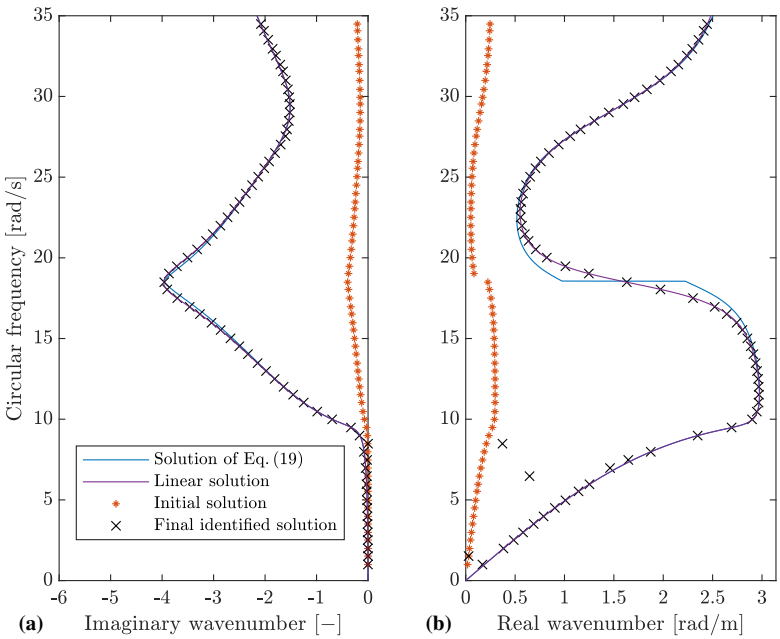

Figure 2.10: Numerical identification of the damped periodic system for (a) the imaginary components κ_i and (b) the real components κ_r of wavenumbers. The numerical results are compared to the analytical solution provided by (2.20)*; the red stars indicate the initial guess.*

for the dispersion law of a damped nonlinear chain, employing the same assumptions as Zivieri et al. [14]:

$$\begin{aligned} m m_R\,\omega^4 + \left[-c_R\,(m+m_R)\,i + 2\,c\,m_R\,\sigma\,i\right]\omega^3 \\ +\left[2\,k\,m_R\,\sigma - 2\,G(\kappa d)\,k_{NL}\,m_R\,U^2 - k_R\,(m+m_R) + 2\,c\,c_R\,\sigma\right]\omega^2 \\ +\left(2\,i\,G(\kappa d)\,c_R\,k_{NL}\,U^2 - 2\,c\,k_R\,\sigma\,i - 2\,c_R\,k\,\sigma\,i\right)\omega \\ -2\,k_R\left(k\,\sigma - G(\kappa d)\,U^2\,k_{NL}\right) = 0, \end{aligned} \tag{2.20}$$

where $\sigma = cos(\kappa d) - 1$. The relevant results obtained using the identification procedure are shown in Fig. 2.10 for $U_{left} = 10\,\text{mm}$ and suitable initial conditions.

Two branches of the undamped curve in Fig. 2.7 (b) here merge into a single curve, Fig. 2.10 (b), that features the characteristic S-shape of damped resonant metamaterials. This additional branch is characterized by a backward slope determined by a negative group velocity [66]. From Fig. 2.10 (b) it is evident that the analytical prediction (2.20) for the real components of wavenumbers agrees with the identified curve, but tends to lose accuracy in that range of negative group velocity; however, in

Fig. 2.10 (a), the imaginary components adequately predict the spatial attenuation $exp\,(-\kappa_i d)$ of the free wave.

2.5 Conclusions and future outlooks

In this study, we proposed a novel procedure for identifying dispersion laws for both linear and nonlinear 1D periodic mass-in-mass discrete systems. For this purpose, we employed the output of a reference subsystem (RS), which includes the system unit cell and is subjected to controlled displacements that meet the Floquet–Bloch (FB) periodic conditions. In particular, with few tools, that is, the FB periodic conditions, the frequency response functions (FRFs) of the RS, and the Levenberg–Marquardt algorithm, we were able to identify the eigenvalues of linear and nonlinear undamped and damped periodic systems.

The advantages of the proposed procedures are fourfold: i) the procedures do not operate on finite lattices and, therefore, numerical/experimental issues related to wave reflections, perfectly matched layers, and so on are avoided; ii) the identification effort is reduced because the procedure relies on a simple experimentally informed RS; iii) the identification of the dispersion law also includes the imaginary part of wavenumbers; iv) the identification procedure captures the dependency of the nonlinear dispersion curves on the amplitude of excitation. Accordingly, we envision the application of this method to the experimental outputs of the physical RS of a 1D linear and nonlinear periodic discrete system excited under displacement control. Along this line, the physical realization of an RS with the control of parameters that accurately govern nonlinear terms remains challenging and may become critical for experimental systems that need to account for dissipation, hysteresis, and disorder. Finally, we anticipate that the proposed dispersion law identification procedure can be completed with parametric identification of the unknown nonlinear mechanical characteristics by exploiting the identified eigenvalues of the dispersion curve.

3.0 A novel postbuckling-based device for switching the propagation of SAWs

This chapter contains the pre-print of:

Fabrizio Aloschi, Antonio Palermo, and Chiara Daraio. Postbuckling-based mechanical switching of surface acoustic waves; in preparation for *Applied Physics Letters*,

as it will be submitted for the Journal *Applied Physics Letters*, differing only in terms of layout and formatting.

The use of periodic materials to control the flow of energy has been a focus of intense study. Switchers, rectifiers, and transistors often rely on magnetic fields and/or logic gates to activate their mechanisms. We propose a novel device that enables the control of mechanical waves - surface acoustic waves - through an ON-OFF mechanism. The device utilizes outer beams as a tunable platform to switch the propagation of the waves. The OFF configuration is achieved by having the beams in their undeformed configuration resonate at specific frequency ranges, resulting in the creation of bandgaps. Conversely, in the ON configuration, the beams in postbuckling undergo softening, which cancels the bandgaps and allows for the flow of energy. Analytical and numerical results demonstrate the potential of this device for controlling the wave propagation with nonlinear periodic materials. The switching mechanism is achieved through the activation of the nonlinearity, eliminating the need for external magnetic fields or logic gates.

3.1 Introduction

The control of energy flow through periodic materials has been successful in various fields [79, 80], including the control of surface acoustic waves (SAWs) [27, 20, 21, 22]. Material and geometric nonlinearities have been utilized to exploit phenomena such as localization [30],

breathers [31], bifurcation, and chaos [29]. Postbuckling is a promising alternative among other geometric nonlinearities due to its ease of realization and reversible nature. Shifting between prebuckling and postbuckling without inducing plastic deformation allows for greater control and versatility.

In this context, our approach proposes a novel strategy for manipulating SAWs using elastic slender beams functioning as resonators. Our device features an array of resonator beams placed along the edge of a thin plate serving as a 2D model. FE simulations and analytical tools justify the compact setup that can be designed to experimentally switch the edge waves. Two conceptual diagrams in Fig. 3.1 illustrate the proposed switching mechanism.

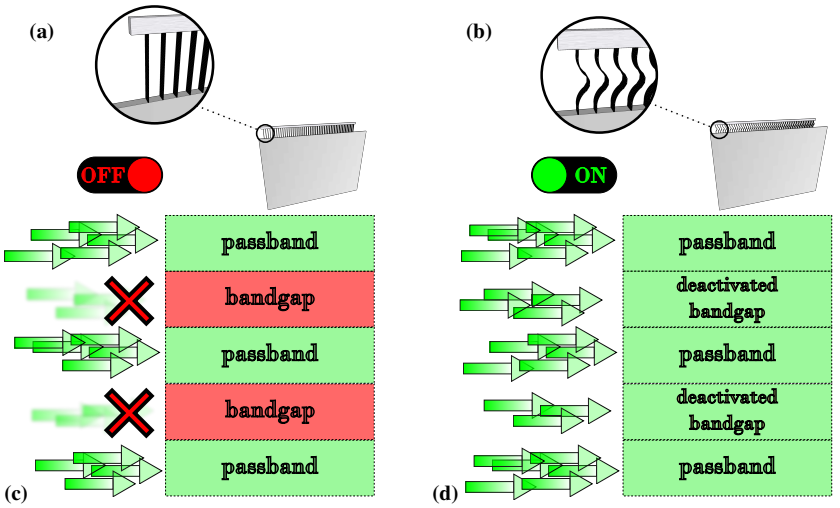

Figure 3.1: 3D view of the device endowed with beams in (a) prebuckling, (b) postbuckling. Conceptual diagrams of the switching mechanism for (c) OFF configuration, (d) ON configuration.

The design of the beams aims to have their axial modes within the frequency range of the SAWs. In a prebuckling configuration, when no compression is applied, the beam's resonances generate bandgaps in the SAWs' dispersion, which is the OFF configuration. The application of external compression beyond the critical load leads to buckling and softening in the beams [81], causing a reduction in the amplitude vibration response and lowering of the first normal modes. The buckled configuration, which is the geometric nonlinearity, activates the ON configuration of the switching mechanism, cancelling the bandgaps and allowing the transmission of SAWs in those frequency ranges.

Although buckling has been a well-known phenomenon for centuries,

it is typically simplified through special design modifications, yet it attracts growing interest in the design of mechanical systems for *smart* purposes [82]. The theory is replete with investigations about the stability of buckled beams, with exact solutions for stability existing [83, 84], and numerous nonlinear methods for model order reduction have been developed [85]. However, the axial and transverse components of the vibration in buckled beams are always decoupled, and, to the best of our knowledge, all the existing investigations concern only the transverse vibration [86]. Therefore, although the problem of determining the exact axial modes remains unchallenged, discrete spring-mass models based on experimental or numerical functions have been adopted to describe the axial dynamics of buckled beams and justify the existence of solitons [87, 88]. However, these models feature a quasi-static approximation of the spring model that cannot be accepted in our case since it neglects inertial effects. Thus, we employ a harmonic perturbation around the postbuckling equilibrium of a 2D FEM of the single beam to show that our external platform can cancel the bandgaps, or in other words, shift the axial resonances of the buckled beams out of the range of interest of the SAWs' dispersion.

3.2 A device for the propagation of the SAWs

To showcase the switching mechanism we resort to numerical simulations and present a novel device designed to manipulate surface acoustic waves (SAWs), which is currently being manufactured in our lab for experimental testing. The key element of the device is a thin PMMA plate that serves as the substrate for the propagation of SAWs. Utilizing thin plates is a well-established practice in seismology [89], as two-dimensional models offer ease of fabrication. This suitability of thin plates is based on the similarity between Rayleigh waves and extensional waves that propagate along the edge of a semi-infinite plate, sharing an analogous dispersive relationship [90, 91]. Therefore, as in [27], we propose the compact device shown in Fig. 3.2 for our study.

A PMMA plate with dimensions of $H = 563$ mm, $L = 900$ mm, and a thickness of $t = 8.5$ mm, is rigidly connected to an optical table at the bottom edge, while the top edge is coupled to a periodic arrangement of 41 polyester beams (PVC: $E_b = 2e9$ Pa, $\rho_b = 1270$ kg/m^3) with dimensions of $l_b = 66$ mm, $h_b = 0.8$ mm, and a thickness of $t = 8.5$ mm. The beams are slender, with $l_b > 50 \cdot h_b$, and they act as mechanical resonators. To couple the beams to the plate, 41 laser cuts are made at the top edge of the plate, and the beams are inserted into the cuts. This

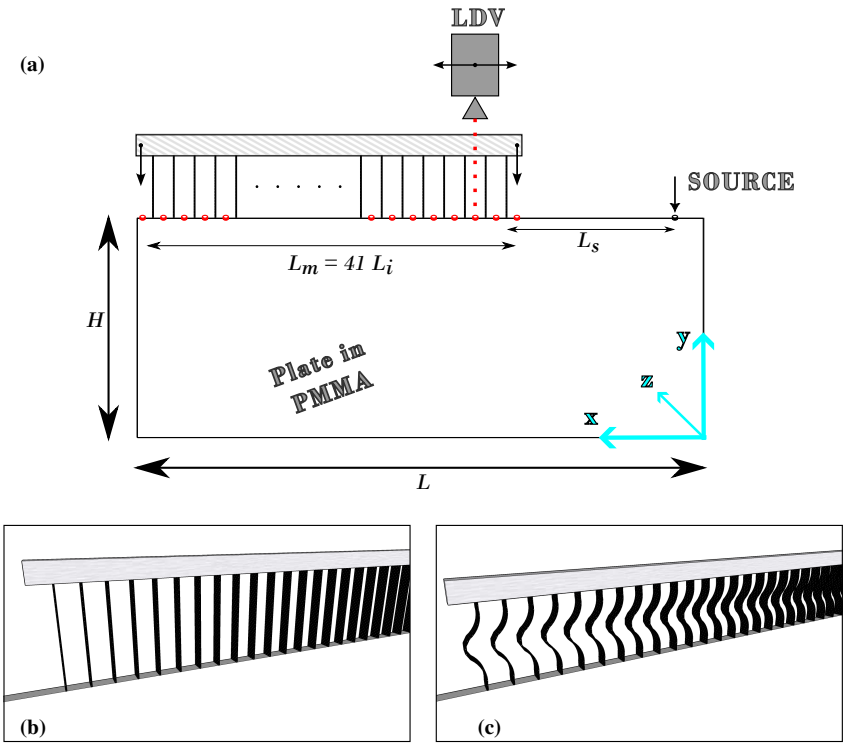

Figure 3.2: (a) Schematic of the device. Detail of the external platform: (b) beams in prebuckling, (c) in postbuckling.

creates a friction-based coupling. Similarly, the tips of the beams are inserted into a smaller top plate, shown as a gray top slab in Fig. 3.2 (a). The slab has a dual function: it constrains the tips of the beams and applies uniform compression when using the postbuckling configuration, i.e., the ON configuration.

Surface waves can be generated using any mechanical transducer placed at a distance $L_s = 177$ mm from the first beam. The interdistance between the beams is $L_i = 15$ mm. The waves are vertically polarized and propagate as edge waves that can be shaped by a simple signal generator. In our simulation, we use a wide-band Ricker wavelet with a central frequency of $f_p = 10$ kHz; the shortest wavelength that we observe is equal to 15 mm, which is significantly larger than the beam dimension h_b. To reconstruct the dispersion curve of the edge waves, we need to measure the vertical component of the velocity along the top surface of the plate at multiple observation points (shown as small red cylinders in Fig. 3.2). To accomplish this, at least one laser Doppler vibrometer (LDV) is required. Therefore, to obtain measurements at mul-

tiple points, the LDV can be mounted on a horizontally motor-powered linear stage and then connected to an oscilloscope to acquire the output.

3.3 Dynamics of the external platform

The switching mechanism relies on an external platform composed of a periodic array of 41 mechanical resonators, namely the 41 slender beams depicted in Fig. 3.2 (b) and (c). To investigate the dynamics of the external platform, we begin by examining the vibration properties of a single resonator-beam, with periodicity being introduced in the following section.

Fig. 3.3 reports the buckling analysis of a doubly-clamped beam.

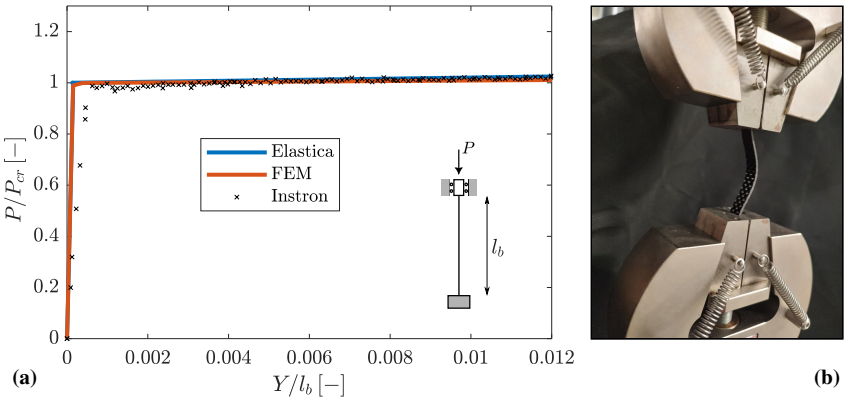

Figure 3.3: Static behavior of an axially-loaded clamped beam: (a) load - displacement diagrams; (b) picture of a beam under Instron test.

Fig. 3.3 (a) shows the axial load - displacement graph of a doubly-clamped beam, where the displacement is measured at a distance $s = l_b/4$ from the bottom clamp. The elastica [92] provides an analytical expression for the shape of the entire beam for the curvilinear coordinate s in the range $[0, l_b]$, given by:

$$Y(s) = -s + \frac{2}{p}\{E\left[\text{am}(sp, \chi), \chi\right]\}, \tag{3.1}$$

$$X(s) = \frac{2\chi}{p}[1 - \text{cn}(sp)], \tag{3.2}$$

where Y and X represent the longitudinal and transverse displacement, respectively. $E(-, \chi)$ stands for the incomplete elliptic integral of the second kind with modulus χ, while 'am' and 'cn' are the Jacobi amplitude function and Jacobi cosine amplitude function, respectively. The

applied load P is contained in $p = \frac{P}{E_b I}$. The value of χ is given by $\chi = \sin(\frac{\bar{\theta}}{2})$, where $\bar{\theta}$ is the rotation angle where the bending moment becomes zero. The relation between the applied load P and the rotation $\bar{\theta}$ associated with the odd (symmetric) m$^{\text{th}}$ buckling mode is given by:

$$P = \frac{E_b I}{l_b^2} 4(m+1)^2 [K(\chi)]^2 \tag{3.3}$$

where $K(\chi)$ is the complete elliptic integral of the first kind.

Fig. 3.3 (a) shows the results of a buckling static test carried out using an Instron (ElectroPuls E3000) on a polyester (PVC) beam. A good agreement is observed between the curves in Fig. 3.3 (a); however, some discrepancies are seen in the prebuckling regime due to small imperfections [88]. The crosses indicate the average of eight tests conducted at a rate of 3 min/mm. To avoid plastic deformations, the tests were stopped at $\frac{Y}{l_b} = 0.15$. However, in Fig. 3.3 (a), we focus on the region around the Euler critical load P_{cr}, and the plot is limited to $\frac{Y}{l_b} = 0.012$. We investigate the dynamics of the beam around its postbuckling configuration $\frac{P}{P_{cr}} = 1.01, , \frac{Y}{l_b} = 0.0117$.

Firstly, let us introduce the longitudinal vibration problem for the linear regime that can be solved by looking at the theory of the longitudinal waves in thin bars [93]. A clamped-clamped beam or bar with zero displacements imposed at the boundaries has n integer multiple half-wavelengths between the ends of the beam, resulting in a harmonic series of normal mode frequencies f_n:

$$f_n = n \frac{c_B}{2 l_b}, \tag{3.4}$$

where c_B is the phase speed that is easily retrieved from the wave equation, and reads:

$$c_B = f\lambda = \frac{\omega}{\kappa} = \sqrt{E_b/\rho_b}, \tag{3.5}$$

where f is the frequency, λ is the wavelength, ω and κ are the circular frequency and the wavenumber, respectively. This speed of longitudinal wave propagation depends upon the ratio of the beam's Young modulus E to its mass density ρ: neither the area nor the cross-section influences c_B. For thin beams, this assumption is valid for those frequencies that are sufficiently low, such that the wavelengths are significantly greater than the cross-sectional dimensions. We will prove this assumption to be valid for the beams of our platform, and will show that when the beams are in the prebuckling regime, i.e., in the OFF configuration, the normal modes of (3.4) cause local resonances that interact with the SAWs dispersion.

The analytical problem of vibrations in buckled beams often only considers the transverse component of displacement, while the axial component is typically neglected [83, 84, 85, 86]. Intuitively, buckling softens the beam, as shown in Fig. 3.3 (a), and one would expect the first normal modes to shift to lower frequency regimes. To demonstrate this, we perform a frequency analysis of a simple 2D FEM in COMSOL Multiphysics. Specifically, a doubly clamped beam is buckled and compressed up to $\frac{P}{P_{cr}} = 1.01, , \frac{Y}{l_b} = 0.0117$, after which we apply a harmonic perturbation of amplitude displacement A_0 around the buckled configuration. The output amplitude displacement A is measured a few millimetres above the fixed base of the beam, and the resulting FRF is shown in Fig. 3.4.

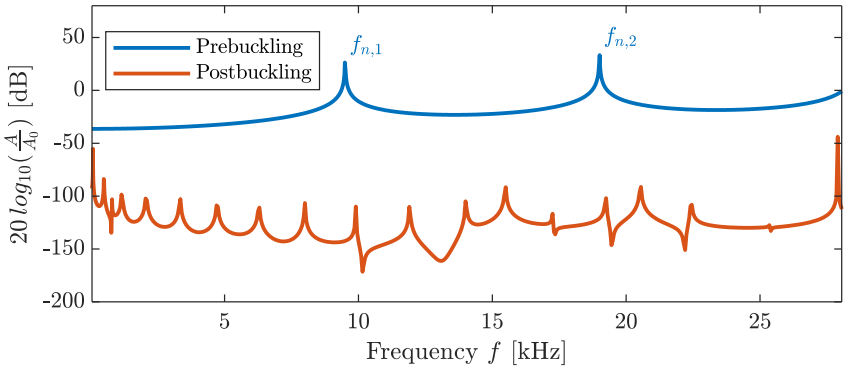

Figure 3.4: Longitudinal frequency analysis of a 2D FEM of the clamped-clamped polyester beam.

The red curve in Fig.,3.4 reveals that in the postbuckling regime, the amplitude of vibration A never attains the input amplitude A_0, i.e., it always remains $FRF < 0$. Furthermore, the first normal modes have shifted below 500 Hz. In contrast, the FRF of the prebuckling regime confirms the normal modes of (3.4), thus validating the thin bar assumption.

3.4 Numerical simulation of the device and a WFE model of the periodic system

Effective medium approaches can provide analytical dispersion relations of uniformly distributed oscillators [94]. However, these models fail to describe the discrete lattice effects that occur at short wavelengths where the wave dispersion induced by local resonances is not negligible. Therefore, to verify the switching mechanism of our device, we employ finite

element simulations. Firstly, we simulate the complete experimental machinery of our device in COMSOL Multiphysics to reconstruct the experimental dispersion curve of the SAWs. Next, we use a wave-finite-element model (WFEM) of the system's unit cell to disclose the dispersive properties of an infinite arrangement of beam-resonators resting on the elastic substrate. Both results are presented in Fig. 3.5.

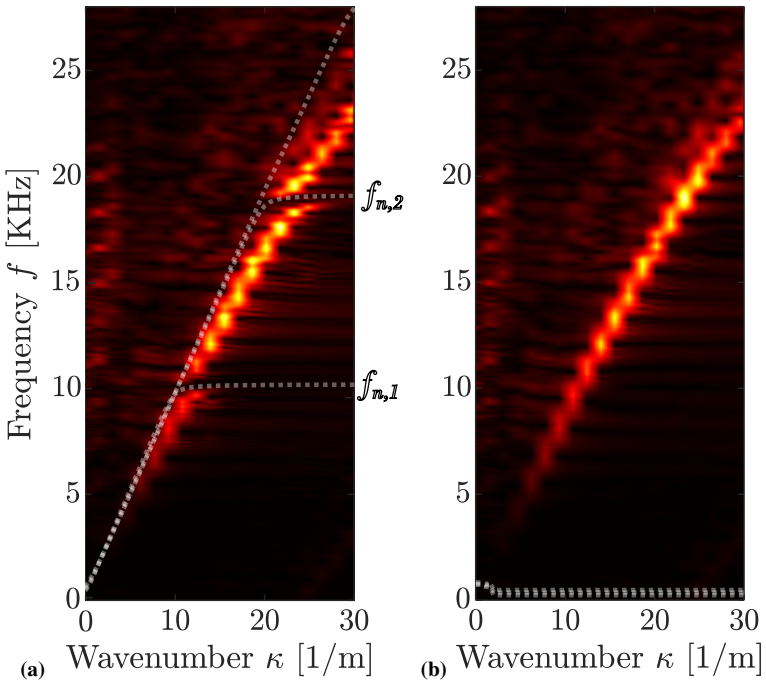

Figure 3.5: SAWs dispersion curves: (a) OFF configuration, beams in prebuckling; (b) ON configuration, beams in postbuckling. The background of the figures is the 2D Fourier Transform (FT) of the transient analyses simulated via COMSOL; the dotted red curves are deducted by the WFE model of the system's unit cell depicted in Fig. 3.6.

The beams in the undeformed configuration resonate according to (3.4), where the first two axial modes $f_{n,1}$ and $f_{n,2}$ generate the bandgaps observed in Fig. 3.5 (a) and determine the OFF state of the device. To achieve the ON state, the beams are axially compressed up to $P = 1.01P_{cr}$, resulting in a noticeable reduction of the response vibration amplitude, as already shown in Fig. 3.4, and in a sensible decrease in frequency of the first normal modes, as seen in Fig. 3.5 (b). In the frequency range of interest, 5 kHz to 23 kHz, the SAWs propagate undisturbed again.

The simulation is validated by the dotted red dispersion curves in

Fig. 3.5, which are calculated using a WFEM of a single unit cell under plane-stress conditions. A schematic of the unit cell is shown in Fig. 3.6. The unit cell consists of a vertical beam and a strip of the plate represent-

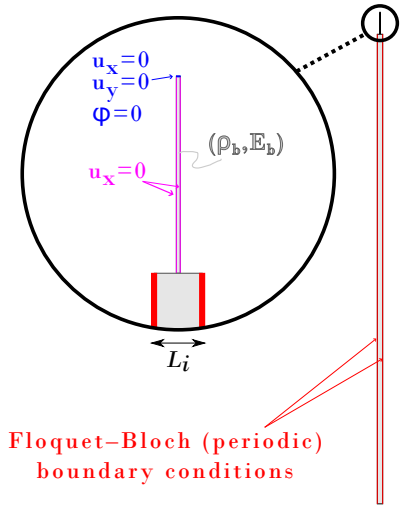

Figure 3.6: Schematic representation of the WFEM employed for the system's unit cell.

ing the elastic substrate. To obtain the dispersion curves, Floquet–Bloch boundary conditions are imposed on the vertical edges of the substrate with a wavenumber ranging between 0 and $1/(2L_i) = 33.3$ 1/m, and the eigenfrequencies are solved for each wavenumber. To account for buckling effects, a tangent material modulus $E_b = 2.4e5$ Pa is used, corresponding to the postbuckling configuration with $\frac{P}{P_{cr}} = 1.01$ and $\frac{Y}{l_b} = 0.0117$. This allows for the eigenvalue problem of the WFEM to be solved for a linear system. The width of the strip is equal to the inter-distance L_i of the beams, while its length is $4H$ to emphasize Rayleigh wave effects and avoid non-zero frequency values with respect to zero wavenumber. To restrict the analysis to vertically polarized waves, the interfaces of the beam are imposed to move vertically only ($u_x = 0$), while the top of the beam and the bottom of the substrate are fixed ($u_x = 0$, $u_y = 0$, $\phi = 0$).

To further prove the proposed switching mechanism, we test its effectiveness against a system that presents bandgap widening. This widening effect is achieved through rainbow trapping [65, 95, 96] that requires arrays of resonators with different characteristics. Therefore, we arrange 41 resonator beams with different Young modulus, such that each beam distills a different frequency within the frequency range $\Delta f_n =$

$[13.5, 15.5]$ KHz. From Eq. (3.4) it follows:

$$\Delta E_b = \rho_b \frac{2 l_b \Delta f_n}{n} = [4.03, 5.32] \cdot 10^9 \text{ Pa} \tag{3.6}$$

where $n = 1$, $\rho_b = 1270$ kg/m^3 and $l_b = 66$ mm. Each beam is statically tested, and the axial load - deformation diagram of the two beams with the lowest and the highest Young modulus are plotted in Fig. 3.7 (a). The curves of Fig. 3.7 (a) are calculated with the elastica (3.1). Despite the

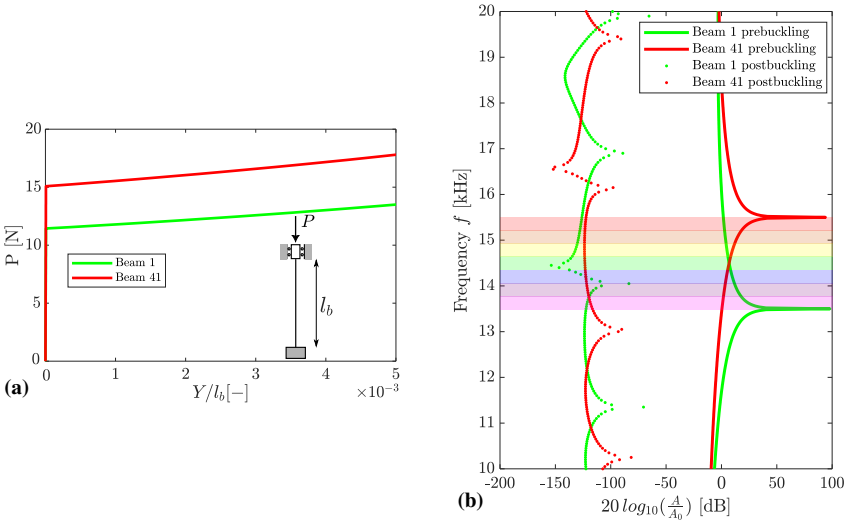

Figure 3.7: (a) Axially-loaded clamped beams in rainbow configuration: load-displacement graph calculated via Eq. (3.1)*; (b) FRF of the first and the last beam of the random rainbow arrangement.*

first and the last beam of the periodical arrangement have respectively the lowest and the highest Young modulus (Beam 1 and Beam 41), all the other beams are randomly arranged along the surface and not spatially graded, to achieve a wider attenuation range [96]. The frequency analysis of Beam 1 and Beam 41 are reported in Fig. 3.7 (b) and reveals a 2 KHz-wide resonant zone of the new platform with the rainbow configuration. Obviously, this resonant zone is relevant to the beams in the prebuckling regime, whereas in the postbuckling regime the amplitude of the FRF is drastically reduced.

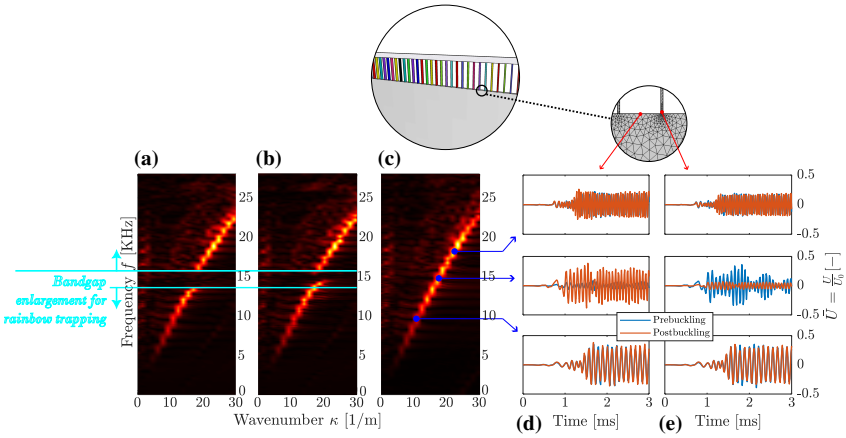

Figure 3.8: Dispersion curves of the SAWs: (a) random rainbow OFF configuration, (b) uniform material beams OFF configuration, (c) random rainbow ON configuration. A bandgap widening is shown wrt the case of uniform material beams. Harmonic analysis of the device in rainbow configuration: (d) the output is placed along the edge of the plate, (e) the output is placed a few millimetres above the base of a single beam.

Fig. 3.8 reveals the potential of the postbuckling-based mechanical switching for the device equipped with beams in a random rainbow arrangement. The dispersion curves confirm the effectiveness of the switching mechanism: when the beams are in the prebuckling regime, Fig. 3.8 (a), the switching is inactive and a wide bandgap filters the SAWs in the frequency range Δf_n of (3.6). In the postbuckling regime, Fig. 3.8 (c), the switching is activated and the SAWs are allowed to transmit. Time harmonic analyses are performed for frequencies that are below, inside, and above the bandgap. The output $\bar{U}$ is the vertical displacement response $u(t)$ normalised over the input amplitude $U_0 = 10$ μm. One can note that, while the transmission of the waves below and above the bandgap is never disturbed, in the bandgap the beams configuration (prebuckling or postbuckling) significantly affect the steady state of the SAWs.

3.5 Conclusions and outlook

SAWs are often used to convert electrical signals into mechanical waves and vice versa, which has led to their extensive use in various applications, such as sensors, resonators in microelectromechanical systems (MEMS), filters, and so on. Researchers have developed various strategies for controlling SAWs, such as using acoustic metamaterials, nonlinear media, and micro/nanomechanical structures.

Along this vein, we have presented a strategy for filtering surface acoustic waves (SAWs) using a switching mechanism. Our approach involves the use of elastic slender beams as resonators, which, when buckled, undergo a softening behavior that cancels bandgaps and allows for the transmission of SAWs. This switching mechanism has the charm of being activated by the nonlinearity of the system and surprisingly offers ease of realization.

While our strategy offers a novel approach to further improve these applications, it opens up the possibility of developing sensing devices that can detect sudden changes in material properties by monitoring the variation of the SAWs' dispersion.

4.0 Seismic waves attenuation in industrial structures through hysteretic nonlinear lattices

This chapter contains the post-print of:

Francesco Basone, Oreste S Bursi, Fabrizio Aloschi, and Günter Fischbach. Vibration mitigation of an MDoF system subjected to stochastic loading by means of hysteretic nonlinear locally resonant metamaterials. *Scientific reports*, 11(1):1–15, 2021,

as published in the Journal *Scientific reports, Nature Research*, differing from the published paper only in terms of layout and formatting.

In this work, we intend to mitigate absolute accelerations and displacements in the low-frequency regime of multiple-degrees-of-freedom (MDoF) fuel storage tanks subjected to stochastic seismic excitations. Therefore, we propose to optimize a finite locally resonant metafoundation equipped with massive resonators and fully nonlinear hysteretic devices. The optimization process takes into account the stochastic nature of seismic records in the stationary frequency domain; the records are modeled with the power spectral density (PSD) S_0 and modified with a Kanai–Tajimi filter. Moreover, the massive superstructure of a fuel storage tank is also considered in the optimization procedure. To optimize the nonlinear behavior of dampers, we use a Bouc–Wen hysteretic model; the relevant nonlinear differential equations are reduced to a system of linear equations through the stochastic equivalent linearization technique. The optimized system is successively verified against natural seismic records by means of nonlinear transient time history analyses. Finally, we determine the dispersion relations for the relevant periodic metafoundation.

4.1 Introduction

Within linear metamaterials, a new category of applications of phononic — or periodic — structures as alternatives to classic seismic isolators for earthquake mitigation has received growing interest [97, 35, 33, 98]. The increasing popularity of these structures resides in the possibility of exploiting the advantages of locally resonant acoustic metamaterials (LRAMs) due to their ability to attenuate low-frequency waves by means of unit cells much smaller than the seismic wavelength of the desired frequency region. The most common isolation solutions use lead-rubber bearings or spherical bearing devices, which are quite effective for the horizontal components of earthquakes. Nonetheless, these solutions require two strong floors, exert a very high stiffness against the vertical component of an earthquake, and are quite ineffective for large structures subjected to rocking [99]. To reduce the seismic responses of superstructures, Casablanca et al. [33] and Cheng and Shi [98] studied periodic and finite locally resonant foundations. Although good response reduction results were obtained, neither of the proposed periodic systems were designed for gravity and/or seismic load combinations. Furthermore, the authors did not consider the feedback forces from the superstructures to the metafoundations. To overcome these drawbacks, we proposed a finite lattice LRAM, the so-called metafoundation, for the seismic protection of multiple-degrees-of-freedom (MDoF) systems, i.e., storage tanks [35, 36, 100]. The relevant coupled metafoundation-tank system is depicted in Fig. 4.1 (a).

The foundation consists of flexible steel columns and concrete slabs that define the primary load-bearing structure, while massive concrete masses are considered resonators. The construction site is Priolo Gargallo in Sicily, Italy. The site is characterized by a peak ground acceleration (PGA) of 0.56g for a return period T_R = 2475 years. Therefore, a linear elastic design according to the Italian code [101] was carried out; the resulting minimal column stiffnesses allow the metafoundation to remain undamaged following safe shutdown earthquakes (SSEs). As a result, the columns have a total height of 4 m with hollow cross-sectional dimensions of 300x300 mm and a thickness of 30 mm. A 3D sketch of the coupled metafoundation-tank system shows that the foundation structure is composed of a finite number of 9-unit cells. Square hollow-section steel columns support each concrete slab and provide the lateral stiffness of the metafoundation. Each unit cell includes a massive concrete cube linked to the foundation, see Fig. 4.1 (b) and Fig. 4.1 (c) by means of wire ropes, as depicted in Fig. 4.2.

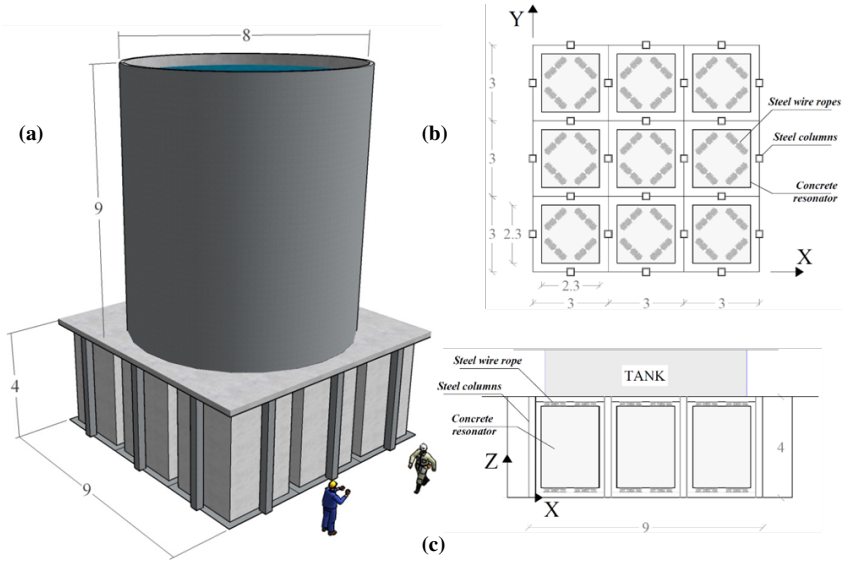

Figure 4.1: Coupled foundation - tank system: (a) 3D view, (b) layout of the unit cells and (c) cross section of the metafoundation. Dimensions are in m.

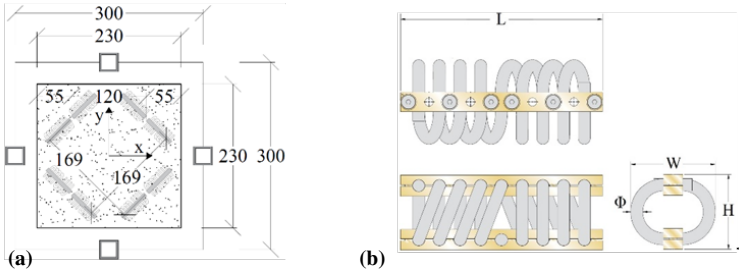

Figure 4.2: (a) Configuration of a single unit cell equipped with steel wire ropes; (b) details of a single wire rope. Dimensions are in cm.

Nonetheless, two basic issues remain unresolved: the optimization of structural devices, i.e., springs and/or dampers, operating in the nonlinear regime within finite lattices and the inclusion of the stochastic nature of the seismic input characterized by a large random uncertainty.

With regard to the first issue, i.e., the selection of proper hysteretic dampers, Basone et al. [36] suggested the use of wire ropes, which are simple devices able to both effectively suspend the concrete resonators inside the foundation and allow motion in all three main directions. Therefore, the behavior of wire ropes is quite complex, and the characterization of their nonlinear properties is difficult [102, 103]. More precisely, the mechanical flexibility of wire ropes provides good isolation prop-

erties, and the sliding friction between the intertwined cables results in high dissipative capabilities. As a result, these devices can achieve equivalent damping ratios of 15-20% with low production and maintenance costs. Their hysteretic behavior can be reproduced with the well-known Bouc–Wen model [102, 103, 104]. This model is quite popular because it can describe the behavior of a nonlinear hysteretic system with a compact first-order differential equation [105].

If we consider the aforementioned devices in periodic systems, the analysis of nonlinear metamaterials is still very challenging [106, 14]. For instance, from a perturbation approach specifically applied to weakly nonlinear periodic chains [107], the following topics emerge: i) the solutions to the nonlinear wave equations are amplitude dependent; ii) the wave amplitudes influence their own propagation characteristics, the so-called self-action; and iii) the analysis methods in the presence of self-action often do not trace all solutions when more than one dominant component is involved. Nonetheless, several researchers have devoted considerable effort to improving our understanding of nonlinear metamaterial-based systems. For instance, to reduce wave transmission in both ultralow and ultrabroad bands with band gaps and chaotic bands, Fang et al. [108] developed both a theoretical approach and an experimental validation to conceive nonlinear acoustic metamaterials (NAMs). Based on a new mechanism for wave mitigation and control consisting of the nonlinear interaction between propagating and evanescent waves, Zega et al. [109] recently presented experimental proof of the appearance of a subharmonic transmission attenuation zone due to an energy exchange induced by autoparametric resonance. In contrast, Gupta et al. [110] explored a wide range of nonlinear mechanical behaviors that can be generated from the same lattice material by changing the building block into a dome-shaped structure. In particular, they proposed a novel hourglass-shaped lattice metastructure that takes advantage of the combination of two oppositely oriented coaxial domes.

With regard to the second issue, i.e., the stochastic nature of the seismic input and the subsequent stochastic response analysis of hysteretic systems, an abundance of literature is available [105, 111, 112]. In this respect, the equivalent (stochastic) linearization technique (ELT) [105, 111], based on a non-Gaussian probability density function, is viable because it can be extended (in a relatively straightforward manner) to MDoF systems. Socha and Pawleta [113] discussed the advantages and disadvantages of this technique.

In summary, to achieve the best performance of a finite locally resonant metafoundation, the following objectives are pursued hereinafter: i) the optimization of the nonlinear behavior of wire ropes reproduced with

hysteretic Bouc–Wen models and ii) the application of the ELT to fully nonlinear devices taking into account the stochastic nature of the seismic input in both the frequency domain and the time domain.

The superstructure is composed of a slender fuel storage tank and its equivalent 2D lumped mass model [114], see Figs. 4.1 (a) and 4.3. More precisely, the slender tank was part of an existing plant, i.e., tank #23 or #24 of Case Study #1, analysed in a European research project [35, 100]. Housner's model [115] is adopted to simulate the hydrodynamic response of liquid containers. This model allows us to associate the inertial force of the liquid with two different masses: the impulsive mass and the convective mass. The tank response is reduced to the contributions of the two main impulsive and convective modes, and the tank wall thickness is taken into account. The tank's liquid content exhibits axial symmetry, which is sufficient to analyse the dynamics in one direction. However, each resonator can vibrate in all three (X, Y and Z) directions.

With regard to the metafoundation, it is designed to remain undamaged for an active seismic site located in Priolo Gargallo, Italy. Considering a consistent seismic input for linear/nonlinear time history analyses, a set of natural earthquakes that correspond to SSE events are selected from Italian and European databases and fitted on average to the uniform hazard spectrum (UHS) of Priolo Gargallo.

To take the stochastic nature of the seismic input into account, the computations are carried out in the frequency domain, and because the analysis of nonlinear periodic systems entails the aforementioned difficulties [107], the ELT is adopted for the Bouc–Wen model. Therefore, an average power spectral density (PSD) function of the accelerograms is evaluated. The resulting PSD function is filtered with a Kanai–Tajimi filter [116] modified by Clough and Penzien [117] and subsequently adopted in the optimization procedure. The resulting optimized metafoundation is then verified through nonlinear time history analyses (THAs) of the coupled system subjected to the aforementioned ground motions.

4.2 Methods

4.2.1 Nonlinear metafoundation system modelling

To address simpler coupled systems and to benefit from the optimization considering different stiffness and damping values, the condensed mass system (CMS) shown in Fig. 4.3 is considered. Through an exact dynamic condensation of both the masses and the stiffnesses along the X and Y directions we can analyse the CMS as a 2D system. This dynamic condensation does not lead to errors since all resonators in both the X

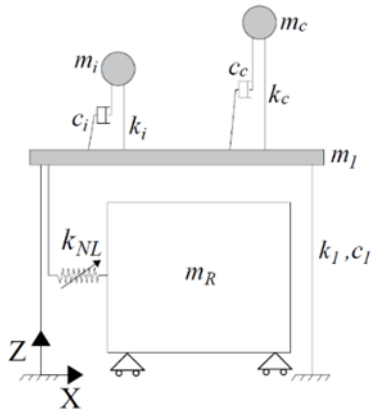

Figure 4.3: Metafoundation-tank coupled system model: condensed mass system (CMS).

and the Y directions are assumed to be endowed with the same mass and stiffness, see Fig. 4.1 (b). The CMS is depicted in Fig. 4.3, in which the dynamic characteristics of the system are reported as well. Herein, m_i, c_i and k_i represent the mass, stiffness and damping coefficients, respectively, of the impulsive mass of the superstructure-tank system, while m_c, c_c and k_c represent the mass, stiffness and damping coefficients of the relevant convective mass.

The following system of equations of motion (EOMs) describes the dynamics of the aforementioned metafoundation-tank coupled system:

$$\mathbf{M}\,\ddot{\mathbf{u}}(\mathrm{t}) + \mathbf{C}\,\dot{\mathbf{u}}(\mathrm{t}) + \mathbf{K}\,\mathbf{u}(\mathrm{t}) + u_y\,\mathbf{K}^{\mathrm{NL}}\mathbf{z}(\mathrm{t}) = \mathbf{F}(\mathrm{t}), \tag{4.1}$$

where **M**, **C** and **K** are the mass, damping and stiffness matrices, respectively; $\mathbf{K}^{\mathrm{NL}}$ defines the component of the stiffness matrix that contains the terms (1 - α_n) k_n introduced later; **z**(t) defines the vector that contains the components $z_n(t)$ of the n^{th} resonator modeled in the next subsection; and u_y sets the yielding displacement of the device. Therefore, Eq. 4.1 is a nonlinear system of EOMs due to the presence of u_y **K**NL **z**(t). The vector **u**(t) indicates the displacement vector, whilst single and double dots represent single and double derivatives with respect to (wrt) time, respectively. Furthermore, **F**(t) = -**M** τ üg(t) represents the forcing vector, where τ is the mass influence vector and $\ddot{u}_g(t)$ represents the ground acceleration.

To evaluate the dynamic properties of the CMS, the system equivalent reduction expansion procedure (SEREP) is adopted. This method allows the modal vectors of the CMS to be reduced [118]; therefore, the convective mode and the relevant DoFs of the tank can be eliminated

from the full set of 'n' DoFs, while the effects on the lower 'a' modes can be retained. More precisely, the SEREP technique is based on the following transformation:

$$\mathbf{u}_n = \mathbf{T}\ \mathbf{u}_a, \tag{4.2}$$

where $\mathbf{T} = \Phi_n\ \Phi_a{}^g$ is the transformation matrix, Φn is the modal matrix of the original system, and Φa^g is the generalized inverse of the modal matrix of the active/reduced system. More precisely, Φa^g can be evaluated as

$$\mathbf{\Phi}_a^g = \left(\mathbf{\Phi}_a^T \mathbf{\Phi}_a\right)^{-1} \mathbf{\Phi}_a^T, \tag{4.3}$$

As a result, the system matrices of the reduced system are $\widetilde{\mathbf{M}} = \mathbf{T^T M T}$, $\widetilde{\mathbf{K}} = \mathbf{T^T K T}$ and $\widetilde{\mathbf{C}} = \mathbf{T^T C T}$, while the forcing term becomes $\widetilde{\mathbf{F}} = -\mathbf{T^T M}\tau\ \ddot{u}g$. Since the optimization procedure requires an inversion of the transmission matrix $\mathbf{T}$ for each frequency interval, the SEREP technique also contributes to the reduction in the run time of the optimization algorithm.

4.2.2 Modelling of nonlinear devices

The nonlinear devices utilized in this work are steel wire ropes, schematically depicted in Fig. 4.2 (b). Steel wire ropes are a commonly used solution in seismic engineering due to their dissipative behavior. Moreover, they represent an inexpensive solution in terms of both production and maintenance costs. Thus, many researchers have investigated the hysteretic characteristics of wire ropes when subjected to shear forces [102, 103, 104]. In this context, steel wire ropes have already been successfully utilized in metafoundations. In some research works [36, 37], the goal was the protection of tanks against both horizontal and vertical ground accelerations by means of finite lattices equipped with nonlinear devices endowed with significant flexibility and hysteretic damping. Furthermore, steel wire ropes allow effective motion of the resonators along the X, Y and Z directions, which can be easily deduced by Fig. 4.1.

To model the nonlinear dissipative behavior of wire ropes, we employ the Bouc–Wen model. This model has been adopted to capture the hysteretic behaviors of many other seismic devices [102, 103, 119].

For the sake of clarity, let us consider a single-degree-of-freedom (SDoF) system:

$$m\ddot{u}(t) + c\dot{u}(t) + R\left(t\right) = F(t), \tag{4.4}$$

where $R(t)$ defines the nonlinear restoring force:

$$R\left(t\right)=\alpha\,k\,u\left(t\right)+\left(1-\alpha\right)k\,u_{y}\,z\left(t\right),\tag{4.5}$$

where k represents the yielding stiffness and u_y is the yielding displacement. The z term is a dimensionless hysteretic component provided by the solution of the following nonlinear differential equation that contains three state variables:

$$\dot{z}\left(t\right)=u_{y}{}^{-1}\left[A\dot{u}\left(t\right)\ -\gamma\left|\dot{u}\left(t\right)\right|\left|z\left(t\right)\right|^{n-1}z\left(t\right)-\beta\dot{u}\left(t\right)\left|z\left(t\right)\right|^{n}\right],\tag{4.6}$$

The shape and smoothness of each hysteretic loop is controlled by the parameters A, β, γ and n. Moreover, the term $\alpha = k_p/k_0$ in Eq. (4.5) defines the ratio of the postyielding stiffness to the preyielding stiffness, with

$$\begin{aligned}k_{0}&=\left(\frac{\partial R\left(u,\ \dot{u},\ z\right)}{\partial u}\right)_{z=0}=\alpha k+\left(1-\alpha\right)kA\ ,\\ k_{p}&=\left(\frac{\partial R\left(u,\ \dot{u},\ z\right)}{\partial u}\right)_{z=z_{\max}}=\alpha k_{0},\end{aligned}\tag{4.7}$$

and $z_{max}=[A/(\beta+\gamma)]^{1/n}$.

Suitable values of A, β, γ and n govern the hardening or softening nonlinearities in the Bouc–Wen model. For instance, with $|\gamma|>|\beta|, \gamma<0$, a hardening behavior is obtained. Moreover, the elastoplastic hysteresis case is approached when $n\to\infty$, where n modulates the sharpness of the yield. A choice of *n=1* entails a closed-form solution of Eq. 4.1 with simple exponential functions [119].

To identify the relevant mechanical characteristics, Paolacci and Giannini carried out an *ad hoc* experimental campaign [102]. On that database, we initialize the main parameters of the Bouc–Wen model. We select wire rope WR36-400-08, whose geometric dimensions are described in Tab. 4.1. In particular, k_0 is the initial shear stiffness, and R_v represents the vertical load-bearing capacity. The authors [101] found α = *0.254* and u_y = *2.2 mm*.

GEOMETRIC CHARACTERISTICS					
H [mm]	W [mm]	L [mm]	Φ [mm]		
178	216	520.7	26.6		
PARAMETERS OF THE Bouc–Wen MODEL					
k_0 [kN/mm]	R_y [kN]	u_y [mm]	n [-]	A [-]	α [-]
1.35	2.97	2.2	1.0	1.0	0.254

Table 4.1: Geometric and mechanical properties of the wire ropes

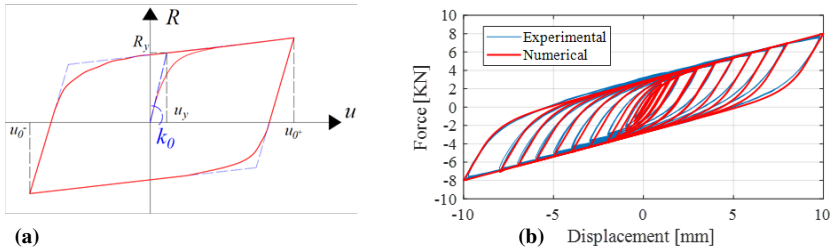

Figure 4.5: (a) Typical hysteretic loop of a Bouc–Wen model; (b) comparison between experimental and numerical responses after Paolacci and Giannini.

For the sake of clarity, two coupled wire ropes can be observed in the test rig of Fig. 4.4a; this arrangement allows cyclic simple shear tests to be reproduced by means of a central plate [101]. The corresponding hysteretic response is depicted in Fig. 4.4 (b).

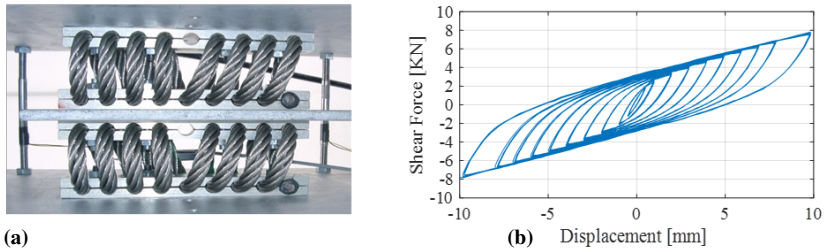

Figure 4.4: (a) Two wire ropes with a central plate subjected to simple shear; (b) hysteretic response of the wire rope under cyclic shear loading after Paolacci and Giannini.

A generic cycle of the Bouc–Wen model is shown in Fig. 4.5 (a) with the main mechanical and kinematic parameters. A careful reader will notice that this model is symmetric, as can be understood from Eq. (4.6); nonetheless, this property does not limit its capability to properly trace the experimental response depicted both in Fig. 4.4 (b) and Fig. 4.5 (b).

The data in Fig. 4.4 (b) and Fig. 4.5 (b) are obtained after Paolacci and Giannini [102]. Note that after choosing steel wire rope, the Bouc–Wen model parameters A and $(\beta + \gamma)$ can be functionally selected to be $A = 1$ and $\beta + \gamma = 1$. As shown by Constantinou and Adnane [120], this choice leads to the collapse of the model to Ozdemir's model, which is a rate-dependent Maxwell model with a nonlinear dashpot. By setting $A = 1$ in Eq. (4.6), indeed, the value of the initial stiffness $k = R_y / u_y = k_0$ is retrieved; then, by setting $\beta + \gamma = 1$, the maximum strength factor z_{max} in Eq. (4.7) becomes $z_{max} = [A/(\beta+\gamma)]^{1/n} = 1$ with $z \epsilon [-1, 1]$.

4.2.3 Seismic input model

Given the epistemic and mainly aleatoric uncertainties of the seismic input, it is not feasible to optimize a system endowed with nonlinear devices on a conventional time basis. A more accurate probabilistic (stochastic) approach is required in which both the excitation and the response are described in terms of statistical parameters such as the mean square and the variance of the vibration amplitudes. As a result, our approach relies heavily on random vibrations treated in the frequency domain, and stochastic linearization carried out in the next subsection. Therefore, the input is assumed to be a weakly stationary Gaussian-filtered white noise random process with zero mean and spectral intensity S_0. Consequently, the soil is approximately taken into account by means of the Kanai–Tajimi filter [116], and to avoid unrealistically high values of the excitation in the low-frequency range, we utilize an additional filter suggested by Clough and Penzien [117]. The result is the so-called Kanai–Tajimi Clough–Penzien (KTCP) filter, and the resulting PSD function is

$$S_{\ddot{u}_g}(\omega) = S_0 \, \frac{4\zeta_g^2\omega_g^2\omega^2 + \omega_g^4}{4\zeta_g^2\omega_g^2\omega^2 + \left(\omega_g^2 - \omega^2\right)^2} \; \frac{\omega^4}{4\zeta_f^2\omega_f^2\omega^2 + \left(\omega_f^2 - \omega^2\right)^2} \tag{4.8}$$

where $\omega_g = 14$ rad/s is the frequency associated with the ground and $\zeta_g = 0.6$ is the relevant damping ratio. The parameters $\omega_f = 0.75$ rad/s and $\zeta_f = 1.9$ are assumed for the low pass filter [117], whilst the PSD intensity $S_0 = 0.09$ m^2/s^3 for safe shutdown earthquakes (SSEs) corresponds to seismic activity with a return period of 2475 years. In the time domain, the KTCP filter becomes

$$\ddot{u}_g = \omega_g^2 u_g + 2\zeta_g\omega_g\dot{u}_g - \omega_f^2 u_f - 2\zeta_f\omega_f\dot{u}_f, \tag{4.9}$$

where some variables can be treated in a state-space formulation:

$$
\begin{aligned}
&\ddot{u}_g = \mathbf{a}_f{}^T \, \mathbf{u}_f, \\
&\dot{\mathbf{u}}_f = \mathbf{A}_f \, \mathbf{u}_f + \mathbf{V}_f \, \mathrm{f}(t)\mathbf{u}_f = \begin{bmatrix} u_f \\ \dot{u}_f \\ u_g \\ \dot{u}_g \end{bmatrix}, \\
&\mathbf{a}_f = \begin{bmatrix} -\omega_f^2 \\ -2\zeta_f\omega_f \\ \omega_g^2 \\ -2\zeta_g\omega_g \end{bmatrix}, \\
&\mathbf{A}_f = \begin{bmatrix} 0 & 1 & 0 & 0 \\ -\omega_f^2 & -2\zeta_f\omega_f & \omega_g^2 & 2\zeta_g\omega_g \\ 0 & 0 & 0 & 1 \\ 0 & 0 & -\omega_g^2 & -2\zeta_g\omega_g \end{bmatrix}, \\
&\mathbf{V}_f = \begin{bmatrix} 0 \\ 0 \\ 0 \\ 1 \end{bmatrix},
\end{aligned}
\tag{4.10}
$$

where *f(t)* denotes the bedrock Gaussian zero-mean white noise process. Both the filter parameters and the PSD intensity S_0 are chosen to fit the stationary PSD spectra of 12 natural seismic records (see Tab. 4.2) selected from Italian and European databases with a 2% probability of exceedance in 50 years.

The corresponding elastic response spectra, their mean and their mean plus one standard variation, together with the target uniform hazard spectrum (UHS) relevant to Priolo Gargallo, are plotted in Fig. 4.6. The twelve records collected in Tab. 4.2 are selected as follows. Let s_0 be the target spectrum value vector, i.e., the mean or the mean plus one standard deviation, let $\mathbf{S}$ be the spectra matrix of the n_a accelerograms, and let α be the vector of the $n_a \times 1$ selection coefficients α_i. We seek for the vector α that satisfies

$$
\left\| \frac{1}{\sum_{i=1}^{n_a} \alpha_i} \mathbf{S}\alpha - \mathbf{s}_0 \right\|^2 = \min, \tag{4.11}
$$

where $0 \leq \alpha_i \leq 1$, and $\sum_{i=1}^{n_a} \alpha_i = n$. Hence, the selection is performed with all possible combinations of the *n* accelerograms among a set of

EVENT	COUNTRY	R [Km]	M
Victoria Mexico	Mexico	13.8	6.33
Loma Prieta	USA	3.85	6.93
Northridge-01	USA	20.11	6.69
Montenegro	Montenegro	25.00	6.90
Erzincan	Turkey	13.00	6.60
South Iceland	Island	7.00	6.50
L'Aquila Mainshock	Italy	4.87	6.30
Loma Prieta	USA	11.03	6.93
Landers	USA	11.03	7.28
South Iceland	Island	11.00	6.40
L'Aquila Mainshock	Italy	4.63	6.30
L'Aquila Mainshock	Italy	4.39	6.30

Table 4.2: Selected natural accelerograms; R is the distance between the epicenter of the seismic event, and M is its magnitude.

n_a records. Thus, we can easily take into account the dispersion of the records about the mean spectrum. The discrepancy between the maximum peak of the two spectra, i.e. the UHS and the Mean Spectrum + σ should entail limited effects on the responses of the nonlinear coupled systems presented in the section *Results*.

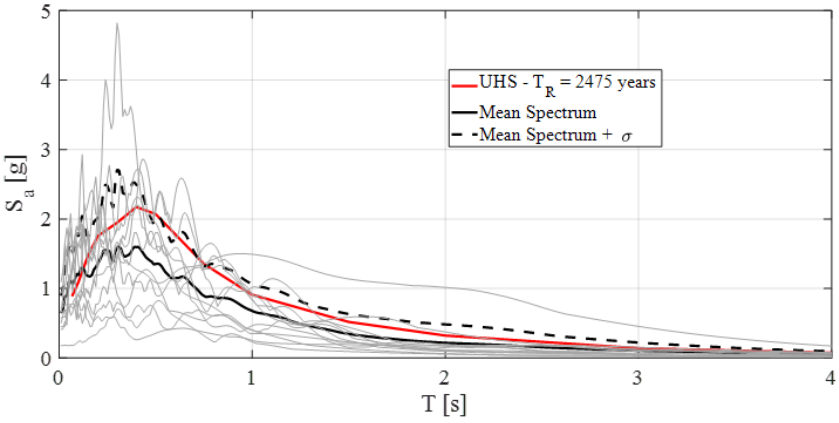

Figure 4.6: Response spectra of the selected accelerograms for SSEs; the UHS of Priolo Gargallo (Italy) is depicted in red.

4.2.4 Equivalent linearization and optimization procedure

To model the wire ropes illustrated in Fig. 4.2 (b), which are not easily treated mathematically, we propose the stochastic linearization technique [113]. As a result, the treatment of the linearized metafoundation-tank coupled system allows the optimization procedure to be performed in the frequency domain and bypasses several difficulties related to the determination of the dispersion properties of fully nonlinear periodic systems [107]. With regard to the parameters to be optimized, to maximize antiresonance or negative effects, the masses of the resonators are set as the largest masses compatible with unit cell dimensions. Moreover, the other parameters are derived from construction or design constraints, e.g., the design column size and slab thickness; therefore, mainly the stiffness and damping of wire ropes, i.e., the relevant dissipated energy controlled by the parameters of Eqs. (4.5) and (4.6), can be optimized.

Since the system of EOMs in Eq. 4.1 characterizes a coupled nonlinear system, classic linear random vibration theory is not applicable. Therefore, to linearize the vector $\mathrm{u_y}\mathbf{K}^{\mathrm{NL}}\mathbf{z}(\mathrm{t})$, we employ the ELT. For the sake of clarity, for an SDoF system with *N = 1*, Eq. (4.6) becomes

$$\dot{z} + c_{eq}\dot{u} + k_{eq}z = 0, \tag{4.12}$$

where c_{eq} and k_{eq} are linearization coefficients that are "equivalent" in a statistical sense [121, 122]. At this stage, it is useful to introduce a state-space formulation of Eqs. (4.1) and (4.12):

$$\frac{d}{dt}\mathbf{Y} = \mathbf{G}\ \mathbf{Y} + \mathbf{V}\ f(t), \tag{4.13}$$

with

$$\begin{aligned}
\mathbf{Y} &= \begin{bmatrix} \mathbf{u} \\ \dot{\mathbf{u}} \\ \mathbf{z} \\ \mathbf{u}_f \end{bmatrix}, \\
\mathbf{G} &= \begin{bmatrix} \mathbf{0}_{N\mathrm{x}N} & \mathbf{I}_{N\mathrm{x}N} & \mathbf{0}_{N\mathrm{x}N} & \mathbf{0}_{N\mathrm{x}r} \\ -\mathbf{M}^{-1}\,\mathbf{K}^{L} & -\mathbf{M}^{-1}\,\mathbf{C} & -\mathbf{M}^{-1}\,\mathbf{K}^{NL} & -\mathbf{1}\,\mathbf{a}_f{}^{T} \\ \mathbf{0}_{N\mathrm{x}N} & -\mathbf{c}_{eq} & -\mathbf{k}_{eq} & \mathbf{0}_{N\mathrm{x}r} \\ \mathbf{0}_{r\mathrm{x}N} & \mathbf{0}_{r\mathrm{x}N} & \mathbf{0}_{r\mathrm{x}N} & \mathbf{A}_f \end{bmatrix}, \\
\mathbf{V} &= \begin{bmatrix} \mathbf{0}_{N\mathrm{x}1} \\ \mathbf{0}_{N\mathrm{x}1} \\ \mathbf{0}_{N\mathrm{x}1} \\ \mathbf{V}_f \end{bmatrix},
\end{aligned} \tag{4.14}$$

where $\mathbf{Y}$ is the state-space vector, $\mathbf{K}^L$ and $\mathbf{K}^{NL}$ define the linear and nonlinear components of the stiffness matrix, respectively, and $\mathbf{k}_{eq}$ and $\mathbf{c}_{eq}$ represent matrices including equivalent linear coefficients. Moreover, *N* defines the number of DoFs of the system, and $r = 4$ defines the number of equations of the KTCP filter introduced in the previous subsection. Let the covariance matrix of $\mathbf{Y}$ be $\mathbf{S}$ with $S_{ij} = E[y_i, y_j]$, and assume that the seismic input is stationary. The solution of Eq. (4.13) can be derived from the following Lyapunov system of equations:

$$\mathbf{G}\,\mathbf{S} + \mathbf{S}\,\mathbf{G}^T + \mathbf{B} = \mathbf{0}, \tag{4.15}$$

where $\mathbf{B}$ is a zero matrix except for the generic diagonal element corresponding to the nonzero row of the forcing function vector, i.e., $B_{ij} = 2\pi S_0$. Eq. (4.15) is solved with the algorithm proposed by Bartels and Steward [123]. As expected, $\mathbf{k}_{\text{eq}}$ and $\mathbf{c}_{\text{eq}}$ are not known a priori; in this regard, Maldonado et al. [121] suggested setting the initial values for an iterative solution procedure $c_{eq} = 1$ and $k_{eq} = 0.05(\beta + \gamma)$ for faster convergence. Further details about the whole procedure are available in Maldonado et al. [121] and Spanos et al.. [124].

To operate in the frequency domain, we start from Eq. (4.4) for a SDoF system and define the transfer function $H(\omega)$ of the coupled system depicted in Fig. 4.3. However, Eq. (4.13) includes the KTCP filter, and the derivation is more burdensome for an MDoF system. Therefore, the relevant $H(\omega)$ becomes

$$\mathrm{H}\,(\omega) = \left[-\omega^2 m + i\omega c + \alpha k - \frac{i\omega}{i\omega + k_{eq}} c_{eq}\,(1-\alpha)\,k u_y\right]^{-1}, \tag{4.16}$$

where the details of the derivation can be found in the Appendix B. Its generalization is expressed as

$$\mathbf{H}\,(\omega) = \left[-\omega^2 \mathbf{M} + i\omega\ \mathbf{C} + \mathbf{K}\ +\ \mathbf{K}^{\text{eq}}\right]^{-1}, \tag{4.17}$$

where contains zero terms except those in which the n^{th} resonator is physically connected. More precisely, the nonzero terms of matrix are

$$k_{ij}^{eq} = -\frac{i\omega}{i\omega + k_{eq}} c_{eq}\,(1-\alpha_n)\,u_y\,k_n, \tag{4.18}$$

where α_n and k_n refer to the n^{th} resonator of the metafoundation. Note that for $\alpha = 1$, the transmission matrix in Eq. (4.17) degenerates into a linear transmission matrix.

To carry out the optimization, we minimize the interstorey displacement and the absolute acceleration of the tank's impulsive mode, where the relevant variances σ_{dr} and σ_{acc}, respectively, are expressed as

$$\sigma_{dr}^2 = \int_0^{+\infty} \left|\mathrm{H}_{imp}(\omega) - \mathrm{H}_{res}(\omega)\right|^2 S_{\ddot{u}_g}(\omega)\, d\omega,$$
$$\sigma_{acc}^2 = \int_0^{+\infty} \left|1 - \omega^2 \mathrm{H}_{imp}(\omega)\right|^2 S_{\ddot{u}_g}(\omega)\, d\omega, \tag{4.19}$$

where $H_{imp}(\omega)$ defines the transfer function of the impulsive mass and $H_{res}(\omega)$ is the transfer function of the resonator's layer. The dimensionless performance indices are defined as follows:

$$\mathrm{PI_{dr}} = \frac{\sigma_{dr}^2}{\sigma_{dr,fixed}^2},$$
$$\mathrm{PI_{acc}} = \frac{\sigma_{acc}^2}{\sigma_{acc,fixed}^2}, \tag{4.20}$$

where $\sigma_{dr,fixed}^2$ and $\sigma_{acc,fixed}^2$ represent the variances of the interstorey drift and the absolute acceleration, respectively, wrt a clamped tank.

The optimization procedure relies on the design variables $k_{k,n}$ and $\beta_{k,n}$ collected in the parameter vector $\mathbf{X}^{NL}$:

$$\mathbf{X}^{\mathrm{NL}} = [k_{1,1},\ k_{k,n},\ A_{1,1},\ A_{k,n},\ \beta_{1,1},\ \beta_{k,n},\ \gamma_{1,1},\ \gamma_{k,n}]^{\mathrm{T}}. \tag{4.21}$$

The statement of our optimization problem is as follows:

$$\min_{k,n}\ \mathrm{PI}_{dr}\left(\mathbf{X}^{\mathrm{NL}}\right) \ \text{ or } \min_{k,n}\ \mathrm{PI}_{acc}\left(\mathbf{X}^{\mathrm{NL}}\right) \tag{4.22}$$

where $k = (1, \ldots, n_k)$ and $n = (1, \ldots, n_r)$. The limits imposed on the design variable $\beta_{k,n}$ are

$$0 \ < \beta_{k,n} < \ 1. \tag{4.23}$$

Further details about the bound of Eq. (4.23) were already provided in the subsection *Modelling of nonlinear devices*.

4.2.5 Dispersion characteristics of the linearized periodic system

Though the system is linearized by means of Eq. (4.11), the effects of the nonlinear devices depicted in Fig. 4.2 on the band structure of the relevant periodic system are of interest. On the one hand, we can observe the effect of equivalent damping on the dispersion relationships; on the other hand, we can appreciate the effects of the PSD S_0.

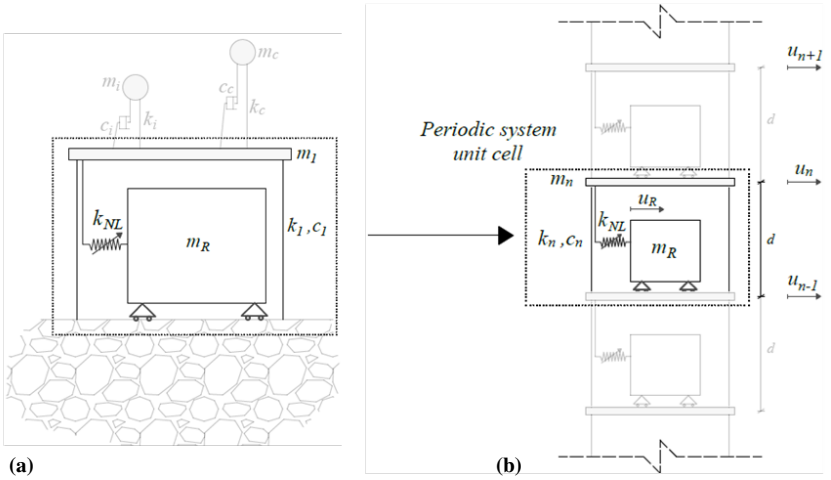

Figure 4.7: Dynamic systems: (a) coupled finite lattice metafoundation-tank system; (b) metafoundation modeled as a periodic system.

First, let us consider Fig. 4.7, which shows both the finite lattice 1-layer structure, see Fig. 4.7 (a) and the relevant system of repetitive unit cells depicted in Fig. 4.7 (b).

The 2-DoF system associated with the unit cell, i.e., slab and resonator of Fig. 4.7 (b), can be represented as follows:

$$\begin{cases} m_n\ddot{u}_n + c_n(\dot{u}_n - \dot{u}_{n-1}) + c_n(\dot{u}_n - \dot{u}_{n+1}) + k_n(u_n - u_{n-1}) \\ +k_n(u_n - u_{n+1}) - \alpha k_0(u_R - u_n) - (1-\alpha)k_0 u_y z(t) = 0, \\ \\ m_R\ddot{u}_R + \alpha k_0(u_R - u_n) + (1-\alpha)k_0 u_y z(t) = 0, \end{cases}$$

where dots refer to time differentiation. We assume the following harmonic solution for displacements:

$$\begin{aligned} u_n &= \tilde{u}_n e^{i\omega t}, \\ u_R &= \tilde{u}_R e^{i\omega t}, \end{aligned} \tag{4.24}$$

where $\tilde{u}_n$ and $\tilde{u}_R$ are displacement amplitudes. In addition, the FB theorem can be applied as

$$\begin{aligned} u_{n+1} &= \tilde{u}_n e^{i\mu}, \\ u_{n-1} &= \tilde{u}_n e^{-i\mu}, \end{aligned} \tag{4.25}$$

where $\mu = \kappa d$ defines the so-called propagation constant based on the wavenumber κ and the unit cell length d. Thus, the application of the

ELT by means of Eqs. (4.11) and (4.17) and the conditions of Eqs. (4.24) - (4.25) to the system of Eq. (4.24) entails the following:

$$\begin{cases} \left[-\omega^2 m_n + 2k_n + 2i\omega c_n + \alpha k_0 - \frac{i\omega}{i\omega+k_{eq}} c_{eq}(1-\alpha)k_0 u_y\right] u_n \\ + \left[-\alpha k_0 + \frac{i\omega}{i\omega+k_{eq}} c_{eq}(1-\alpha)k_0 u_y\right] u_R \\ -(k_n + i\omega c_n)(e^{-i\mu} + e^{i\mu})u_n = 0, \\ \\ u_R = \frac{\alpha k_0 - \frac{i\omega}{i\omega+k_{eq}} c_{eq}(1-\alpha)k_0 u_y}{-\omega^2 m_n + \alpha k_0 - \frac{i\omega}{i\omega+k_{eq}} c_{eq}(1-\alpha)k_0 u_y} u_n. \end{cases} \tag{4.26}$$

The substitution of u_R into the first equation of Eq. (4.26) leads to the following dispersion relation:

$$\mu = Cos^{-1}\left(\frac{-\omega^2 m_n + 2k_n + 2i\omega c_n + \alpha k_0 - \frac{i\omega}{i\omega+k_{eq}} c_{eq}(1-\alpha)k_0 u_y + \frac{\left[-\alpha^2 k_0^2 + 2\alpha k_0 \frac{i\omega}{i\omega+k_{eq}} c_{eq}(1-\alpha)k_0 u_y - \left(\frac{i\omega}{i\omega+k_{eq}} c_{eq}(1-\alpha)k_0 u_y\right)^2\right]}{-\omega^2 m_R + \alpha k_0 - \frac{i\omega}{i\omega+k_{eq}} c_{eq}(1-\alpha)k_0 u_y}}{2(k_n + i\omega c_n)} \right), \tag{4.27}$$

in the $(\mu - \omega)$ plane.

4.3 Results

4.3.1 Optimization and time-history analysis results

The optimization and time history analyses based on the methods discussed at length in the previous section are presented and discussed herein. We set n, α and u_y based on the properties described in Tab. 4.1, and we search for the optimal values of k, β and γ with the constraints [120] $A = 1$ and $\beta + \gamma = 1$. The results of the optimization process based on the index PI_{dr} introduced in Eq. (4.20) are depicted in Fig. 4.8 for the CMS model. The minimum value of $PI_{dr} = 0.78$, i.e., the red point on the $\beta - k_{0,opt}$ plane, corresponds to $k_{0,opt} = 56.8$ KN/mm and $\beta_{opt} = 0.9$. β and γ quantify the dissipation characteristics of wire ropes, and with $\beta+\gamma = 1$, $\gamma^{opt} = 0.1$. Notably, $k_{0,opt}$ corresponds to the horizontal stiffness of a single resonator of the metafoundation. Similar values can be obtained by means of the index PI_{acc}.

To test the performance of the metafoundation-tank coupled system, THAs are carried out considering the hysteretic responses of the devices in agreement with Eq. (4.5). Fig. 4.9 shows the hysteretic loops of a single wire rope when the CMS model is subjected to one of the 12 accelerograms listed in Tab. 4.2. The term u_{res} represents the displacement of the generic resonator wrt u_{tl}, i.e., the displacement of the top of the metafoundation. Fig. 4.9a refers to the optimized system where 42 wire

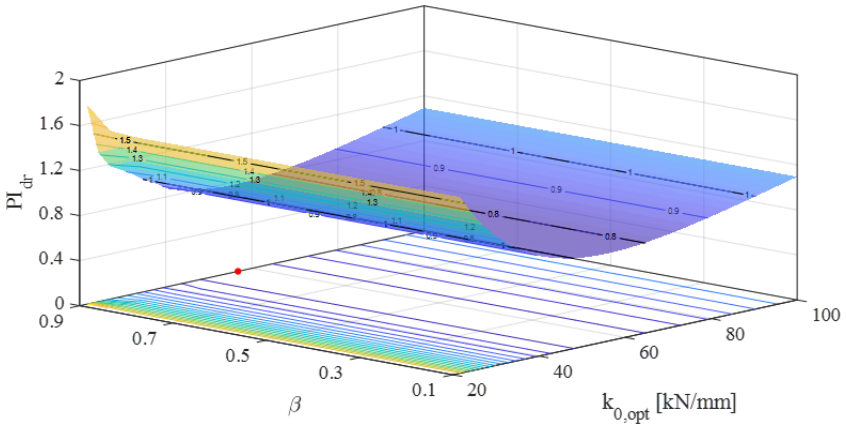

Figure 4.8: Optimal surface for the linearized CMS case.

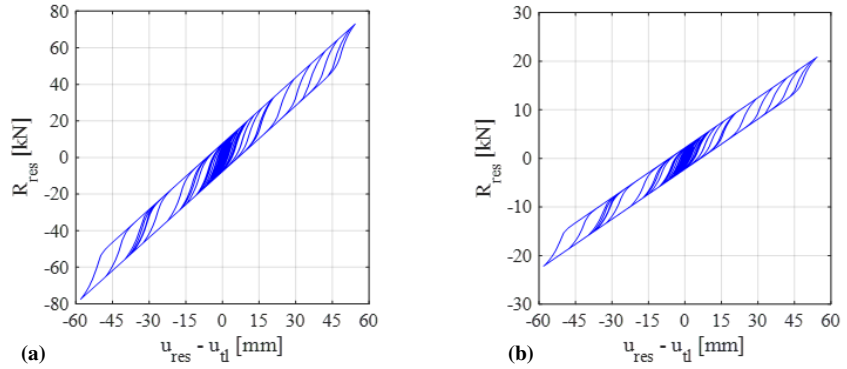

Figure 4.9: Hysteretic loops of the one-layer CMS hysteretic damper for $A = 1$, $\beta = 0.9$ and $\gamma = 0.1$. The resonators are equipped with the (a) optimal and (b) minimum numbers of wire ropes.

ropes per resonator are needed. Conversely, Fig. 4.9 (b) refers to the system provided with the minimum number of wire ropes required to support a resonator, i.e., 16 wire ropes.

To appreciate the performance of the optimized CMS finite lattice metafoundation, Fig. 4.10 depicts both the maximum and the median parameter values of the nonlinear foundation-tank coupled system wrt the fixed-base solution when subjected to the 12 seismic records listed in Tab. 4.2. The maximum values of the base shear V, absolute acceleration a and interstorey drift d of the impulsive mass are reported. Nonlinear devices are characterized by β and γ equal to 0.9 and 0.1, respectively. The favourable performance of the metafoundation, which achieves reductions of approximately 21%, 10% and 19% in V, a, and d, respectively, wrt the fixed-base case, is evident.

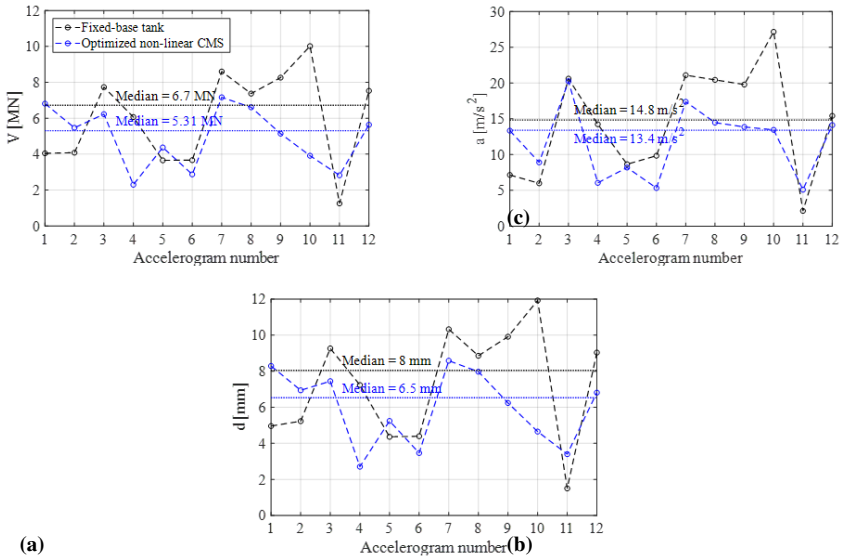

Figure 4.10: Maximum and median values of the (a) base shear, (b) absolute acceleration and (c) interstorey drift of the optimized nonlinear CMS wrt the fixed-base tank for each accelerogram listed in Table 2.

Finally, Fig. 4.11 shows the maximum and median values of the wire rope displacements in the optimized nonlinear CMS model relevant to each time history. The maximum displacements reach approximately 90 mm with a median equal to 50 mm. These demand values are compatible with the capacities of standard wire ropes.

4.3.2 Dispersion curves of the linearized periodic system

For the sake of completeness, it is worthwhile to examine some wave propagation properties of the decoupled metafoundation depicted in Fig. 7 and modeled as a periodic system in Fig. 4.7 (b). We rely on the ELT applied to nonlinear devices so that we are able to trace the mode shape families, i.e., the dispersion curves or band structures, defined by means of wavelengths — inversely, wavenumbers — and frequencies. As the linearized hysteretic system exhibits a significant amount of damping, see Eqs. (4.15) and (4.16), the damped periodic materials can be characterized by means of i) complex wavenumbers as a function of real frequencies and ii) complex frequencies as a function of real wavenumbers. We adopt the former methodology, where the dispersion relationships are obtained with Eq. (4.27) in terms of $\mu(\omega)$. This condition corresponds to a harmonic wave motion where a driving frequency ω is prescribed. The values of the propagation constant $\mu(\omega)$ are all complex due to the

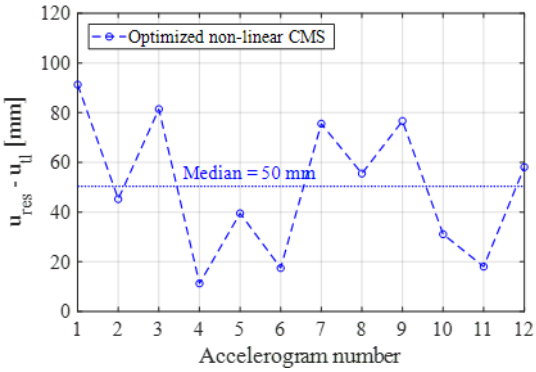

Figure 4.11: Maximum and median values of wire ropes for the optimized non-linear CMS for each time history.

presence of damping. The relevant dispersion relationships representative of the periodic metafoundation depicted in Fig. 4.7 (b) are shown in Fig. 4.12. The relationships are expressed by real values of μ corresponding to the propagative index of waves, while the imaginary components of μ, often called the attenuation constant, define the spatial decay of the amplitude as the wave progresses through the lattice.

Each dispersion curve shown in Fig. 4.12 is associated with a different value of k_{eq} that, due to the linearization process, depends on the input PSD S_0. Standard ELT results [121, 122] show that an increase in S_0 from 0.03 to 0.36 m^2/s^3 entails an increase in k_{eq} — 83, 177, 273 and 410 — whilst c_{eq} remains essentially unchanged and equal to $c_{eq} = -269$. As shown by Spanos and Giaralis [122], k_{eq} and c_{eq} are derived from a third-order ELT whose values do not correspond to any particular mechanical system; hence, their physical significance is limited. Conversely, if we rely on a second-order statistical linearization scheme [122] governed by the linearization parameters ζ_{eq} and ω_{eq}, this leads to a trend where an increase in S_0 corresponds to a reduction in ω_{eq}, as understood from Fig. 4.12a. Note that for the highest value of S_0, i.e., almost an undamped-like structure, the curve tends to create a bandgap. In that area, the μ values are higher for curves with less damping. Finally, with regard to waves travelling at frequencies that belong to the passband of μ_R, higher damping values entail greater spatial wave attenuation.

4.3.3 Numerical investigation of the periodic system

In contrast to the previous subsection, where we considered a linearized periodic system, in this section we carry out numerical simulations on the

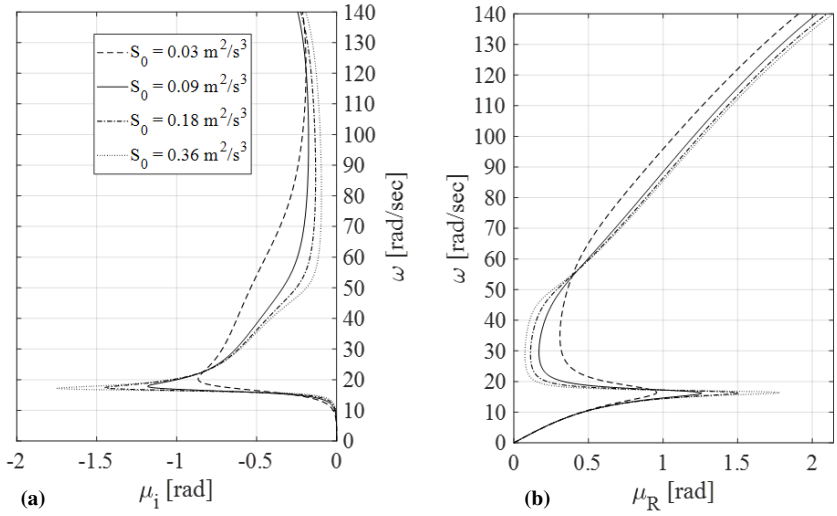

Figure 4.12: Periodic metafoundation dispersion curves: (a) imaginary component of μ; (b) real component of μ.

metafoundation's periodic configuration depicted in Fig. 4.7 (b); thus, we do not make any assumptions about the nonlinearities involved. The system is excited by a time-harmonic displacement A_0 applied to the bottom layer. The output response A is read from the top layer. The boundary condition of the system of masses is free-free, and since the system is not excited by a force, rigid-body motion is avoided. The frequency response function (FRF) is then evaluated as

$$FRF = 20 \log_{10} \frac{A}{A_0}, \tag{4.28}$$

where A is the maximum amplitude of the steady-state response and A_0 is the amplitude of the harmonic excitation. The resulting wave transmittances are plotted in Fig. 4.13.

The FRFs of Fig. 4.13 are clearly amplitude dependent because the system is nonlinear. However, the wave transmittances in Fig. 4.13 (a) for low frequencies show that the modal resonances do not depend strongly on the amplitude excitation. This is clearly confirmed by the linearized band structure observed in Fig. 4.12, where the acoustic branch appears to be identical for each S_0. Nevertheless, the identification of an optical branch is simpler for high amplitudes, i.e., $A_0 = 25cm$; in fact, the presence of resonance points becomes evident.

We can also identify a strong attenuation zone comparable to the band gap. The width of the band gap varies with the displacement amplitude. A wide and deep band gap can be observed under small-amplitude

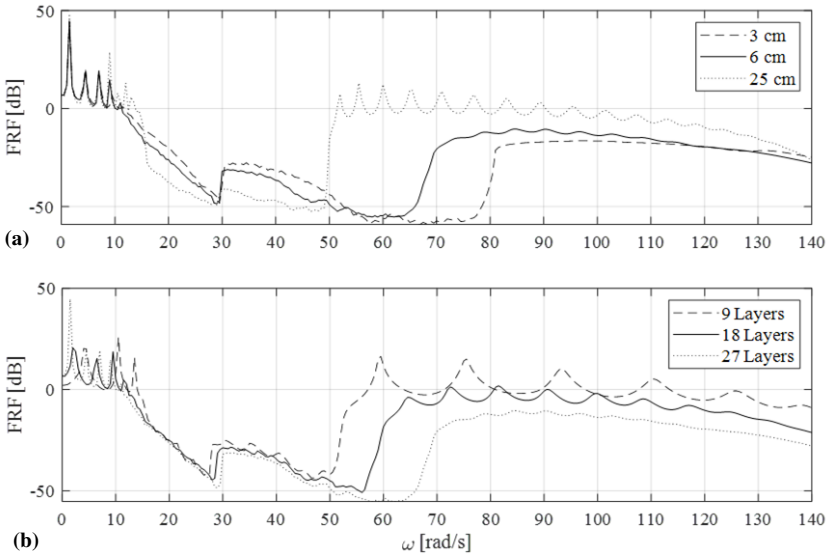

Figure 4.13: Numerical FRFs of a periodic finite lattice: a) FRF for several input amplitudes A_0 for 27 layers; b) FRF for several layers for A_0 = 6 cm.

excitations, whereas the width and depth of the band gap are reduced by increasing the input amplitude. This leads to a worse wave attenuation performance of the hysteretic system under high-amplitude vibrations. The performance of the periodic hysteretic system can also be evaluated by means of Fig. 4.13 (b) for $A_0 = 6$ cm. It is clear that the performance level increases in terms of the width and depth of the band gap as the system is characterized by more layers. Moreover, it is worth noting that both FRFs identify an attenuation zone accurately predicted by the linearized dispersion curves of Fig. 4.12. In fact, the trend of the imaginary components of μ is centred at the resonator's linearized frequency $\omega_R = (\alpha k_0/m_R)^{1/2} = 16,9$ rad/s. Fig. 4.13 consistently shows that for frequencies ranging from approximately 15 to 20 rad/sec, the FRF starts to decrease. Finally, note that the stiffness αk_0 corresponds to the slope of the hardening branch of the Bouc–Wen model in Eq. (4.7).

4.4 Discussion

The objective of this work was to conceive a metafoundation bearing oil storage tanks capable of inheriting the filter properties of finite lattice phononic structures. More precisely, the vibrations in the frequency regime induced by seismic records are attenuated by the favourable properties of coupled hysteretic devices and resonators embedded in the metafoun-

dation. The metafoundation is composed of massive vibrating concrete blocks that are coupled to the slabs by means of fully nonlinear hysteretic devices. Moreover, to achieve cost savings, the foundation is constituted by a single layer of resonators.

To identify the effective properties of nonlinear hysteretic devices in terms of stiffness and equivalent damping, an optimization procedure was carried out by minimizing two dimensionless performance indices based on the variances of the interstorey displacement of the impulsive mass and of the relevant absolute acceleration. Because the optimization procedure has to be carried out in the frequency domain for linear time-invariant systems subjected to stationary seismic records, we applied the stochastic linearization technique [111] to the nonlinear hysteretic devices embedded in the metafoundation. As a result, the optimized metafoundation-tank coupled system performed well when subjected to natural seismic records carried out in the time domain. In addition, we determined the dispersion relations for the periodic linearized spring–mass chain, see Fig. 4.7 (b), which clearly depends on the PSD S_0 amplitude. As a result, the maximum attenuation rate depicted in Fig. 4.12 increases with an increase in S_0 and a decrease in the equivalent damping ζ_{eq} in the resonators.

Furthermore, we investigated the nonlinear response of the periodic metafoundation by means of numerical FRFs. The results confirm the reliability of the dispersion analysis subsequent to applying the equivalent linearization technique. In fact, a strong attenuation zone in the FRF is located in the frequency range where the dispersion curves indicate very high values of the imaginary propagation constant μ_i.

The results achieved herein reveal a promising application of finite lattice metafoundations to large systems subjected to strong seismic excitations. However, in addition to a sound application of finite lattice metafoundations for large systems subjected to strong seismic excitations, this work paves some ways: i) the application of stochastic linearization to a finite lattice allows the metafoundation-tank coupled nonlinear system to be optimized while capturing the variability of the seismic input, and ii) the use of simple hysteretic devices such as wire ropes permits the 3D motion of massive resonators and reflect the great effectiveness and potential of these devices as vibration mitigation tools.

Ultimately, the validation of these results by means of the 3D physical characterization of hysteretic devices as well as the analysis of nonlinear wave mechanisms through nonlinear spatial analyses deserves further study.

5.0 Periodic damped pipeline attenuation zones and optimal stochastic dynamic performance of a pipe-rack equipped with an impact device

This chapter contains the post-print of:

Fabrizio Aloschi, Roberto Andreotti, and Oreste S. Bursi. Pipe vibration attenuation through internal damping and optimal design of vibro-impact systems. *Scientific Reports*, 13(1):6510, 2023,

as published in the Journal *Scientific reports, Nature Research*, differing from the published paper only in terms of layout and formatting.

Pipelines periodically supported by rack structures (PPRs) are common in chemical and petrochemical plants, among others, and conventional tools such as dampers and hysteretic absorbers are commonly used to mitigate large vibrations in these systems. In this study, we explore two alternative strategies: (i) enhancing the attenuation rate of PPR vibrations through structural internal damping, and (ii) using nonlinear vibro-impact systems (VIS) to reduce seismic vibrations in a PPR. To shed light on the first strategy, we develop analytical dispersion relations for a PPR and show how damping can improve the mitigation capabilities of the periodic system. As for the second strategy, we consider a 9-node beam, i.e., a single span (SS) of a PPR equipped with a VIS, and combine the central composite design (CCD) and Kriging metamodelling to maximize dissipation energy and minimize the number of impacts. This multi-objective optimization problem aims to find the most effective design solution for the VIS in terms of gap and coefficient of restitution (COR). Additionally, we consider the stochastic nature of seismic input and the possible chaotic behavior of the VIS. To account for the sensitive variability of the number of impacts in seismic records, we perform incremental dynamic analyses (IDA) and calculate fragility functions for various engineering demand parameters (EDP), including the number of impacts. We define a 3D surface for selecting the optimal gap-COR pair.

When impacts occur, transient results can be chaotic, and we compute the largest Lyapunov exponents of a few representative trajectories.

5.1 Introduction

Pipelines supported by rack structures (PPRs) are a crucial means of carrying liquefied gas in different types of plants, such as liquefied natural gas plants, thermal power plants, petroleum industries, and chemical plants. These structures have demonstrated vulnerability to excessive vibrations [125, 126, 127], such as ground-borne vibrations [128, 129, 130, 131, 132, 133] and flow-induced turbulence [134, 135, 136, 137]. To mitigate vibrations, researchers have exploited bandgaps and attenuation zones exerted by periodically arranged structures. In some research works, Bloch waves have been applied to long, distributed infrastructures, such as bridges [138, 42], and pipes [43, 139, 140]. The dispersion analysis of Iqbal et al. [43] revealed the dynamic flexural behavior of long supported pipes modeled as an infinite periodic structure. However, none of these works took into account the supplemental dissipation that damping [141, 142] may provide to continuous systems.

Researchers have also used linear and nonlinear external tools to attenuate large vibrations, such as pounding tuned mass dampers (PTMD) [143], pipe-in-pipe systems [144], multi-stage dampers [145], and Stockbridge dampers [146]. Song et al. [143] developed a numerical analysis based on the Hertzian contact to model the pounding force and performed experimental tests on a pipeline coupled with a PTMD. The presence of the PTMD increased the damping ratio and effectively induced amplitude attenuation; nonetheless, this device is complicated to design since it combines vibro-impact and TMD. In this work, we exploit the impact phenomenon [147, 45, 46, 148, 149, 150, 151, 152, 153, 154, 155, 156, 157, 158, 159, 160] with a nonlinear device that constrains the amplitude displacement of the pipe's interface.

Conventional linear dampers, such as TMDs, are not always recommended for vibration mitigation due to their low performance under certain conditions caused by detuning effects [44]. Moreover, they may not be sufficient to mitigate the abrupt flow-induced increases of velocity. In such cases, impact-based dissipation systems serve as a powerful alternative [147]. However, high-velocity impacts can cause large deformations near the contact area, eventually leading to system design difficulties. Therefore, the design optimization of dissipative vibro-impact systems (VIS) needs further study. To the best of our knowledge, it is difficult to estimate the frequency response function of a nonlinear VIS and com-

pare it with that of a TMD system, as a VIS often exhibits non-periodic motion. Additionally, TMDs have limitations in terms of their ability to suppress a broader range of frequencies [45, 46], and as such, nonlinear systems have become the preferred choice for this purpose. Hysteretic quadratic nonlinearity devices [148], energy sinks [149, 150], nonlinear vibration absorbers [151, 152], and other nonlinear systems have proven to be effective in suppressing broader frequency ranges.

Within this framework, the mitigation of dynamic vibration in PPRs is performed by means of two main strategies: i) the attenuation properties of PPR models by means of internal damping; ii) the optimized performance of a VIS subjected to stochastic (seismic) loading. Fig. 5.1 schematically depicts the two strategies employed.

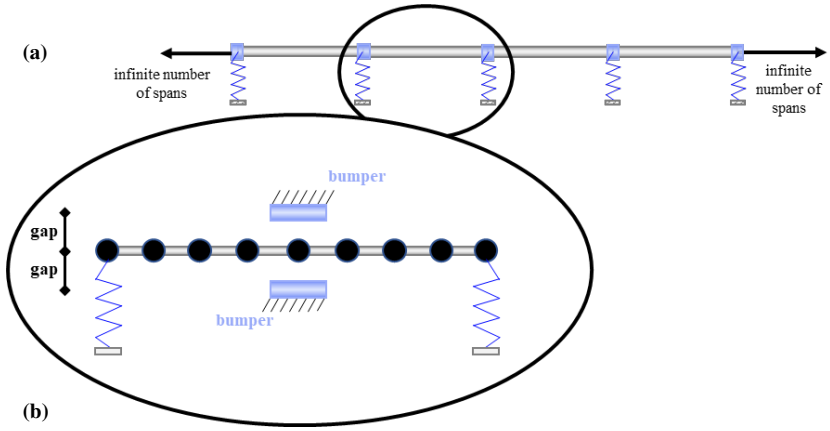

Figure 5.1: (a) Periodic damped pipeline on flexible supports and (b) single span (SS) endowed with bumpers for impact-based energy dissipation.

In particular, Fig. 5.1 (a) shows a linear PPR; the attenuation zones due to internal damping will be obtained by applying dispersion analysis to a single cell. Fig. 5.1 (b) depicts, instead, a single span (SS) of a pipeline equipped with the VIS. The relevant nonlinear dissipation system is optimized in terms of maximum dissipation energy and minimum number of impacts when subjected to stochastic excitations. To model the impact phenomenon, a non-smooth approach is adopted with an algorithm that combines instantaneous and finite duration contact [153, 154, 155]; pipes and bumpers are assumed to be rigid bodies, and the COR is given by Newton's impact law. To further streamline the computational effort, we adopt the CCD, along with the Kriging metamodel implemented in UQLab [161]. Both Kriging metamodelling and response surface methodologies (RSM) in general [162] provide the designer with an overall perspective of the system's response within the design domain,

which in this paper are the gap and the COR. RSM is indeed a common tool for design optimization problems [163, 164, 165, 166, 167], especially for those cases where the input is (seismic) stochastic, and the system's response is nonlinear. In this respect, among many interesting features of the dynamics of impacts, bifurcation and chaos have gained much attention over the last few decades. Two basic characteristics of chaos as a dynamical state are commonly discussed [158, 159, 160]: i) the chaos pertains to a pseudorandom behavior observed in a deterministic nonlinear dynamical system, i.e., the system's output appears to be statistically random despite having been produced by a deterministic and repeatable process; ii) the chaos causes a sensitive dependence on initial conditions, thus the initial states of close trajectories exponentially separate; the rate of separation over time is identified by the Lyapunov exponent. Shaw [158] experimentally tested an elastic beam with a one-sided displacement constraint under periodic excitation and reported nonlinear features of the beam, such as subharmonic resonances, period doublings, and chaotic regimes. The results were validated with the analytical model of a single oscillator with periodic excitation and a piecewise linear restoring force. Coexistent attractors and multi-stability appeared in the impact oscillator of Costa et al. [160], and the existence of chaos was proven with the 0-1 test and the Lyapunov exponents [168].

Nonetheless, the design problem of a chaotic deterministic system under (seismic) stochastic loading, such as earthquakes, still needs to be deepened. To handle this task, the design optimization procedure of a pipe with vibro-impact is complemented with a fragility assessment. Fragility functions usually derive from a variety of approaches like static structural analyses, judgment, or field observations of damage. In this work, we derive the so-called analytical fragility functions from incremental dynamic analyses (IDA) [169, 170, 171]. Given the unpredictability of the number of impacts due to chaos, the fragility function will be defined by a surface [172] for a variety of damage states (DM). Just to prove the existence of chaos in the SS depicted in Fig. 5.1 (b), a few chaotic trajectories and the bifurcation diagrams are reported in the Supplementary Information. They have been evaluated for certain ranges of frequencies in the vicinity of the natural frequency of the SS, and the largest Lyapunov exponents have been estimated. Due to the nonlinear dependence of the dispersion features upon amplitude and frequency of excitation, this last task has required periodic excitation with multiple amplitudes.

5.2 Methods

5.2.1 Internal and external damping models in periodic PPRs

We intend to improve the attenuation properties of the two periodic PPRs depicted in Fig. 5.2.

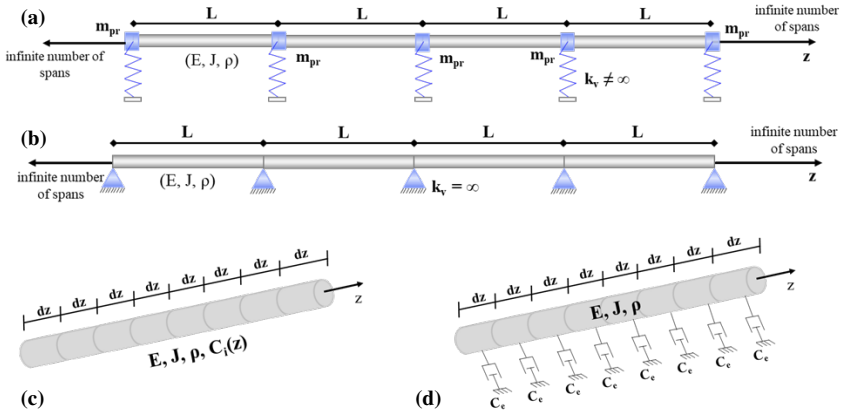

Figure 5.2: (a) PPR_f: Periodic damped pipeline coupled with the flexible supports and the masses m_{pr} of a pipe rack; (b) PPR_r: periodic damped pipeline on rigid supports; (c) internal or structural damping model for a continuous beam and (d) external viscous damping model.

The supports of the pipelines depend on the flexural stiffness k_v of the pipe rack's columns. In Fig. 5.2 (a), flexible springs support the periodic pipeline, i.e., non-negligible displacements of the columns. Fig. 5.2 (b), instead, depicts the model of a pipeline supported by rigid supports. Hereinafter, the models in Fig. 2 (a) and (b) are called $\mathrm{PPR_f}$ and $\mathrm{PPR_r}$, respectively. The damping models that we propose are linear and have different sources, such as internal material damping, see Fig. 5.2 (c), and external damping, see Fig. 5.2 (d). Since the length $dz \to 0$, the damping is continuously distributed along the pipe. Therefore, internal and external damping forces can be represented by two different equations for the Euler-Bernoulli beam.

For the $\mathrm{PPR_f}$ and the internal damping model the Euler-Bernoulli equation reads:

$$\frac{\partial^2}{\partial \mathrm{z}^2}\left[\mathrm{EJ}\frac{\partial^2 w(\mathrm{z,t})}{\partial \mathrm{z}^2}\right] + \frac{\partial^2}{\partial \mathrm{z}^2}\left[\mathrm{C}_i\frac{\partial^2 \frac{\partial w(\mathrm{z,t})}{\partial t}}{\partial \mathrm{z}^2}\right] + \rho A\frac{\partial^2 w(\mathrm{z,t})}{\partial \mathrm{t}^2} = 0, \quad (5.1)$$

where ρ, E, A and J are, respectively, the material density, the Young modulus, the area and the inertia of the beam cross section. The term

w(z,t) is the beam transversal displacement. C_i is the internal damping coefficient. Instead, for an externally damped $\mathrm{PPR_f}$, the Euler-Bernoulli equation reads:

$$\frac{\partial^2}{\partial z^2}\left[\mathrm{EJ}\frac{\partial^2 w(z,t)}{\partial z^2}\right] + \mathrm{C}_e\frac{\partial w(z,t)}{\partial t} + \rho A\frac{\partial^2 w(z,t)}{\partial t^2} = 0, \tag{5.2}$$

where $\mathrm{C_e}$ is the external damping coefficient. In Eqs. (5.1) and (5.2), the damping coefficients read:

$$\mathrm{C}_i = \frac{2\zeta_i \mathrm{EJ}}{\omega}, \tag{5.3}$$

$$\mathrm{C}_e = 2\zeta_e \rho A\omega, \tag{5.4}$$

where $\zeta_{i/e}$ is the modal damping ratio, *i/e* specifies internal or external damping, and ω defines the modal frequency. Note that the two coefficients $C_{i/e}$ have different physical meanings and are dimensionally different. C_i comes from the assumption that structural internal damping does not entail plastic deformations in the cross section of the pipe [141]. In this regard, Kimball et al. [142] showed that, for metals subjected to cyclic stress, internal friction entails strains that remain below the elastic limit. C_e in (5.4), instead, represents the common proportionality constant of a viscous damping model.

The mass and the stiffness of the pipe are constant along its length. Since the systems are periodic, we consider (5.1) and (5.2) and apply the Floquet-Bloch theorem to the j^{th} support, thus obtain:

$$\psi_{\mathrm{i/e}}\cosh^2(\mu_{\mathrm{i/e}}) + \chi_{\mathrm{i/e}}\cosh(\mu_{\mathrm{i/e}}) + \eta_{\mathrm{i/e}} = 0, \tag{5.5}$$

where $\mu_{i/e} = i\kappa L$ is the propagation constant, κ is the wavenumber and L is the distance between the supports. Eq. (5.5) is the dispersion relation wavenumber – frequency of a $\mathrm{PPR_f}$. Indeed, the terms $\psi_{i/e}$, $\chi_{i/e}$ and $\eta_{i/e}$ are functions of $\Omega_{\mathrm{i/e}}$ which reads:

$$\Omega_i = \frac{\rho A\omega^2}{\mathrm{EJ} + i\omega\,\mathrm{C}_i}, \tag{5.6}$$

$$\Omega_e = \frac{\rho A\omega^2 + i\omega\,\mathrm{C}_e}{\mathrm{EJ}}, \tag{5.7}$$

where ω defines the circular frequency. Full derivation of Eq. (5.5) is provided in Appendix C.1.

About the $\mathrm{PPR_r}$, a dispersion relation between μ and ω is available in literature [42], and it reads,

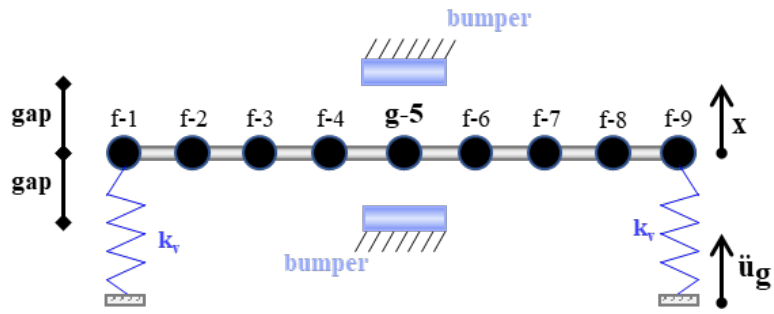

Figure 5.3: Single span (SS) discretized into 9 nodes that vibrate vertically and rotate; f indicates the nodes that do not experience the impact, whereas g-5 has a two-sided displacement constraint.

$$\cosh(\mu_{i/e}) = \cosh(i\kappa L) = -\frac{\cot(\Omega_{i/e}L) \ - \coth(\Omega_{i/e}\mathrm{L})}{\mathrm{csch}(\Omega_{i/e}L) - \csc(\Omega_{i/e}\mathrm{L})}. \tag{5.8}$$

Two-dimensional FEMs of the $\mathrm{PPR_f}$ and $\mathrm{PPR_r}$ are modeled via Ansys APDL 19.0 with Euler-Bernoulli beam elements. A time-harmonic rotation $\phi_{i/p}\ e^{i2\pi ft}$ is imposed as input at the left-end of the pipe, and the steady state response $\phi_{o/p}\ (f)$ is read as the output rotation at the right-end. The system response in the frequency domain is evaluated as follows,

$$FRF = 20\log_{10}\left|\frac{\phi_{\mathrm{o/p}}(\mathrm{f})}{\phi_{\mathrm{i/p}}(\mathrm{f})}\right|, \tag{5.9}$$

where *FRF* is the frequency response function expressed in dB. To foster the dynamics of a finite periodic system, the FEM consists of a 40 spans beam.

Optimization of the stochastic dynamic performance of the impact device

To analyse the performance of the vibro-impact system (VIS), nonlinear transient analyses were carried out on the equations of motion of a single unit cell of the $\mathrm{PPR_f}$, i.e., a SS beam supported by flexible springs. The aforementioned FEM was adopted to obtain the consistent mass matrix **M**, the symmetric stiffness matrix **K** whereas the damping matrix **C** was computed with the proportional Rayleigh damping model. The discretized model of the SS equipped with a VIS is depicted in Fig. 5.3.

The interface of the SS has a two-sided displacement constraint, such that the node **g-5** impacts two rigid bumpers. In this case, we directly

model the VIS and let the system of equations of motion to remain fully linear. The COR is defined according to Newton's law [147]:

$$\mathrm{COR} \;=\; -\,\frac{\mathrm{v_r}^{+}}{\mathrm{v_r}^{-}}, \tag{5.10}$$

where v_r is the relative velocity of two colliding bodies, and + and – mean post-impact and pre-impact, respectively. Since the bumpers are fixed to the ground, relative velocities coincide with absolute velocities. Note that (5.10) does not need further nonlinearities to be included. However, to take into account the typical limitations of the aforementioned instantaneous model [147, 153, 154, 155], very small time steps of the order of 10^{-5} have been used; thus, the simulations showed a limited dependence from time steps[155].

The equations of motion read:

$$\mathbf{M}\ddot{\mathbf{x}} + \mathbf{C}\dot{\mathbf{x}} + \mathbf{K}\mathbf{x} = -\mathbf{M}\mathbf{r}\mathbf{u}_{\mathbf{g}}, \tag{5.11}$$

where **M**, **C** and **K** are respectively the mass, damping and stiffness matrices, **r** is the influence vector and u_g is the ground displacement; the dot represents the derivative wrt the time. When impact occurs, the g node is subjected to the impact forces, and the f nodes vibrate according to inertial and restoring forces. The equations of motion now read:

$$\begin{bmatrix}\mathbf{M}_{\mathrm{ff}} & \mathbf{M}_{\mathrm{fg}}\\ \mathbf{M}_{\mathrm{gf}} & \mathbf{M}_{\mathrm{gg}}\end{bmatrix}\begin{Bmatrix}\ddot{\mathbf{x}}_{\mathrm{f}}\\ \ddot{\mathbf{x}}_{\mathrm{g}}\end{Bmatrix} + \begin{bmatrix}\mathbf{C}_{\mathrm{ff}} & \mathbf{C}_{\mathrm{fg}}\\ \mathbf{C}_{\mathrm{gf}} & \mathbf{C}_{\mathrm{gg}}\end{bmatrix}\begin{Bmatrix}\dot{\mathbf{x}}_{\mathrm{f}}\\ \dot{\mathbf{x}}_{\mathrm{g}}\end{Bmatrix} + \begin{bmatrix}\mathbf{K}_{\mathrm{ff}} & \mathbf{K}_{\mathrm{fg}}\\ \mathbf{K}_{\mathrm{gf}} & \mathbf{K}_{\mathrm{gg}}\end{bmatrix}\begin{Bmatrix}\mathbf{x}_{\mathrm{f}}\\ \mathbf{x}_{\mathrm{g}}\end{Bmatrix} = -\begin{bmatrix}\mathbf{M}_{\mathrm{ff}} & \mathbf{M}_{\mathrm{fg}}\\ \mathbf{M}_{\mathrm{gf}} & \mathbf{M}_{\mathrm{gg}}\end{bmatrix}\begin{Bmatrix}\mathrm{r_f}\\ \mathrm{r_g}\end{Bmatrix}\ddot{\mathrm{u}}_{\mathrm{g}} + \begin{Bmatrix}0\\ \mathrm{R_g}\end{Bmatrix}, \tag{5.12}$$

where $\mathbf{R}_{\mathrm{g}}$ is the impact force vector. We divide Eq. (5.12) in two different equations, one for the non-impacting nodes f and one for the impacting node g. Since the impact force is unknown, we consider the first equation of the system in Eq. (5.12), as

$$\mathbf{M}_{\mathrm{ff}}\ddot{\mathbf{x}}_{\mathrm{f}} + \mathbf{C}_{\mathrm{ff}}\dot{\mathbf{x}}_{\mathrm{f}} + \mathbf{K}_{\mathrm{ff}}\mathbf{x}_{\mathrm{f}} = -\left(\begin{bmatrix}\mathbf{M}_{\mathrm{ff}} & \mathbf{M}_{\mathrm{fg}}\end{bmatrix}\begin{Bmatrix}\mathrm{r_f}\\ \mathrm{r_g}\end{Bmatrix}\ddot{\mathrm{u}}_{\mathrm{g}} + \mathbf{M}_{\mathrm{fg}}\ddot{\mathbf{x}}_{\mathrm{g}} + \mathrm{C}_{\mathrm{fg}}\dot{\mathbf{x}}_{\mathrm{g}} + \mathbf{K}_{\mathrm{fg}}\mathbf{x}_{\mathrm{g}}\right). \tag{5.13}$$

To obtain the structural response at the i^{th} step of the algorithm, Eq. (5.12) is employed when the pipe and the bumper are not in contact. Conversely, if the contact occurs, (5.13) is used. A flowchart that describes the algorithm implemented in MATLAB for the nonlinear impact model is shown in Fig. 5.4.

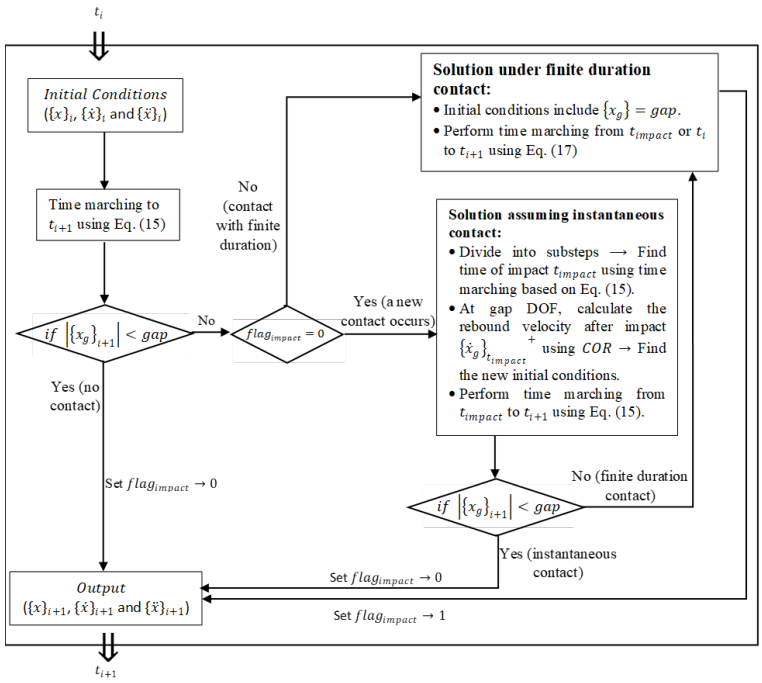

Figure 5.4: Flow chart for the implementation of the impact in the transient analyses in MATLAB

At a certain instant t_d the energy dissipated by linear viscous damping is computed as follows:

$$\mathrm{E_{dam}(t_d)} = \sum_{\mathrm{t=0}}^{\mathrm{t=t_d}} \{\mathrm{dx}\}_\mathrm{t}{}^\mathrm{T}.\mathrm{C}.\{\dot{\mathrm{x}}\}_\mathrm{t}, \tag{5.14}$$

whilst the energy dissipated by the impacts reads,

$$\mathrm{E_{imp}(t_d)} = \frac{1}{2} \sum_{\mathrm{i=0}}^{\mathrm{n_d}} (\{\dot{\mathrm{x}}\}^{+\,\mathrm{T}}\mathrm{M}\{\dot{\mathrm{x}}\}^{+} - \{\dot{\mathrm{x}}\}^{-\,\mathrm{T}}\mathrm{M}\{\dot{\mathrm{x}}\}^{-}), \tag{5.15}$$

where n_d is the number of impacts occurred up to t_d, and $\{\dot{x}\}^-$ and $\{\dot{x}\}^+$ represent the velocity vector before and after impact, respectively. Once the seismic event is extinguished, free decay oscillation occurs in the structure up to a certain time t_r at which the rest condition is fully restored and the number of impacts is n_{im}. The total input seismic energy reads:

$$\mathrm{E_{tot}(t_r)} = \mathrm{E_{dam}(t_r)} + \mathrm{E_{imp}(t_r)}. \tag{5.16}$$

Therefore, at time instant t_r, all the input seismic energy has been dissipated by means of viscous damping and impacts. We seek for the

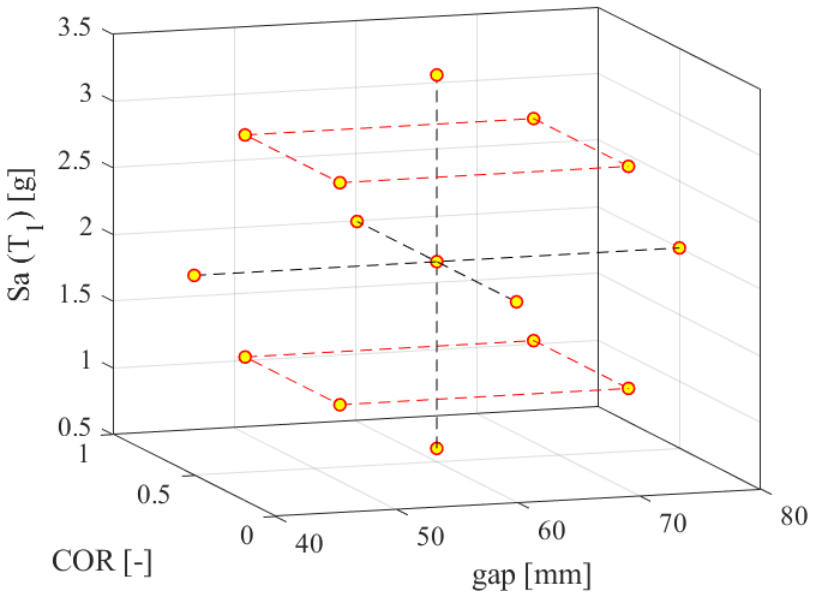

Figure 5.5: Central composite design (CCD) points for three factors: gap, COR, and $Sa(T_1)$.

design parameters *COR* and *gap* that optimize the seismic performance of the impact system with a multi-objective optimization problem based on two objective functions defined as follows,

$$O_1(\mathrm{t_r}) = \frac{\mathrm{E_{imp}}}{\mathrm{E_{tot}}}, \tag{5.17}$$

$$\mathrm{O_2(t_r) = n_{im}}, \tag{5.18}$$

where n_{im} is the number of impacts, E_{imp} and E_{tot} are defined by (5.15) and (5.16), respectively. The purpose of installing bumpers next to the pipe is to dissipate the largest amount of energy through impacts while limiting the number of impacts, to prevent damage to the pipe. Therefore, the objective function O_1 must be maximized, or equivalently -O_1 must be minimized, while O_2 is to be minimized. To reduce the number of transient analyses, we combine CCD and Kriging modelling with the explanatory variables *COR*, *gap*, and *Sa* (T_1), and response variables O_1 and O_2. The 15 yellow points in Fig. 5.5 indicate the computer-experimental data set - sampling points - defined by the CCD. The ranges of values of the explanatory variables are shown in Tab. 5.1.

Note that the IM, i.e., the spectral acceleration *Sa*(T_1) at the first natural period T_1 of the system, is included in the CCD. The system is non-

CCD variable	Lower Limit	Upper Limit
COR [-]	0.01	0.99
gap [mm]	40	80
$Sa(T_1)$ [g]	0.6	3.4

Table 5.1: Bounds of the CCD variables.

linear and sometimes chaotic, see Appendix C, therefore a certain variability of the system response wrt the input is expected. As indicated in Tab. 5.1, $Sa\ (T_1)$ is bounded by the mean minus/plus the standard deviation of the selected records. Then, to evaluate O_1 and O_2 for the 15 points selected within the CCD, seismic transient analyses are carried out. Each ground motion, see Tab. 5.2, is scaled at the relevant value of $Sa(T_1)$ and thus, O_1 and O_2 are calculated as the mean of the values obtained by employing all the seismic records described hereinafter. After running all the 15x12 analyses needed for CCD, a Gaussian polynomial regression between the 15 mean values by means of the Kriging metamodeling provided by UqLab [161] has been performed. It has been assumed that the model output is a realization of a Gaussian process defined as the joint distribution of the prediction and the true model response [161].

Then, the Pareto front is used to provide the optimal values of the multi-objective optimization problem by seeking the nondominated solutions among the O_1 and O_2 quantities of (5.17) and (5.18) evaluated through the Kriging metamodel. To each nondominated solution of the Pareto front will correspond an optimal triplet ($Sa(T_1)$, gap, COR). Therefore, the optimal values of gap and COR are connected to a certain value of $Sa(T_1)$; nonetheless $Sa(T_1)$ is not a true design parameter since it characterizes a (seismic) stochastic process.

5.2.2 Seismic input, fragility assessment, and optimal design parameters selection

For evaluating the performance of the SS depicted in Fig. 5.3, a set of twelve natural records with a 2% probability of exceedance in 50 years, are employed; that is, relevant to safe shutdown events (SSE). The selection of the natural seismic records follows the principle sketched in Fig. 5.6:

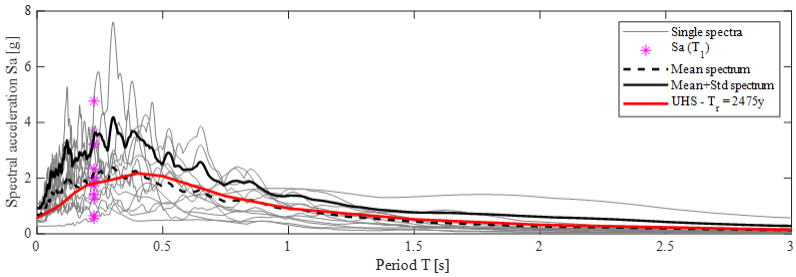

Figure 5.6: Response spectrum, mean spectrum and mean + standard deviation spectrum matching the UHS; in gray, each individual spectrum of Tab. 5.2.

Both the mean spectrum and the mean spectrum plus one standard deviation of the selected accelerograms match with the uniform hazard spectrum (UHS) of a specific site, Priolo Gargallo, Sicily in Italy, in a least-square sense. More precisely, let us consider $\boldsymbol{s_0}$ the target spectrum value vector, that is, the UHS; and evaluate $\mathbf{S}$ as the spectra matrix of the n_a accelerograms. One can define a vector of n_a selection coefficients, α, where each element can only take a binary value of 1 or 0, and the sum of the elements is equal to n_s, i.e., the number of accelerograms to be selected. Thus, the vector α that satisfies:

$$\min\left(\left\|\frac{\mathbf{S}_\alpha}{n_s} - \mathbf{s_0}\right\|^2\right). \tag{5.19}$$

is sought. The selection is performed with all possible combinations of the n_s accelerograms among a set of n_a records. This operation allows to preserve full hazard consistency and minimize the record-to-record variability yet considering the dispersion of the records about the mean spectrum. Tab. 5.2 reports the set of accelerograms and their main characteristics.

Event	**Country**	**R [km]**	**M**
1. Victoria Mexico	Mexico	13.8	6.33
2. Loma Prieta	USA	3.85	6.93
3. Northridge-01*	USA	20.11	6.69
4. Montenegro*	Montenegro	25.00	6.90
5. Erzincan	Turkey	13.00	6.60
6. South Iceland*	Island	7.00	6.50
7. L'Aquila Mainshock*	Italy	4.87	6.30
8. Loma Prieta	USA	11.03	6.93
9. Landers*	USA	11.03	7.28

Event	Country	R [km]	M
10. South Iceland*	Island	11.00	6.40
11. L'Aquila Mainshock*	Italy	4.63	6.30
12. L'Aquila Mainshock*	Italy	4.39	6.30

Table 5.2: Main characteristics of the selected records; R is the distance from the epicenter, and M is the magnitude of the relevant seismic event.

Note that in 5.2, the * indicates those records that are employed for performing the IDA. The number of impacts, indeed, is related to the maximum velocity exhibited by the system during the transient analysis, and to observe a sufficient number of impacts, the duration of the strong motion must exceed about 40 seconds.

Finally, we perform the fragility assessment of the SS. Along this line, the fragility function F_{DM} *(IM)* is defined as the probability that the node **g-5** of Fig. 5.3 reaches or exceeds some damage measure (DM) for a given ground motion with $IM = im$. In particular, the DM is connected to the number of impacts $n_i m$, i.e., the engineering demand parameters (EDP), that exceeds a certain threshold. Typically, $F_{DM}(IM)$ is assumed to follow a lognormal distribution, and hence reads,

$$\begin{aligned} \mathrm{F_{DM}(IM)} \;&\equiv\; \mathrm{P[EDP > edp \,|\, IM = im]}, \\ \mathrm{F_{DM}(IM)} &= \Phi\left(\frac{\ln(\mathrm{im/X_m})}{\beta}\right), \end{aligned} \tag{5.20}$$

where Φ is the Gaussian cumulative distribution with a median X_m and a logarithmic standard deviation β, calculated as:

$$\mathrm{X_m} = \exp\left(\frac{1}{\mathrm{M}} \sum_{\mathrm{i}}^{\mathrm{M}} \ln(\mathrm{IM_i})\right), \tag{5.21}$$

$$\beta = \left(\frac{1}{\mathrm{M\text{-}1}} \sum_{\mathrm{i}}^{\mathrm{M}} \left[\ln(\mathrm{IM_i/X_m})\right]^2\right)^{1/2}, \tag{5.22}$$

where M is the number of ground motions considered, and IM_i is the IM value associated with onset of DM for the i^{th} ground motion. The values of IM_i are the results of the IDA performed on the SS. Commonly, the IDA involves scaling each ground motion in a suite until it causes the exceedance of some DM [171]. However, for the purpose of generality, FDM (IM) in Eq. (5.20) is calculated for all the feasible n_{im} = *EDP* corresponding to the Pareto front. In fact, the Pareto front highlights the optimal design parameters *gap* and *COR*. Therefore, each

optimal value of the Pareto front corresponds to a fragility surface (F_{DM} *(IM)*, *IM*, *EDP*). The corresponding volume V_j under the j$^{\text{th}}$ surface is computed as follows

$$\mathrm{V_j} = \int_{IM} \int_{EDP} F_{DM}(\mathrm{IM})\, \mathrm{dIM}\, \mathrm{dEDP}, \tag{5.23}$$

where *j* indicates the j^{th} optimal solution of the Pareto front. According to the law of total probability, (5.23) is proportional to the total probability of exceedance of all the edps. Then, one should perform the fragility assessment for all the $j = \{1, \ldots, n\}$ Pareto front solutions and select the optimal couple *gap* - *COR* that minimizes (5.23). In this work, an application of this procedure is shown for three optimal couples.

5.3 Results

5.3.1 Dispersion curves of the PPRs and enhancement of the attenuation rate

The pipe cross section measures an outer and inner diameter of 0.*2731* m and 0.*2639* m, respectively, while the inertia *J* of the cross section is 3.4977e-5 m^4. The span length *L* is *12* m, and the modulus of elasticity *E* and the mass density ρ are respectively *200* GPa and *7800* kg/m^3. The stiffness k_v of the pipe rack's pillars is *17.9* MN/m and the mass m_{pr} of the repetitive unit of the coupled system PPR is equal to *22880* kg. Consequently, the first natural frequency of the PPR$_\mathrm{f}$ reads $\omega_{pr,1} = (k_v/m_{pr})^{0.5} = 4.45$ Hz.

When the pillars' stiffness is considerably higher than the pipe's flexural stiffness, the pillars act as rigid supports wrt the flexural behavior of the pipe. Thus, the PPR$_\mathrm{r}$ is modeled as a beam supported by simple supports. The dispersion diagrams of the internally damped PPR$_\mathrm{r}$ are calculated via Eq. (5.8) and are depicted in Fig. 5.7.

Fig. 5.7 shows the dispersion diagrams $(\mu - f)$ for seven values of material damping ζ_i of Eq. (5.3). The yellow bands in Fig. 5.7 (a) and (b) highlight four bandgaps in the following frequency ranges: *[0 - 5.25]* Hz, *[11.94 - 21.01]* Hz, *[32.79 - 47.27]* Hz and *[64.30 - 84.03]* Hz. The dispersion diagrams of Fig. 5.7 reveal common properties of linear periodic systems. The blue curve represents the undamped pipe and clearly defines the bandgaps in the regions where $\Re(\mu) \neq 0$ and, consequently, $\Im(\mu) = 0$ or $\Im(\mu) = \pi$, unveiling the existence of pure evanescent waves. Instead, for damped pipes with nonzero values of ζ, $\Re(\mu) \neq 0$ in

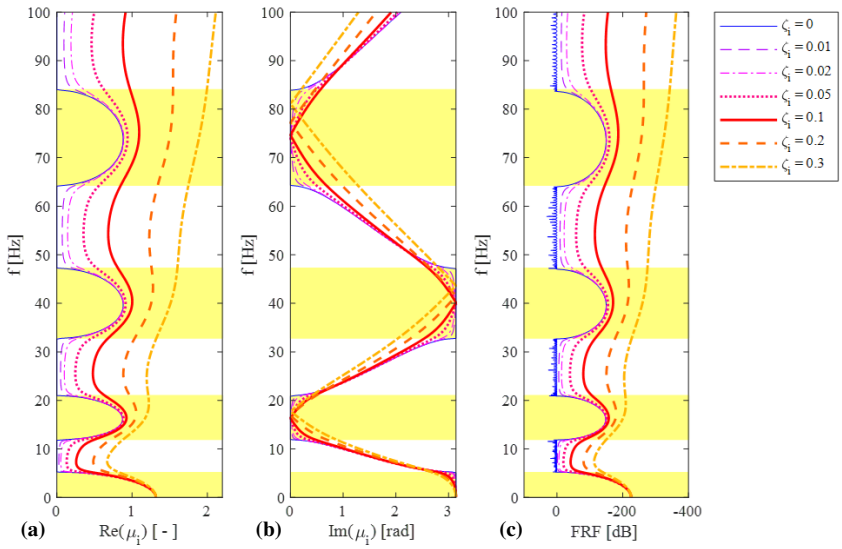

Figure 5.7: Dispersion curves for an internally damped PPR$_r$ as a) function of real part of μ_i, b) function of the imaginary part of μ_i; c) numerical FRF of the finite periodic (40 spans) FEM. The bandgaps are indicated in yellow.

the overall frequency domain, since attenuating oscillatory waves can always be observed for all frequencies. However, the damping is included in the main structure, and clearly enlarges the attenuation rate $\Re(\mu)$. This effect is more evident as the frequency range increases. Fig. 5.7 (c) shows the FRF of Eq. (5.9), evaluated with the FEM. A good agreement is observed between Fig. 5.7 (c) and the dispersion curves of Fig. 5.7 (a) and (b), in terms of passbands, bandgaps and attenuation rates.

Let us now consider the PPR$_\mathrm{f}$, see Fig. 5.2 (a). The pipe rack is modeled by a spring-mass oscillator that matches the first lateral mode of the rack. Iqbal et al. [43] demonstrated the effectiveness of such approximation. The relevant dispersion curves are calculated via Eq. (5.5) and plotted in Fig. 5.8.

Fig. 5.8 (a) and (b) show the dispersion relations of the PPR$_\mathrm{f}$, where a local resonance is observed around the first natural frequency of the pipe rack $\omega_{pr,1} = 4.45$ Hz. The first bandgap, that initially ranged from 0 Hz to *5.25* Hz, is now divided into two different bandgaps. Generally, bandgaps can be tuned with local resonances, whereas the Bragg scattering induces bandgaps that are constrained by the periodic system dimensions. Nevertheless, in this paper the PPR$_\mathrm{f}$'s first natural frequency belongs to the first bandgap frequency range, and therefore no additional bandgaps appear. On the contrary, Fig. 5.8 (a) and (b) depict a zoom on a narrow passband that opened due to the pipe rack's resonance. Fi-

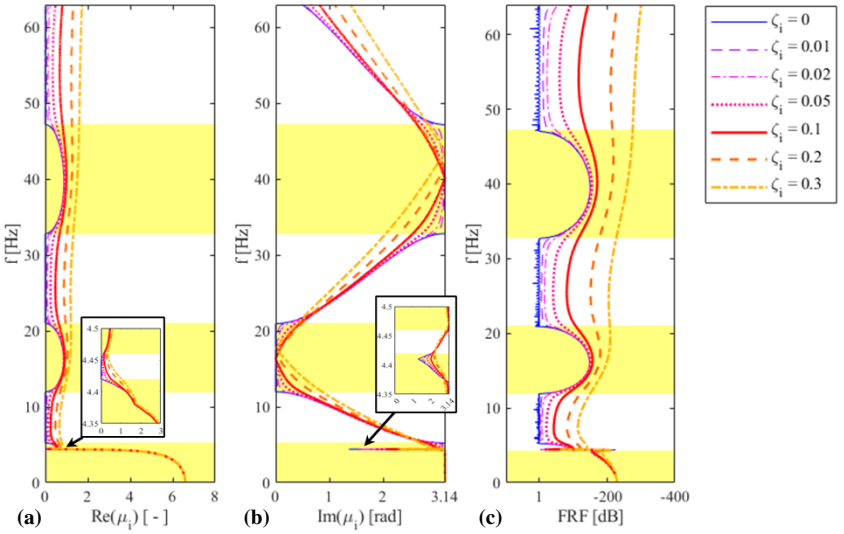

Figure 5.8: Dispersion curves for an internally damped PPR$_f$: a) real part of μ_i, b) imaginary part of μ_i; c) the numerical FRF.

nally, one can notice a good agreement between the numerical FRF of Fig. 5.8 (c) and the analytical dispersion diagrams of Fig. 5.8 (a) and (b). Again, the damping induces an attenuation rate that increases with the frequency.

The combination of Eq. (5.7) with (5.5) and (5.8) allows for plotting the dispersion diagrams and the bandgaps relevant to the external damping case. Also in that situation, favourable bandgap zones can be obtained; for brevity, they are not shown or commented on.

5.3.2 Optimization results

As anticipated in a previous subsection, the Pareto front depicted in Fig. 5.9 pinpoints the nondominated solutions among all the possible realizations evaluated with the Kriging model.

The surrogate Kriging metamodel generates O_1 and O_2 as 3D-arrays for the parameters *gap*, *COR* and *Sa(T_1)*. Therefore, the Pareto front highlights the optimal triplets (*Sa(T_1), gap, COR*), and the optimal values of *gap* and *COR* correspond to a certain *optimal* value of *Sa(T_1)*.

Nonetheless, *Sa(T_1)* is characterized by randomness and influences the optimal solutions. For clarity, the three surfaces that depict the values of O_1 wrt three optimal *Sa(T_1)*, equal to 0.6 g, 1.3 g and 2 g, are depicted in Fig. 5.10.

Note that the objective function O_1 defined in (5.17), must be max-

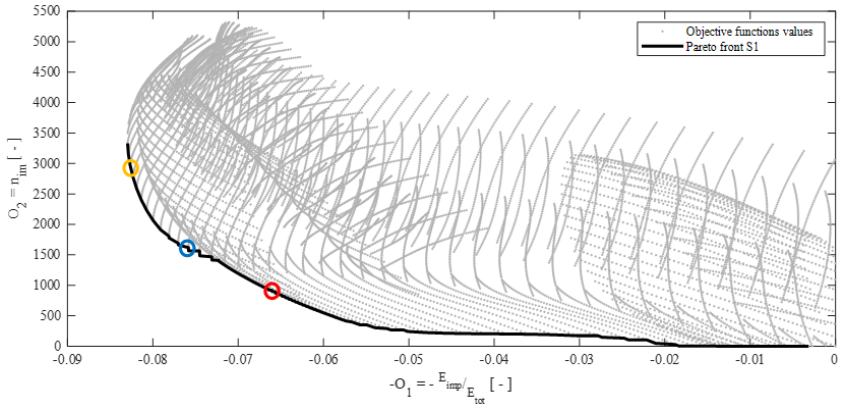

Figure 5.9: Plot of all the realizations of the Kriging metamodel and the Pareto front; the circles indicate the three optimal solutions investigated in the Subsection 5.3.3.

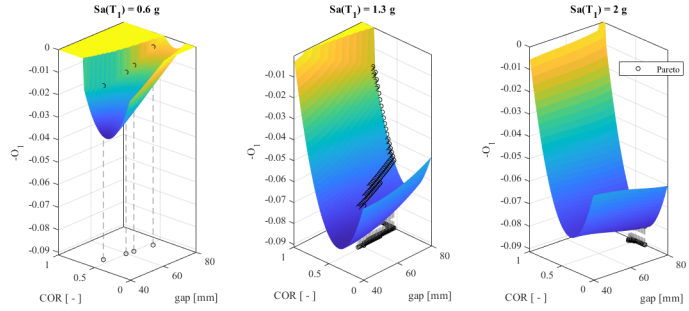

Figure 5.10: O_1 surfaces for (a) the optimal $Sa(T1)$ equal to 0.6 g, (b) equal to 1.3 g, and (c) 2 g.

imize. Nonetheless, we plot $-O_1$ in Fig. 5.10 and seek for its minimum values. The surfaces O_2 of (5.18) refer to the optimal $Sa(T_1)$ equal to 0.6 g, 1.3 g, and 2 g in Fig. 5.11. The black circles in both Fig. 5.10 and Fig. 5.11 represent the Pareto front of Fig. 5.9.

To underline the sensitivity of the optimization problem to the seismic input $Sa(T_1)$, Fig. 5.12 shows the Pareto fronts corresponding to several levels of $Sa(T_1)$.

It is clear that the optimal solutions differ significantly as the severity level of the seismic input varies. For clarity, Fig. 5.13 depicts all the Pareto fronts of Fig. 5.12 along with the relevant surfaces O_1 and O_2.

One can clearly note that the optimization is sensitive to the seismic input $Sa(T_1)$; therefore, the inclusion of the IM in the CCD is justified. A few more general considerations arise from the optimization results.

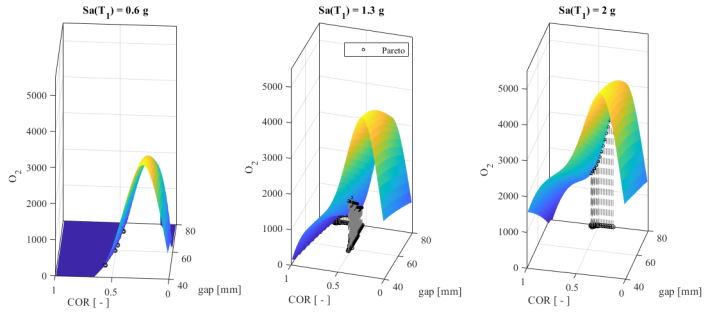

Figure 5.11: O_2 surfaces for (a) the optimal $Sa(T_1)$ equal to 0.6g, (b) 1.3g, and (c) 2g.

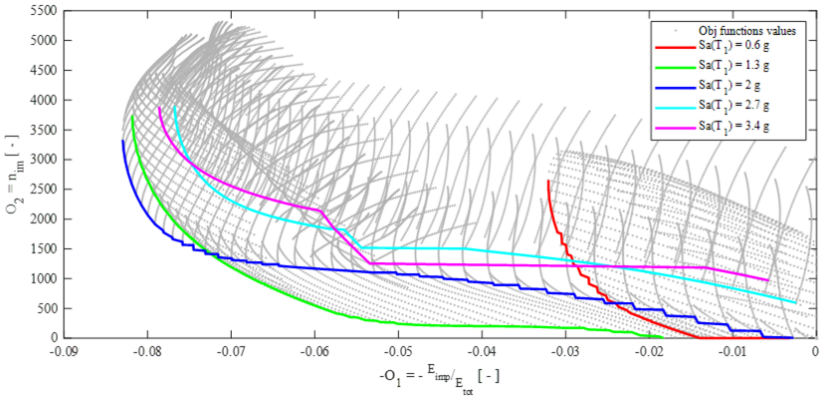

Figure 5.12: Pareto fronts obtained for certain $Sa(T_1)$ levels.

Both the objective functions O_1 and O_2 depend more on the *COR* than on the *gap*. In particular, optimal values of *COR* are found in the whole range *0-1*, whereas large *gap* values are optimal for strong earthquakes, say *Sa(T1)* equal to *2* g, *2.7* g, and *3.4* g. For lower values of *Sa(T1)*, the optimal *gap*s cover the whole range *40-80* mm.

5.3.3 Fragility assessment and selection of the optimal solution

To perform the fragility assessment, three optimal solutions among those of the Pareto front in Fig. 5.9 are randomly taken; and the IDA are calculated for the eight ground motions indicated with the * in Tab. 5.2. Fig. 5.14 reports the results of the IDA and the relevant 2D fragility functions.

The impact phenomenon generates chaotic motion, as described in Appendix C.2; hence the IDAs result in responses that are not unique

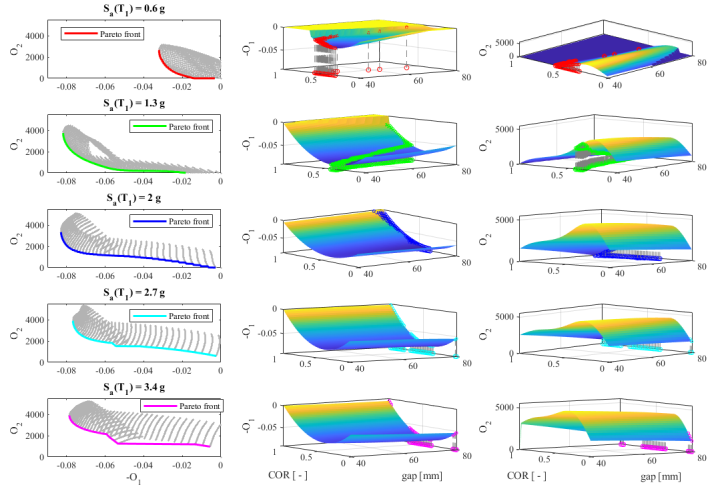

Figure 5.13: On the left column, each single Pareto front of Fig. 5.12; on the middle and the right column, the -O_1 and O_2 surfaces, respectively.

for a certain $EDP = n_{im}$. Vamvatsikos et al. [171] described the occurrence of multiple capacity points, and recommended to handle this ambiguity by an ad hoc, specified procedure, i.e., by conservatively defining the limit state point as the lowest IM. However, we preferred to filter the numerical data of the IDA, see the circles in Fig. 5.14, with a moving average technique that resulted in the solid curves of Fig. 5.14. Indeed, the IDA curves appear rather noisy because of the nonlinear and sometimes chaotic behavior of the vibro-impact system.

Then, the fragility surfaces are calculated by Eq. (5.15) and are plotted in Fig. 5.14 and Fig. 5.15.

We can compute the volumes underneath the surfaces of Fig. 5.15 (a), (b), and (c) with (5.23). The lower the surface, the lower the probability of exceedance of the edp, namely the number of impacts n_{im}. The volumes relevant to Fig. 5.15 (a), (b), and (c) read: $V_1 = 6698$ g, $V_2 = 7069$ g, and $V_3 = 7270$ g. Therefore, the Optimal solution #1 is the one that minimizes the volume under the fragility surface.

Finally, and for the sake of completeness, the reader can appreciate the speed of the algorithm sketched in Fig. 5.4 by using Optimal solution #1. In this respect, Tab. 5.3 reports the CPU time required to simulate the response of the optimal VIS to the records listed in Tab. 5.2 using MATLAB. The simulations run on a processor with a clock speed of 3.00 GHz and 4 cores.

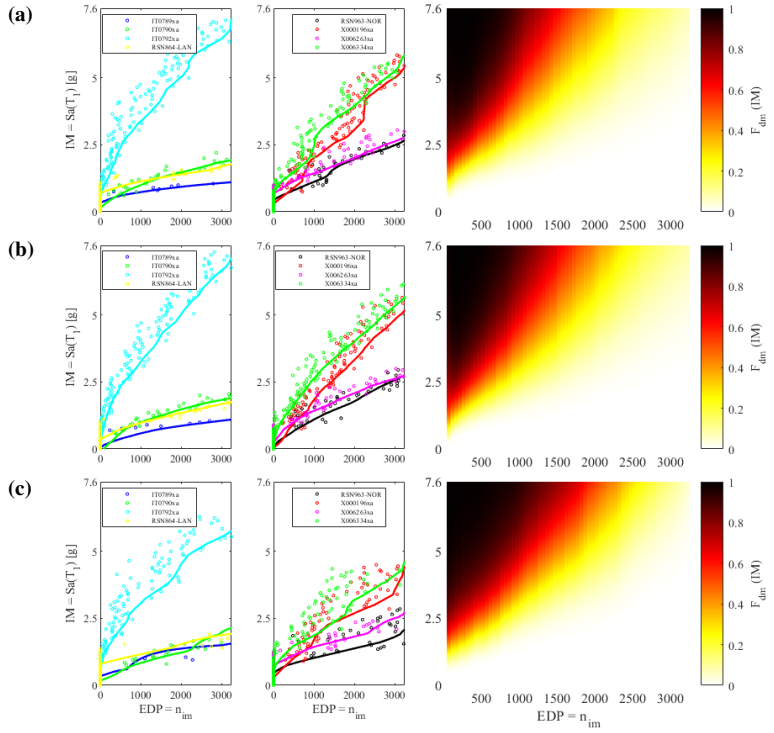

Figure 5.14: IDA curves on the left side and 2D color plot of the fragility function on the right side for (a) the first optimal point with gap = 64 mm, COR = 0.49; (b) the second optimal point with gap = 58 mm, COR = 0.52; and (c) the third optimal point with gap = 80 mm, COR = 0.39. These optimal points are indicated by the circles in Fig. 5.9.

One can observe that the CPU time employed to solve the system of equations (5.11) is effective in relation to the event duration.

5.3.4 Discussion and outlook

In this chapter, the enhanced attenuation properties of two periodic damped pipelines coupled with pipe racks (PPRs) have been shown; and the relevant results have been confirmed by the FE software Ansys on a 40-spans PPR. Two damping models were proposed in view of vibration mitigation, i.e., internal material damping, and external viscous damping. A local resonance was observed around the first natural frequency of the PPR $\omega_{pr,1} = 4.45$ Hz. The damping clearly enlarges the attenuation rate $\Re(\mu)$, and this effect is more evident as the frequency range increases.

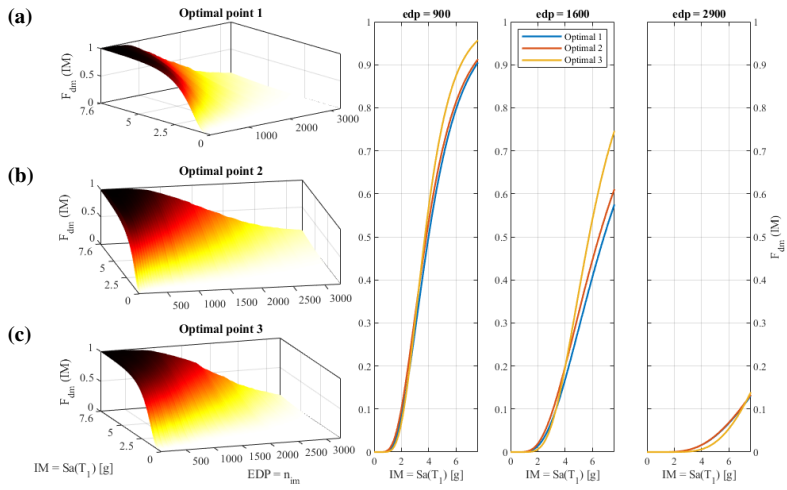

Figure 5.15: Fragility surfaces for (a) Optimal solution #1, (b) Optimal solution #2, (c) Optimal solution #3, and relevant fragility curves for (d) $n_im = 900$, (e) $n_im = 1600$, (f) $n_im = 2900$; these values of $n_im = 900$ were taken from the values of O_2 in Fig. 5.9.

Event	**1**	**2**	**3**	**4**	**5**	**6**
Event duration [s]	100	100	100	24.5	25	25
CPU time [s]	32.1	36.0	36.8	12.1	9.8	10.1
Event	**7**	**8**	**9**	**10**	**11**	**12**
Event duration [s]	44	40	48.2	72.5	55	21.3
CPU time [s]	16.8	16.0	18.8	26.6	19.2	9.2

Table 5.3: CPU time requested for solving the transient analyses for each seismic record of Tab. 5.2.

As a result of the analyses, we have found a good agreement between the frequency response function (FRF) of the FEMs and the analytical band structures.

Then, a generic single span (SS) of the PPR equipped with a vibro-impact system (VIS) was considered; and due to the nonlinearities, a design optimization procedure was conceived and carried out. The procedure aims to maximize the dissipation energy and to minimize the number of impacts. Both objective functions resulted to be more sensitive to the COR than to the gap; the response surface was generated by the Kriging metamodel with a Gaussian 2nd order-polynomial regression. It was found that the metamodels were endowed with sharp curvatures wrt to COR. Optimal values of COR were found in the whole range 0-1;

large gap values appear to be optimal for strong earthquakes, say $Sa(T_1)$ equal to 2 g, 2.7 g, and 3.4 g, whereas optimal gaps are found in the whole range 40-80 mm for lower values of $Sa(T_1)$. Moreover, we have found that the optimal solution with $gap = 64$mm and $COR = 0.49$ is the one that minimizes the probability of exceeding the damage states (DM) connected to the engineering demand parameter (EDP), that is, the number of impacts. The incremental dynamic analysis (IDA) resulted in curves that are not unique for a certain EDP, i.e., noisy, mainly due to the chaotic behavior of the VIS. In addition, the IDA curves displayed significant record-to-record variability: for example, in Fig. 5.14 (a), the EDP $n_{im} = 3000$ was reached for values of $Sa(T_1)$ equal to about 1 g, 1.6 g, 1.7 g, 2.4 g, 2.5 g, 5 g, 5.3 g and 7 g. This result, however, must be imputed to the frequency content of the records and the nonlinear response of the VIS that exhibits a strong dependency upon frequency and amplitude of excitation, and sometimes chaos. To investigate this last issue, we have excited the SS of Fig. 5.3 with periodic loadings for a restricted range of frequencies in the vicinity of $\omega_{pr,1}$, and have reported the relevant bifurcation diagrams in Appendix C.2. When impact does not occur, the bifurcation diagram shows that the system is linear and periodic. Conversely, the impact activates higher modes of vibrations, and non-periodic solutions that can be found in the bifurcation diagram. Therefore, three of these trajectories have been investigated, and the largest Lyapunov exponents were found to be higher than zero, thus indicating the presence of divergence and chaos.

In conclusion, we have shown how to evaluate the safest design solution for a nonlinear dissipation system despite the (seismic) stochastic nature of the loading. Nevertheless, some challenges remain undisclosed. First, the dispersion curves define the linearly damped system without impact-induced dissipation. Nonlinear waves, in fact, distort as they propagate and change their original shape along the periodic medium; this causes the impossibility to find periodic, harmonic solutions, to define a unique frequency - wavenumber relation. In this vein, numerical transient analyses of a multiple-span pipe rack may reveal periodic features of the impacting repetitive structure. Moreover, in-depth investigation of chaos for systems under (seismic) stochastic excitation may disclose the predictability of some paths for subharmonic resonances, period doublings, grazing bifurcations, etc.

6.0 Conclusions and outlook

6.1 Conclusions

Since the advent of metamaterials in mechanics, they have demonstrated tremendous potential in controlling and mitigating elastic waves. The literature is replete with studies that leverage the resonant properties of metamaterials to confine wave transmission and energy dissipation in non-critical areas of the structure, such as metafoundations, metabarriers, or metasurfaces. In the case of finite lattices, metastructures have been designed to take advantage of strong attenuation zones in the frequency domain, known as bandgaps, which are generated by Bragg scattering or local resonances. However, in recent years, there has been a growing belief that nonlinearities could expand the methods of elastic wave control, making metamaterials even more promising. This is not only in terms of analysis accuracy but also in terms of exploiting typical nonlinear phenomena, such as amplitude-gaps, solitons, multi-resonances, bifurcation, chaos, and so on. Against this backdrop, this thesis develops analytical and numerical analyses of nonlinear metamaterials and metastructures to address two primary challenges: i) identifying and controlling dispersion characteristics in nonlinear periodic structures in free oscillation, and ii) mitigating seismic waves through nonlinear finite lattices.

In relation to i), Chapter 2 presents a dispersion curve identification tool that can be used experimentally and numerically. The method applies to all one-dimensional structures that consist of periodic spatial repetitions of unit cells and is based on applying Floquet-Bloch (FB) conditions to a reference subsystem (RS) modeled as a simple spring-mass system. Latest investigations have proven that this method also works on one-dimensional continuous systems in the linear regime; nevertheless, these findings are not reported in this thesis. The proposed procedure offers several advantages: a) it does not operate on finite lattices, avoiding numerical/experimental issues related to wave reflections, perfectly matched layers, and so on; b) it reduces the identification effort since the procedure relies on a simple experimentally informed RS; c) the identification of the dispersion law includes the imaginary part of wavenumbers; d) the identification procedure captures the dependency of nonlinear dispersion curves on the amplitude of excitation. Regarding this last consideration, Chapter 2 presents a perturbation approach to analyze the frequency response function (FRF) of the weakly nonlinear

metamaterial. It shows that although the application of the FB theorem neglects superharmonics, the dispersion curve still maintains the amplitude dependency of the first harmonic.

Continuing with i), Chapter 3 proposes a new apparatus for switching the propagation of surface acoustic waves (SAWs) using nonlinear tools. The concept is based on the fact that the tunability of SAWs propagating on the edge of an elastic plate can be achieved by compressing external slender beams in the regime of large displacements. The frequency analysis of a doubly clamped beam performed via harmonic perturbation around the postbuckling configuration of the beam is presented. This analysis shows that the amplitude of the vibration response of buckled beams decreases with respect to that of undeformed beams and that the first normal modes disappear from the frequency range of the SAWs. These effects result in the dispersion curve of the SAWs being undisturbed by the vibrations of the buckled beams. In particular, by imposing postbuckling to the beams, it is shown that switching of the SAWs for certain frequency ranges is possible. Chapter 3 presents this concept both analytically and numerically and provides a detailed description of a conceptual mock-up that we have designed and is currently in production.

Regarding point ii), Chapters 4 and 5 investigate the feasibility of using a nonlinear metafoundation and a nonlinear metapipe for protecting special-risk industrial structures, namely a fuel storage tank and a pipeline-pipe rack coupled system (PPR), respectively. The metafoundation is composed of massive vibrating concrete blocks that are coupled to the slabs using fully nonlinear hysteretic devices. To identify the effective properties of the devices in terms of stiffness and equivalent damping, an optimization procedure is carried out by minimizing two dimensionless performance indices based on the variances of the interstorey displacement of the impulsive mass and the relevant absolute acceleration. Regarding the metapipe, we modeled two periodic damped PPRs, and two damping models were proposed, i.e., internal material damping and external viscous damping. Chapter 5 presents a design optimization procedure of a single span (SS) of the PPR provided with a vibro-impact system (VIS), which was proven to be sometimes chaotic. The procedure aims to maximize the dissipation energy and minimize the number of impacts. Dispersion analyses of the periodic systems were performed for both the metafoundation and the metapipe. A stochastic linearization of the nonlinear hysteretic devices embedded in the metafoundation was necessary for the dispersion analysis. In the case of the metapipe, the bumpers that characterize the VIS are not physical characteristics of the metapipe, and thus the modal frequencies of the metapipe are not

affected by the external bumpers. The dispersion curves of both the metafoundation and the metapipe are shown. In the former, the maximum attenuation rate increases with an increase in the power spectral density (PSD) S_0 used to model the ground motions. Conversely, in the latter, the attenuation rate is increased by the structural damping. The dispersion curves are validated by the nonlinear FRF obtained via nonlinear transient analyses. In the case of the metapipe, a comparison with the numerical FRF of an FEM is also presented. Both systems have a strong attenuation capacity against stochastic loading thanks to the periodic orientation of the structures. Also, the optimization procedures played a central role in maximizing the seismic performance. For the metafoundation, the optimization had to be carried out after linearization because it pertained to a linear time-invariant system subjected to stationary seismic records, in the frequency domain. In the case of the metapipe, the design parameters of the fully nonlinear and sometimes chaotic VIS are optimized by employing response surfaces generated through Kriging modeling with a Gaussian 2nd order-polynomial regression.

6.2 Outlook

To summarize, this thesis explores the potential of nonlinear metamaterials and metastructures in controlling and mitigating elastic waves. The validation of all the findings presented in this thesis through experimentation is of utmost significance. Hence, it is essential to tackle the challenges related to the accurate control of the nonlinearities involved, to open up new avenues for engineering the nonlinear metamaterials discussed in this thesis.

For instance, the identification procedure is proposed to identify the dispersion characteristics of, potentially, any periodic structure in which FB is a valid solution of the free oscillations. In this sense, realizing a linear reference substructure (RS) that includes the single unit cell excited at the boundaries with two simple actuators is conceptually trivial. However, physically realizing an RS with accurate control of parameters governing nonlinear terms remains a challenge, since it requires considering nonlinear behaviors such as hardening/softening in nonlinear oscillations, multi-resonances, disorder, and others. A detailed characterization of damping effects, although controlled by the imaginary wavenumber, is also a challenge.

Despite the difficulties in identifying nonlinearities, we have demonstrated their potential for controlling SAWs. In our novel proposed device, postbuckling is exploited to activate a switching mechanism that

improves the propagation of the SAWs for certain frequency ranges. However, wave reflection at the vertical edges of the PMMA plate and advanced accuracy in the precompression of beams are critical aspects to consider in further studies. Moreover, inducing precompression using a rigid top plate may create coupling with the beams, thereby invalidating the switching mechanism.

Overall, this thesis highlights the promising applications of metamaterials and metastructures in the field of structural mechanics and engineering, particularly with the potential use of finite lattice metafoundations and metapipes for large distributed systems subject to seismic excitation. Further investigations should validate these results through 3D physical characterization of hysteretic devices and analysis of nonlinear wave mechanisms through nonlinear spatial analyses. Numerical transient analyses of multiple span PPRs could reveal periodic features of nonlinear, impacting, finite lattices.

A.0 Supplementary material to Chapter 2

In this Appendix, supplementary material to the work presented in Chapter 2 is reported. Appendix A.1 supports the developments of Section 2.4 by providing an analytical expression for the FRF of Eq. (2.17). Appendix A.2 reports a revised application of the subspace identification techniques (SSI) for identifying the linear and nonlinear stiffnesses of the reference subsystem presented in Fig. 2.1. Finally, Appendix A.3 reports on the parametric identification of the damping of a linear damped periodic metamaterial.

A.1 Definition of FRF for the nonlinear periodic system

We recall the system of EOMs relevant to the periodic 1D chain shown in Fig. 2.1 (a):

$$\begin{cases} m\ddot{u}_n + k\big(2u_n - u_{n-1} - u_{n+1}\big) + k_R\big(u_n - u_R\big) \\ +k_{NL}(u_n - u_{n-1})^3 + k_{NL}(u_n - u_{n+1})^3 = 0, \\ m_R\ddot{u}_R + k_R\big(u_R - u_n\big) = 0. \end{cases} \tag{A.1}$$

Subsequently, following the Lindstedt–Poincaré method [173], we consider the following asymptotic expansions:

$$\begin{aligned} u_j &= u_j^{(0)} + \epsilon\, u_j^{(1)} + O\left(\epsilon^2\right), \\ u_R &= u_R^{(0)} + \epsilon\, u_R^{(1)} + O\left(\epsilon^2\right), \\ \omega &= \omega_{(0)} + \epsilon\, \omega_{(1)} + O\left(\epsilon^2\right), \end{aligned} \tag{A.2}$$

where $j = \{n-1, n, n+1\}$. Then, we introduce (A.2) into (A.1) and obtain

$$\epsilon^0 : \begin{cases} m\omega_{(0)}^2 u_n^{(0)} + k(2u_n^{(0)} - u_{n-1}^{(0)} - u_{n+1}^{(0)}) + k_R(u_n^{(0)} - u_R^{(0)}) = 0, \\ m_R\omega_{(0)}^2 u_R^{(0)} + k_R(u_R^{(0)} - u_n^{(0)}) = 0, \end{cases} \tag{A.3}$$

$$\epsilon^1 : \begin{cases} m\omega_{(0)}^2 u_n^{(1)} + k(2u_n^{(1)} - u_{n-1}^{(1)} - u_{n+1}^{(1)}) + k_R(u_n^{(1)} - u_R^{(1)}) \\ +2m\omega_{(0)}\omega_{(1)} u_n^{(0)} + k_{NL}[(u_n^{(0)} - u_{n-1}^{(0)})^3 + (u_n^{(0)} - u_{n+1}^{(0)})^3] = 0, \\ m_R\omega_{(0)}^2 u_R^{(1)} + k_R(u_R^{(1)} - u_n^{(1)}) + 2m_R\omega_{(0)}\omega_{(1)} u_R^{(0)} = 0. \end{cases} \tag{A.4}$$

The system of equations (A.3) represents the order ϵ^0 equations, whereas (A.4) represents the order ϵ^1 equations. Subsequently, we consider the following harmonic wave solution:

$$\begin{aligned} u_j^{(0)} &= \frac{U^{(0)}}{2}\, exp(ij\kappa d)\, exp(i\omega t) + \frac{U^{(0)^*}}{2}\, exp(-ij\kappa d)\, exp(-i\omega t), \\ u_R^{(0)} &= \frac{U_R^{(0)}}{2}\, exp(in\kappa d)\, exp(i\omega t) + \frac{U_R^{(0)^*}}{2}\, exp(-in\kappa d)\, exp(-i\omega t), \end{aligned} \tag{A.5}$$

where * denotes the complex conjugate, and $j = \{n-1, n, n+1\}$. Then, we apply the harmonic solution to (A.4) and obtain

$$\begin{cases} m m_R \omega_{(0)}^4 u_n^{(1)} + m k_R \omega_{(0)}^2 u_n^{(1)} + k m_R \omega_{(0)}^2 (2u_n^{(1)} - u_{n-1}^{(1)} - u_{n+1}^{(1)}) \\ + m_R k_R \omega_{(0)}^2 u_n^{(1)} + k_R (2u_n^{(1)} - u_{n-1}^{(1)} - u_{n+1}^{(1)}) = \\ = C_1\, exp(i\omega_{(0)} t)\, exp(in\kappa d) + C_3\, exp(3i\omega_{(0)} t)\, exp(3in\kappa d), \\ \\ m_R \omega_{(0)}^2 u_R^{(1)} + k_R (u_R^{(1)} - u_n^{(1)}) = C_{1,R}\, exp(i\omega t)\, exp(in\kappa d), \end{cases} \tag{A.6}$$

where the coefficients C_1 and C_3 are

$$\begin{aligned} C_1 &= (k k_R - m_R \omega_{(0)}^2 k) \Big[k k_R\, \omega_{(0)} \omega_{(1)} - \frac{3}{2} k_{NL} k_R \big(1 - \cos\kappa d\big)^2 \Big| U^{(0)} \Big|^2 \Big] U^{(0)} \\ &\quad + m_R\, \omega_{(0)} \omega_{(1)} \frac{k_R^2}{k_R - \omega_{(0)}^2 m_R}\, U^{(0)}, \\ C_3 &= \frac{1}{2} \frac{k_{NL} k_R}{k} (k_R - 9k\omega_{(0)}^2) \big(2\cos^3\kappa d + 3\cos^2\kappa d - 1\big) \big(U^{(0)}\big)^2, \\ C_{1,R} &= m_R\, k_R\, \omega_{(0)} \omega_{(1)}\, \frac{1}{k_R - \omega_{(0)}^2 m_R}\, U^{(0)}. \end{aligned} \tag{A.7}$$

More precisely, we consider $U^{(0)}\, U^{(0)^*} = \Big| U^{(0)} \Big|^2$ in (A.7). The forcing terms on the right-hand side of the first equation in (A.6) are secular; therefore, we determine that C_1 is equal to 0. We then apply the F–B boundary conditions on the left and right-hand bounds via controlled displacements to the $(n-1)^{th}$ and $(n+1)^{th}$ masses, respectively. Consequently, we can define the analytical expression of $\omega_{(1)}$, which corresponds to $\boldsymbol{FRF^{(1)}}$ in the form $\frac{U}{U_{left}}$. Finally, we obtain Eq. (2.17), i.e.

$$\boldsymbol{FRF^{(1)}} = \left(\frac{2\, m_R\, \omega_{(0)}\, \omega_{(1)} \left(k_R^2\, m_R + m\, k_R^2 - 2\, m\, k_R\, m_R\, \omega_{(0)}^2 + m\, m_R^2\, \omega_{(0)}^4 \right)}{3\, k_{NL}\, m \left(k_R - m_R\, \omega_{(0)}^2 \right)^2 [1 - exp(2i\kappa d)]^2 \left| U_{left} \right|^2} \right)^{\frac{1}{2}}. \tag{A.8}$$

It is easy to verify that the linear term $\boldsymbol{FRF^{(0)}}$ is obtained by substituting harmonic solutions (A.5) in the form of $\frac{U^{(0)}}{U_{left}}$ into (A.3).

A.2 Parametric identification based on subspace identification techniques

A vast literature deals with subspace identification (SSI) methods. See, among others, the late-'90s books by Van Overschee and De Moor [174] and Ljung [175] that represent two milestones in the subject. Clearly, they have also been used with success for nonlinear SI in structural dynamics [176, 177]; therefore, we decided to consider their application to nonlinear periodic systems.

SSI methods exploit QR factorisation and/or Singular Value Decomposition by means of oblique projections of the row space of matrices. The unknowns of the method are both the model order and the state-space matrices of a discrete time model in state-space, with s measurements, as follows:

$$\begin{cases} \boldsymbol{x}_{k+1} = \boldsymbol{A}\boldsymbol{x}_k + \boldsymbol{B}\boldsymbol{v}_k + \boldsymbol{w}_k, \\ \boldsymbol{y}_k = \boldsymbol{C}\boldsymbol{x}_k + \boldsymbol{D}\boldsymbol{v}_k + \boldsymbol{z}_k, \end{cases} \tag{A.9}$$

where, $\boldsymbol{x} \epsilon \mathrm{R}^n$, $\boldsymbol{y} \epsilon \mathrm{R}^l$ and $\boldsymbol{v} \epsilon \mathrm{R}^m$ are the state-space vector, the output vector and the input vector, respectively; $\boldsymbol{w}$ and $\boldsymbol{z}$ are the process and measurement vectors; $\boldsymbol{A} \epsilon \mathrm{R}^{nxn}$ and $\boldsymbol{B} \epsilon \mathrm{R}^{nxm}$ are the system and the input matrices; $\boldsymbol{C} \epsilon \mathrm{R}^{lxn}$ and $\boldsymbol{D} \epsilon \mathrm{R}^{lxm}$ are the output and the direct feedthrough matrix. The characters n, l and m symbolize the order of the system, the number of outputs and the number of inputs, respectively. The input and output data are collected in block Hankel matrices. To identify the unknown state-space matrices, we implemented the so-called "subid" algorithm developed by Van Overschee and De Moor published in [174].

Once the state-space matrices $\boldsymbol{A}, \boldsymbol{B}, \boldsymbol{C}$ and $\boldsymbol{D}$ have been identified, we need to transform the system from discrete to continuous. In this respect, we adopted the zero-order hold time conversion method [178], which assumes that the control inputs are piecewise constant over the sampling period. The corresponding time-invariant continuous system is described by the following state-space model,

$$\begin{cases} \dot{\boldsymbol{x}} = \boldsymbol{A}_c\, \boldsymbol{x} + \boldsymbol{B}_c\, \boldsymbol{v}, \\ \boldsymbol{y} = \boldsymbol{C}\, \boldsymbol{x} + \boldsymbol{D}\, \boldsymbol{v}. \end{cases} \tag{A.10}$$

Once the state-space matrices $\boldsymbol{A}_c, \boldsymbol{B}_c, \boldsymbol{C}$ and $\boldsymbol{D}$ are found, the so-called "extended" transfer function $\boldsymbol{H}_E(\omega)$ of the nonlinear system can be defined as,

$$\boldsymbol{Y}(\omega) = \boldsymbol{H}_E(\omega)\,\boldsymbol{V}(\omega) = \Big[\boldsymbol{D} + \boldsymbol{C}(i\omega\boldsymbol{I} - \boldsymbol{A}_c)^{-1}\,\boldsymbol{B}_c\Big]\boldsymbol{V}(\omega), \quad \text{(A.11)}$$

where $\boldsymbol{Y}(\omega)$ and $\boldsymbol{V}(\omega)$ are the Fourier transforms of the output and the input, respectively.

A.2.1 Nonlinear parametric identification

According to Marchesiello and Gandino [177], we can derive the unknown mechanical parameters, i.e., the linear stiffness k and the nonlinear k_{NL}, as follows. The system of EoM of a nonlinear system with h degrees of freedom reads,

$$\boldsymbol{M}\ddot{\boldsymbol{u}}(t) + \boldsymbol{C}\dot{\boldsymbol{u}}(t) + \boldsymbol{K}\boldsymbol{u}(t) + \sum_{j=1}^{p} \mu_j \boldsymbol{L}_{nj} g_j(t) = \boldsymbol{f}(t), \qquad \text{(A.12)}$$

where $\boldsymbol{M}, \boldsymbol{C}$ and $\boldsymbol{K}$ are the mass, damping and linear stiffness matrices, respectively; $\boldsymbol{u}(t)$ is the absolute displacement vector and $\boldsymbol{f}(t)$ the linear force vector. The nonlinear term is expressed as the sum of p components, each of them depending on the scalar nonlinear function g_j and on the scalar nonlinear parameter μ_j through the vector $\boldsymbol{L}_{nj}$; it is composed by only $1, 0$ or -1, depending on the location of the nonlinear element. The function g_j defines the class of nonlinearity. As we deal with a cubic restoring force, see Eq. (2.12), we can move the nonlinear term to the right-hand side, and consider the nonlinear force as an internal feedback force. The system parameters k and k_{NL} to be identified are contained in the invariant matrix $\boldsymbol{H}_E(\omega)$, as shown by (A.11). As a result, it is easy to derive the parameters k and k_{NL} from the estimated transfer function, see [176], as follows:

$$\boldsymbol{H}_E(\omega) = \Big[\boldsymbol{H} \quad \boldsymbol{H}\,\mu_1\boldsymbol{L}_{n1} \quad \ldots \quad \boldsymbol{H}\,\mu_p\boldsymbol{L}_{np}\Big], \qquad \text{(A.13)}$$

where $\boldsymbol{H}$ is the linear transfer function. For zero frequency, the estimated $\boldsymbol{H}_E$ finally becomes,

$$\boldsymbol{H}_E(\omega = 0) = \Big[\boldsymbol{K}^{-1} \quad \boldsymbol{K}^{-1}\,\mu_1\boldsymbol{L}_{n1} \quad \ldots \quad \boldsymbol{K}^{-1}\,\mu_p\boldsymbol{L}_{np}\Big], \qquad \text{(A.14)}$$

A.2.2 Application with a white noise input

Herein, we present the application of the SSI method applied to the RS depicted in Fig. 2.5 when the input is a white noise (WN). The boundary conditions are applied to the left- and right-side of the RS in the form of a zero-mean Gaussian random input whose root mean squares are $U_{left} = 20\,mm$ and $U_{right} = 10\,mm$, respectively, as reported in Fig. A.1. Fig. A.1 (a) depicts input and output of the undamped case,

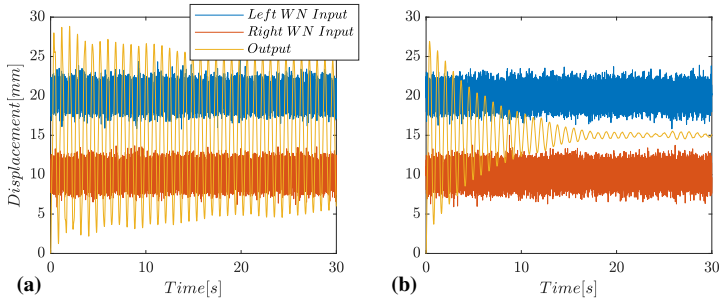

Figure A.1: Gaussian white noise displacements applied to the boundaries of the reference subsystem and relevant output: (a) undamped case, (b) damped case.

while Fig. A.1 (b) refers to the damped case. For clarity, the output response of the resonator is not shown, though it is included in the output vector and, therefore, in the Hankel matrix. To evaluate the effects of measurement noise, we added different levels of WN to the generated output, before the SI of the RS. Fig. A.2 shows one relevant simulation; in such instance, the output of the identified system agrees well with that of the original output. The added noise amounts to a certain percentage of the root mean square of the entire output. The errors associated to the identified parameters k and k_{NL} of the undamped RS after 100 simulations for each output noise level are collected in Tab. A.1. One may conclude that the involved errors are small. Similarly, mean and standard deviation of errors for the identification of the damped RS are listed in Tab. A.2 for the damped case. One may argue that also in this case the involved errors are small.

A.2.3 Application with Floquet-Bloch conditions

The identification of periodic nonlinear systems by means of the SSI ideally requires both a rich frequency content of the input and of the amplitude [179]. To meet these requirements while keeping a harmonic excitation to guarantee the application of FB boundary conditions, we

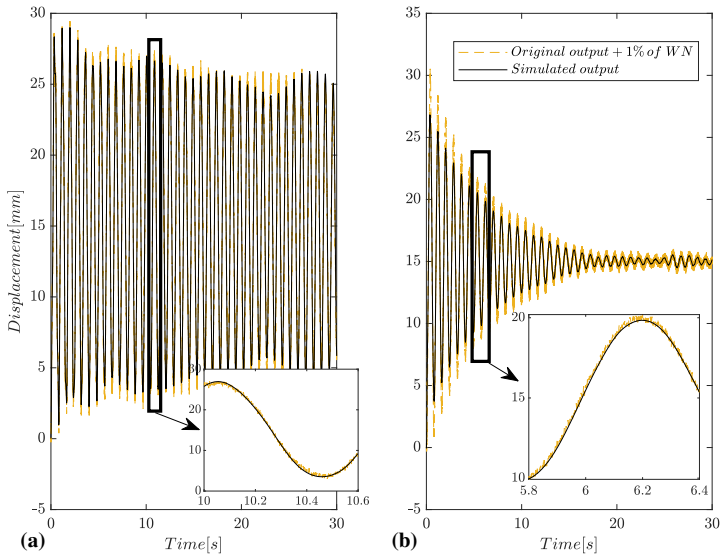

Figure A.2: Comparison between outputs of the identified model and of the original output: (a) undamped case, (b) damped case.

considered a harmonic input corrupted with a Gaussian WN and shifted to a non-zero mean value U_{left}, i.e.,

$$u_{left} = U_{left} + U_{left}\, exp(i\bar{\omega}t),$$
$$u_{right} = U_{left} + (u_{left} - U_{left})\, exp(2i\bar{\kappa}d). \tag{A.15}$$

An example is shown in Fig. A.3, for $U_{left} = 5\,mm$ and $\bar{\omega} = 10\,rad/s$. A careful reader can notice that the power spectral densities (PSDs) of both the original and modified signals remain essentially unchanged with a favourable frequency enrichment. Furthermore, the zoom-box shows that the addiction of the value U_{left} to the original excitation causes the PSD to increase at zero frequency due to the δ Dirac function.

Both results and relevant errors associated with the application of the SSI method are reported in Tab. A.3 and Tab. A.4 for the undamped and damped case, respectively. For these cases, we selected an amplitude $U_{left} = 5\,mm$ and three circular frequencies of the identified dispersion curves depicted in Fig. 2.7 and Fig. 2.10. The complex wavenumbers were also taken from the identified dispersion curves. We can argue that even in such instances identification errors are still limited. Clearly, the amount of errors can be further limited by a careful reduction of the SNR that characterizes the harmonic input and the added WN.

Noise [%]	Mean err (k_{ID})[%]	Std err (k_{ID})[%]	Mean err $(k_{NL,ID})$[%]	Std err $(k_{NL,ID})$[%]
0.1	0.008	0.001	0.751	0.090
0.3	0.009	0.005	1.071	0.206
0.5	0.009	0.008	1.793	0.404
1	0.051	0.015	5.175	0.870
2	0.078	0.024	16.687	1.540
3	0.082	0.031	31.936	1.720

Table A.1: Error values wrt the parameters k and k_{NL} after 100 simulations for each noise level in the undamped case.

Noise [%]	Mean err (k_{ID})[%]	Std err (k_{ID})[%]	Mean err $(k_{NL,ID})$[%]	Std err $(k_{NL,ID})$[%]
0.1	0.004	0.0006	0.761	0.491
0.3	0.008	0.006	2.932	1.639
0.5	0.011	0.009	7.357	2.230
1	0.015	0.015	14.451	3.920
2	0.039	0.023	39.350	6.142
3	0.091	0.026	73.344	10.053

Table A.2: Error values wrt the parameters k and k_{NL} after 100 simulations for each noise level in the damped case.

A.3 Damping identification for the linear periodic system

We assume in this case that the linear RS in Fig. 2.2 is damped, as depicted in Fig. A.4; only damping parameters c and c_R are unknown: all the mechanical characteristics of the relevant undamped periodic system have already been identified, see Eq. (2.9). Moreover, for the sake of generality, we consider both the case of non-classical damping and Rayleigh's proportional damping.

$\bar{\omega}$ [rad/s]	$\bar{\kappa}$ [rad/s]	Err k [%]	Err k_{NL} [%]
6	1.3+0.005i	1.233	3.490
16	1.4+3.217i	0.992	2.357
30	2.2+0.225i	1.814	4.004

Table A.3: Error values wrt the parameters k and k_{NL} for amplitudes $U_{left} = 5\,mm$ and $SNR = 20\,dB$, in the undamped case.

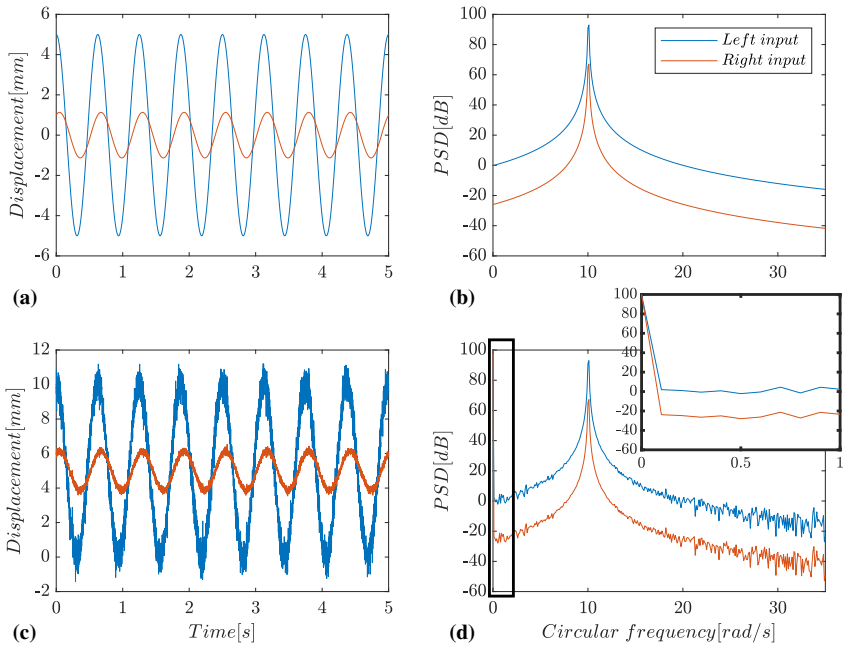

Figure A.3: Original input signals and modified signals to left and right of the RS and relevant power spectral densities (PSDs): (a) Original inputs; (b) PSDs of the original inputs; (c) Shifted inputs with WN; (d) PSDs of modified inputs.

$\bar{\omega}$ [rad/s]	$\bar{\kappa}$ [rad/s]	Err k [%]	Err k_{NL} [%]
6	1.3+0.037i	1.151	3.040
16	1.9+3.111i	0.855	1.961
30	1.9+1.546i	0.670	2.004

Table A.4: Error values wrt the parameters k and k_{NL} for amplitudes $U_{left} = 5\,mm$ and $SNR = 20\,dB$, in the damped case.

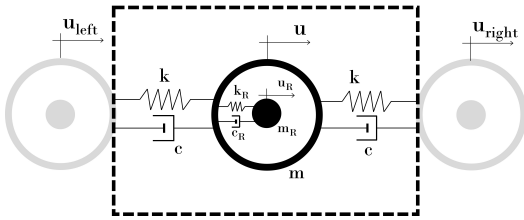

Figure A.4: RS for a linear resonant 1D chain provided with non-classical damping.

Fig. A.4 depicts the linear damped RS. The relevant system of EoM

reads,

$$\begin{cases} m\ddot{u} + c\big(2\dot{u} - v_{left} - v_{right}\big) + k\big(2u - u_{left} - u_{right}\big) + \\ c_R\big(\dot{u} - \dot{u}_R\big) + k_R\big(u - u_R\big) = 0, \\ \\ m_R\ddot{u}_R + c_R\big(\dot{u}_R - \dot{u}\big) + k_R\big(u_R - u\big) = 0. \end{cases} \tag{A.16}$$

where m and m_R are masses, k and k_R linear elastic constant stiffnesses, u and u_R absolute displacements and c and c_R the damping parameters to be identified. The dot represents the derivative with respect to time. The FB boundary conditions (2.6) and (2.7) are applied on u_{left} and u_{right}. In the damped case, also v_{left} and v_{right} are inputs involved. An analytical expression of the FRF is obtained after a few manipulations on (A.16), i.e.,

$$FRF_d = \frac{U}{U_{left}} = \frac{(i\omega c + k)(1 + e^{2i\kappa d})}{-m\omega^2 + 2i\omega c + 2k + i\omega c_R - \frac{-c_R^2\omega^2 + 2i\omega c_R k_R + k_R^2}{-m_R\omega^2 + i\omega c_R + k_R} + k_R}, \tag{A.17}$$

where U and U_{left} are the amplitudes of output and input, respectively, and d is the distance between cells. For completeness, the corresponding formula for the undamped FRF reads,

$$FRF_u = \frac{U}{U_{left}} = \frac{k\,(1 + e^{2i\kappa d})}{-m\omega^2 + 2k - \frac{k_R^2}{k_R - m_R\omega^2} + k_R}. \tag{A.18}$$

The dispersion law of the discrete periodic system can be easily obtained by means of the FB theorem applied to (A.16) and the condensation of the resonator DoF. It reads,

$$\kappa = Cos^{-1}\left(\frac{-m\omega^2 + 2i\omega c + 2k + i\omega c_R - \frac{-c_R^2\omega^2 + 2i\omega c_R k_R + k_R^2}{-m_R\omega^2 + i\omega c_R + k_R} + k_R}{2k + 2i\omega c}\right) \Big/ d. \tag{A.19}$$

Then, from Eq. (2.3) one can define the FRF for a damped system,

$$\Big|\frac{U}{U_{left}}\Big| = \big|exp(i\kappa_r d - \kappa_i d)\big| < 1. \tag{A.20}$$

Both (A.17) and (A.20) coincide when (A.17) is evaluated for the couples (κ, ω) that satisfy the dispersion law. Owing to the presence of κ_i, (A.20) is less then 1. In such instance, the following flowchart summarizes the main steps of the identification procedure.

A careful reader can note that the aforementioned SI procedure differs from the one presented in Section 2.4; nonetheless, the analytical

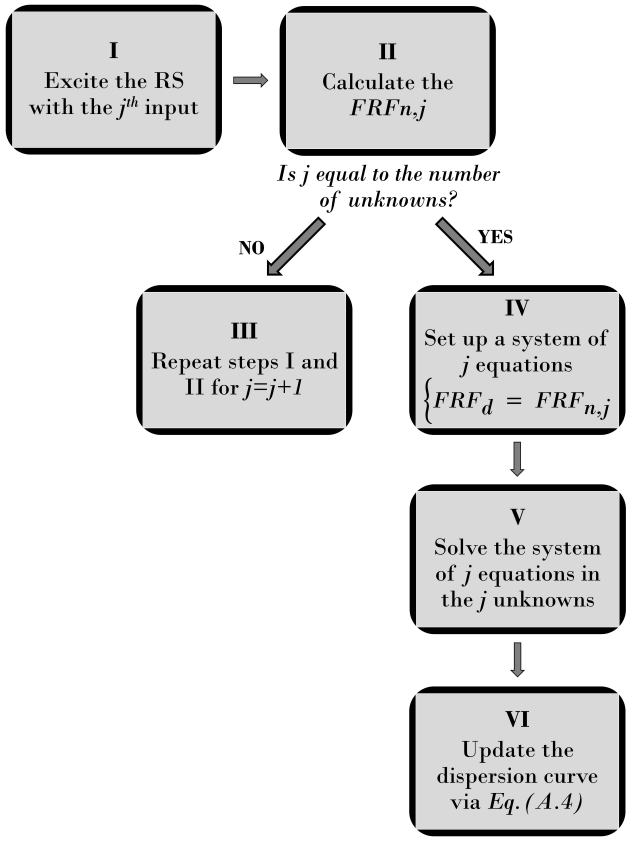

Figure A.5: Flowchart of the identification procedure of a linear resonant damped 1D discrete system.

expression (A.17) available for the linear case avoids any possible iteration.

Let's turn now to a numerical application. For clarity, the mechanical properties of the experimentally-informed RS represented in Fig. A.4 are listed herein: $m = 2450$ kg, $k = 0.155$ MN/m, $m_R = 3170$ kg, $k_R = 1.08$ MN/m. The damping parameters targets of the identification process read $c = 929.83$ N·s/m and $c_R = 7.83 \cdot 10^3$ N·s/m, respectively.

In agreement with the **Steps I**,**II** and **III** of the flowchart in Fig. A.5, the procedure requires two outputs from the RS. In this respect, as input, we prescribe two identified modal pairs of the undamped system; in this respect, see Fig. 2.3 (c) of Section 2.3. The numerical integration of

(A.16) entails the following outputs

$$\begin{aligned} \left|FRF^{I}_{n,1}\right| &= 0.998, \\ \left|FRF^{I}_{n,2}\right| &= 0.242, \end{aligned} \tag{A.21}$$

where $FRF^{I}_{n,1}$ is a complex number that refers to the input $\bar{\kappa}_r = 1$ rad/m and $\bar{\omega}_{1,1} = 4.9$ rad/s, whereas $FRF^{I}_{n,2}$ refers to $\bar{\omega}_{1,2} = 28.6$ rad/s. Then, to set a system of two equations in the two unknowns c and c_R - **Step V** - we combine (A.17) with the two values of (A.21) - **Step IV** -, which are identified without any error. Finally, we use the identified physical parameters to update the dispersion law - **Step VI** - (A.19). The entailed dispersion law for both imaginary and real components of the wavenumber are plotted in Fig. A.6.

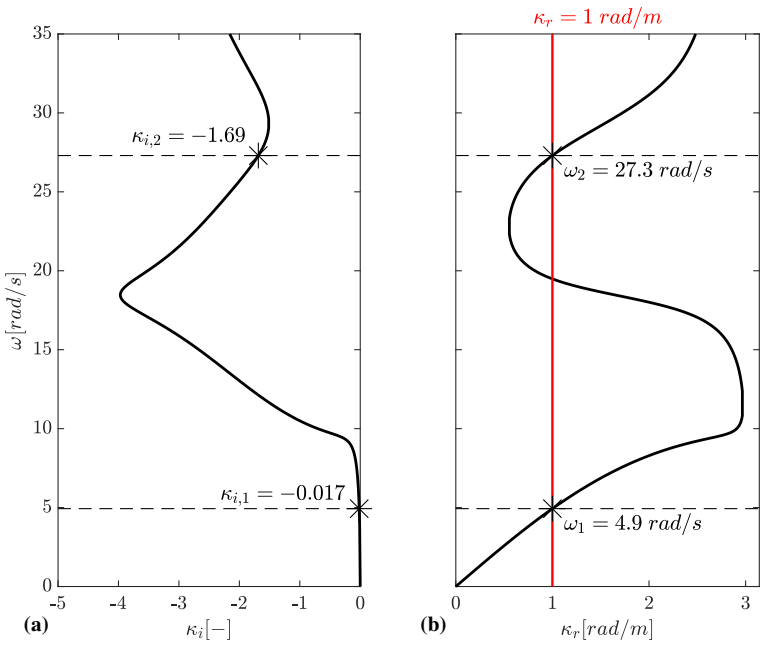

Figure A.6: Updated dispersion curves of the linear periodic damped periodic chain, (a) imaginary component of the wavenumber, (b) real component.

Nonetheless, note that the FRFs of (A.21) do not satisfy (A.20), because the input frequencies and wavenumbers do not belong to the dispersion curve. To run a test on the identified parameters and dispersion curve, the modal pairs $(\kappa_r,\, \omega)$ of Fig. A.6 (b) are employed, along with the corresponding imaginary components κ_i of Fig. A.6 (a), as input for a new simulation. We get,

$$\begin{aligned} \left|FRF^{II}_{n,1}\right| &= exp(-\kappa_{i,1} d) = 0.983, \\ \left|FRF^{II}_{n,2}\right| &= exp(-\kappa_{i,2} d) = 0.185, \end{aligned} \tag{A.22}$$

which now satisfy Eq. (A.20), as proved by the analytical FRFs depicted in Fig. A.7. Finally, a comparison between Fig. A.6 (b) and Fig. 2.3 (c)

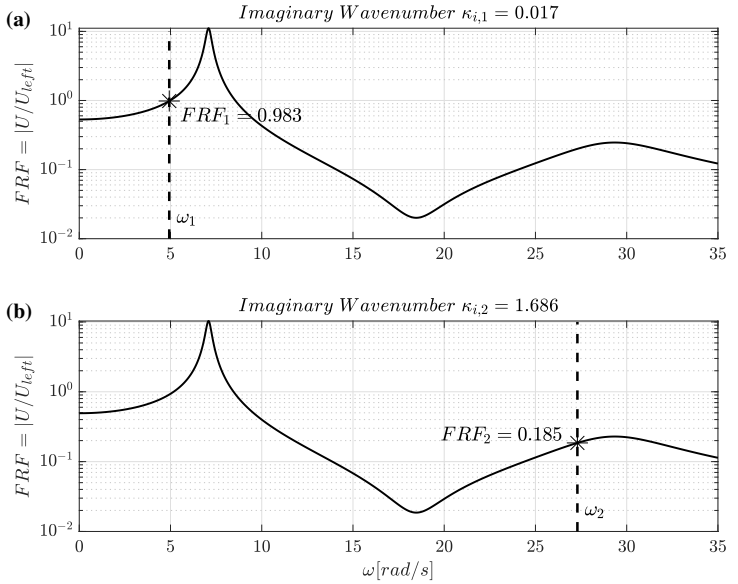

Figure A.7: Analytical FRFs of the linear damped chain evaluated for $\kappa_r = 1$ *rad/m and for: (a)* $\kappa_{i,1} = 0.017$*, (b)* $\kappa_{i,2} = 1.686$*.*

reveals a common property of periodic systems: in the dispersion curve of the damped system, just a slight change in the acoustic branch appears, wrt to the curve of the undamped system. Instead, a clearer change in the optical branch occurs.

As anticipated, also a SI procedure on a linear resonant metamaterial endowed with Rayleigh damping is carried out. To this end, the proportional Rayleigh damping matrix can be defined as,

$$\boldsymbol{C}_{pr} = p\boldsymbol{M} + q\boldsymbol{K} = p\begin{bmatrix} m & 0 \\ 0 & m_R \end{bmatrix} + q\begin{bmatrix} 2k + k_R & -k_R \\ -k_R & k_R \end{bmatrix}. \quad \text{(A.23)}$$

At the very least, we need to identify the coefficients p and q. All the other parameters belong to the RS of Fig. 2.2 and have been already identified, as outlined in Section 2.3.1. The system of EoM reads,

$$\boldsymbol{M}\ddot{u}(t) + \boldsymbol{C}_{pr}\dot{u}(t) + \boldsymbol{K}u(t) = f(t), \quad \text{(A.24)}$$

where $u(t)$ is the absolute displacement vector and the dot represents the derivative in time. The force vector $f(t)$ is a known term which contains the complex displacement fields u_{left} and u_{right}, and the velocities

v_{left} and v_{right}, respectively. A few manipulations of (A.24) lead to the analytical expression:

$$FRF_R = \frac{(i\omega q+1)\ k[1+exp(2i\kappa d)]}{-m\omega^2+i\omega pm+2k+2i\omega qk+i\omega qk_R+k_R-\frac{(i\omega qk_R+k_R)^2}{-m_R\omega^2+i\omega pm_R+i\omega qk_R+k_R}}. \tag{A.25}$$

The parametric ID method follows the same procedure conceived for the non-classical damping case, as described previously in this Appendix. The parameters to be identified read,

$$\begin{aligned} p &= 0.0804, \\ q &= 0.0048, \end{aligned} \tag{A.26}$$

which corresponds to modal damping ratios $\zeta_1 = 2\%$ and $\zeta_2 = 7\%$.
The modal pairs $(\kappa - \omega)$ of the undamped structure, see Section 2.3.1 and Fig. 2.3 (c), are adopted as input: $\kappa_r = 1$ rad/m, $\omega_{1,1} = 4.9$ rad/s and $\omega_{1,2} = 28.6$ rad/s. The FRFs are then computed as ratios between the amplitude U of the harmonic output and the amplitude U_{left} of the relevant input, i.e.,

$$\begin{aligned} \left|FRF^I_{nR,1}\right| &= 0.998, \\ \left|FRF^I_{nR,2}\right| &= 0.338, \end{aligned} \tag{A.27}$$

where $FRF^I_{nR,1}$ is a complex quantity that refers to the input $\kappa_r = 1$ rad/m and $\omega_{1,1} = 4.9$ rad/s; $FRF^I_{nR,2}$ refers instead to $\kappa_R = 1$ rad/m and $\omega_{1,2} = 28.6$ rad/s. Then, to deal with a system of two equations in the two unknowns p^{ID} and q^{ID}, the analytical formula of FRF_R expressed in (A.25) is inverted. As a result, the values of $FRF^I_{nR,1}$ and $FRF^I_{nR,2}$ of Eq. (A.27) are employed, and both p and q are exactly identified.

B.0 Supplementary material to Chapter 4

This Appendix supports the work reported in Chapter 4, specifically Subsection 4.2.2, and explains how the transmission matrix $H(\omega)$ is obtained for the SDoF resonator linked to the concrete slab by means of wire ropes depicted in Fig. 4.2 (b).

B.1 Calculation of the single resonator transmission matrix

In order to solve Eq. 4.12, we consider a Cauchy problem, whose solution reads,

$$z\left(t\right) = -c_{eq}e^{-k_{eq}t}\left(\int e^{k_{eq}t}\dot{u}\left(t\right)dt + c\right), \tag{B.1}$$

where c defines the integration constant. The value $c = 0$ derives from the initial conditions and . Then, if one replaces B.1 in both (4.4) and (4.5) obtains,

$$m\ddot{u}\left(t\right) + c\dot{u}\left(t\right) + \alpha k u\left(t\right) + \left(1-\alpha\right)ku_y\left[-c_{eq}e^{-k_{eq}t}\int e^{k_{eq}t}\dot{u}\left(t\right)dt\right] = F\left(t\right). \tag{B.2}$$

The conditions $u\left(t\right) = u_0 e^{i\omega t}$ and $F\left(t\right) = F_0 e^{i\omega t}$ entail

$$-\omega^2 u_0 e^{i\omega t}m + i\omega u_0 e^{i\omega t}c + \alpha u_0 e^{i\omega t}k + \left(1-\alpha\right)ku_y\left[-c_{eq}e^{-k_{eq}t}\int i\omega\ u_0 e^{k_{eq}t}e^{i\omega t}dt\right] = F_0 e^{i\omega t}. \tag{B.3}$$

As a result, the integral term in (B.3) can be solved as

$$\int i\omega\ u_0 e^{(i\omega+k_{eq})t}dt = \frac{i\omega}{i\omega+k_{eq}}u_0 e^{(i\omega+k_{eq})t}, \tag{B.4}$$

and, thus, (B.3) becomes,

$$-\omega^2 u_0 e^{i\omega t}m + i\omega u_0 e^{i\omega t}(d) + \alpha u_0 e^{i\omega t}k - \tfrac{i\omega}{i\omega+k_{eq}}c_{eq}\left(1-\alpha\right)ku_y u_0 e^{i\omega t} = F_0 e^{i\omega t}. \tag{B.5}$$

The transfer function $H(\omega)$ finally reads,

$$\mathrm{H}\left(\omega\right) = \left[-\omega^2 m + i\omega c + \alpha k - \frac{i\omega}{i\omega+k_{eq}}c_{eq}\left(1-\alpha\right)u_y\ k\right]^{-1}. \tag{B.6}$$

C.0 Supplementary material to Chapter 5

In this Appendix, supplementary material to Chapter 5 is reported. Appendix C.1 provides details of the analytical treatment of $\mathrm{PPR_f}$ dispersion curves depicted in Fig. 5.8; Appendix C.2 reports some comments and results of a few nonlinear transient analyses performed on the SS model depicted in Fig. 5.3.

C.1 Dispersion analysis of periodic damped $\mathrm{PPR_f}$

For the $\mathrm{PPR_f}$ and internal damping model, see Fig. 5.2 (a) and (c), the Euler-Bernoulli equation reads:

$$\frac{\partial^2}{\partial \mathrm{z}^2}\left[\mathrm{EJ}\frac{\partial^2 w(\mathrm{z,t})}{\partial \mathrm{z}^2}\right]+\frac{\partial^2}{\partial \mathrm{z}^2}\left[\mathrm{C}_i\frac{\partial^2 \frac{\partial w(\mathrm{z,t})}{\partial t}}{\partial \mathrm{z}^2}\right]+\rho A\frac{\partial^2 w(\mathrm{z,t})}{\partial \mathrm{t}^2}=0, \quad \text{(C.1)}$$

where ρ, E, A and *J* are, respectively, the material density, the Young modulus, the area and the inertia of the beam cross section. The term *w(z,t)* is the beam transversal displacement. C_i is the internal damping coefficient. Instead, for an externally damped $\mathrm{PPR_f}$, see Fig. 5.2 (a) and (d), the Euler-Bernoulli equation reads:

$$\frac{\partial^2}{\partial z^2}\left[\mathrm{EJ}\frac{\partial^2 w(z,t)}{\partial z^2}\right]+\mathrm{C}_e\frac{\partial w(z,t)}{\partial t}+\rho A\frac{\partial^2 w(z,t)}{\partial t^2}=0, \quad \text{(C.2)}$$

where $\mathrm{C_e}$ is the external damping coefficient. In Eqs. (C.1) and (C.2), the damping coefficients read:

$$\mathrm{C}_i=\frac{2\zeta_i \mathrm{EJ}}{\omega}, \quad \text{(C.3)}$$

$$\mathrm{C}_e=2\zeta_e \rho A\omega, \quad \text{(C.4)}$$

where $\zeta_{i/e}$ is the damping ratio, *i/e* specifies internal or external damping, and ω is the circular frequency. The free wave oscillations of the j^{th} support are expressed as:

$$\mathrm{w_j(z,t)}=\mathrm{w_0 e^{j\mu} e^{i\omega t}}=\mathrm{w_{0,j}(z) e^{i\omega t}}, \quad \text{(C.5)}$$

where μ is the propagation constant that is defined as

$$\mu=i\kappa L, \quad \text{(C.6)}$$

where κ is the wavenumber, L is the distance between the supports and i is the imaginary unit. From Eqs. (C.1) and (C.2) the following fourth-order ordinary differential equation can be derived, respectively, for the case of internal and external damping:

$$\mathrm{EI}\,\mathrm{w}^{\mathrm{IV}}(\mathrm{z}) + i\omega\ \mathrm{C}_i\mathrm{w}^{\mathrm{IV}}(\mathrm{z}) + \rho\mathrm{A}\omega^2\mathrm{w}(\mathrm{z}) = 0, \tag{C.7}$$

$$\mathrm{EI}\,\mathrm{w}^{\mathrm{IV}}(\mathrm{z}) + i\omega\,\mathrm{C_e}\mathrm{w}(\mathrm{z}) - \rho\mathrm{A}\omega^2\mathrm{w}(\mathrm{z}) = 0. \tag{C.8}$$

Both the equations can be rewritten in a compact form:

$$\mathrm{w}^{\mathrm{IV}}(\mathrm{z}) = {\Omega_i}^4\mathrm{w}(\mathrm{z}), \tag{C.9}$$

$$\mathrm{w}^{\mathrm{IV}}(\mathrm{z}) = {\Omega_\mathrm{e}}^4\mathrm{w}(\mathrm{z}), \tag{C.10}$$

where $\Omega_{i/e}$ is differently defined for internal and external damping, as follows:

$$\Omega_i = \frac{\rho\mathrm{A}\omega^2}{\mathrm{EI} + i\omega\,\mathrm{C}_i}, \tag{C.11}$$

$$\Omega_\mathrm{e} = \frac{\rho\mathrm{A}\omega^2 + i\omega\,\mathrm{C_e}}{\mathrm{EI}}. \tag{C.12}$$

The solution to Eqs. (C.7) and (C.8) is:

$$\mathrm{w}(\mathrm{z}) = \mathrm{A}_1\cos(\Omega_{\mathrm{i/e}}\mathrm{z}) + \mathrm{A}_2\sin(\Omega_{\mathrm{i/e}}\mathrm{z}) + \mathrm{A}_3\cosh(\Omega_{\mathrm{i/e}}\mathrm{z}) + \mathrm{A}_4\sinh(\Omega_{\mathrm{i/e}}\mathrm{z}). \tag{C.13}$$

Hence, Floquet-Bloch conditions in terms of transversal displacement and rotation are applied to each side - *l/r* - of the j^{th} support as,

$$\begin{aligned}
\mathrm{w}_{\mathrm{j+1}} &= \mathrm{w}_\mathrm{j}\mathrm{e}^{\mu},\\
\mathrm{w}_{\mathrm{j\text{-}1}} &= \mathrm{w}_\mathrm{j}\mathrm{e}^{-\mu},\\
\phi^{\mathrm{l}}_{\mathrm{j+1}} &= \phi^{\mathrm{l}}_\mathrm{j}\mathrm{e}^{\mu},\\
\phi^{\mathrm{l}}_{\mathrm{j\text{-}1}} &= \phi^{\mathrm{l}}{}_\mathrm{j}\mathrm{e}^{-\mu},\\
\phi^{\mathrm{r}}_{\mathrm{j+1}} &= \phi^{\mathrm{r}}_\mathrm{j}\mathrm{e}^{\mu},\\
\phi^{\mathrm{r}}{}_{\mathrm{j\text{-}1}} &= \phi^{\mathrm{r}}_\mathrm{j}\mathrm{e}^{-\mu},
\end{aligned} \tag{C.14}$$

where *l* and *r* mean left and right side, respectively. To compute the constants in Eq. (C.13) we apply the kinematic compatibility and equilibrium conditions at the j^{th} support. Such conditions lead to a system of linear homogeneous equations [180] in terms of transversal displacement w_j and rotation at the right side ϕ^r_j of the support. After obtaining the *2x2* matrix representing the system and setting its determinant to be

non-zero, the dispersion relation of a periodic piping system supported by flexible springs is obtained as,

$$\psi_{\mathrm{i/e}}\cosh^2(\mu_{\mathrm{i/e}}) + \chi_{\mathrm{i/e}}\cosh(\mu_{\mathrm{i/e}}) + \eta_{\mathrm{i/e}} = 0, \tag{C.15}$$

in which $\psi_{i/e}$ is defined as follows:

$$\psi_{\mathrm{i/e}} = [\cosh(\Omega_{\mathrm{i/e}}\mathrm{l}) - \cos(\Omega_{\mathrm{i/e}}\mathrm{l})]^2 - \sinh^2(\Omega_{\mathrm{i/e}}\mathrm{l}) - \sin^2(\Omega_{\mathrm{i/e}}\mathrm{l}), \tag{C.16}$$

and where $\chi_{i/e}$ and $\eta_{i/e}$ are:

$$\begin{aligned}\chi_{i/e} = [&\{\sinh(\Omega_{i/e}\mathrm{l}) - sin(\Omega_{i/e}\mathrm{l})\}\{\cosh(\Omega_{i/e}\mathrm{l})\, sin(\Omega_{i/e}\mathrm{l}) + cos(\Omega_{i/e}\mathrm{l})\sinh(\Omega_{i/e}\mathrm{l})\} \\ &- \{\cosh(\Omega_{i/e}\mathrm{l})\, sin(\Omega_{i/e}\mathrm{l}) - cos(\Omega_{i/e}\mathrm{l})\sinh(\Omega_{i/e}\mathrm{l})\}\{sin(\Omega_{i/e}\mathrm{l}) + \sinh(\Omega_{i/e}\mathrm{l})\} \\ &+ \frac{12\{\sinh(\Omega_{i/e}\mathrm{l}) - sin(\Omega_{i/e}\mathrm{l})\}\{1 - cos(\Omega_{i/e}\mathrm{l})\cosh(\Omega_{i/e}\mathrm{l})\}K_{v-m}\omega^2}{(\Omega_{i/e}\mathrm{l})^3}]\end{aligned} \tag{C.17}$$

$$\begin{aligned}\eta_{i/e} = [&\left\{\sin^2(\Omega_{i/e}\mathrm{l})\cosh^2(\Omega_{i/e}\mathrm{l}) - \cos^2(\Omega_{i/e}\mathrm{l})\sinh^2(\Omega_{i/e}\mathrm{l})\right\} - \left\{\cosh(\Omega_{i/e}\mathrm{l}) - \cos(\Omega_{i/e}\mathrm{l})\right\}^2 \\ &+ \frac{12\cosh(\Omega_{i/e}\mathrm{l})\ \sin(\Omega_{i/e}\mathrm{l}) - \cos(\Omega_{i/e}\mathrm{l})\sinh(\Omega_{i/e}\mathrm{l})\left\{1 - \cos(\Omega_{i/e}\mathrm{l})\cosh(\Omega_{i/e}\mathrm{l})\right\}K_v - m\omega^2}{(\Omega_{i/e}\mathrm{l})^3}].\end{aligned} \tag{C.18}$$

C.2 Some considerations about the transient analyses and the chaotic behavior

The transient analyses reported in this section were performed on the SS model depicted in Fig. 5.3, with *gap* = 64 mm and *COR* = 0.49, that is, Optimal solution 1. Fig. C.1 depicts the displacement responses, and the relevant Fourier transforms for the 7$^{\text{th}}$ ground motion of Tab. 5.2.

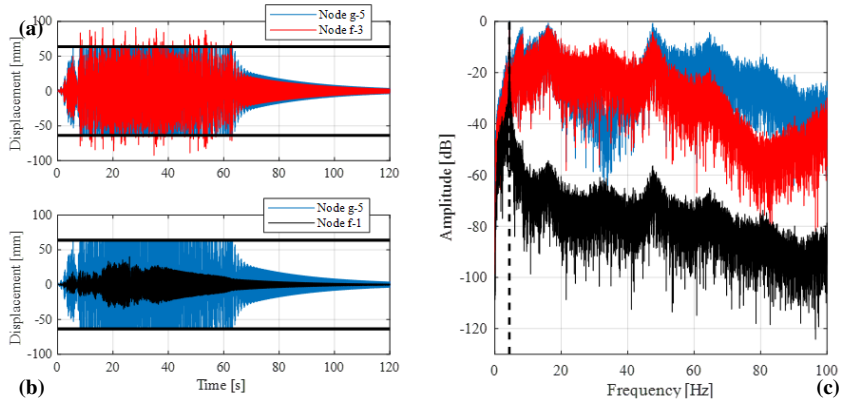

Figure C.1: Displacement x(t) of (a) Node g-5 and f-3, and (b) Node g-5 and f-1; (c) FRF of the three nodes. The black solid horizontal lines indicate the gap, whereas the vertical dashed line indicates the first natural frequency $\omega_{pr,1}$ of the system, see Fig. 5.8. The input is the 7th ground motion of Tab. 5.2.

Only the node *g-5* experiences the nonlinear boundary conditions, i.e., the amplitude constraints highlighted by solid black horizontal lines of Fig. C.1 (a) and (b). As expected, the impacts activate higher modes, see Fig. C.1 (c). However, these occurrences also affect the neighboring nodes. The amplitude of the vibrations of Node f-3, in fact, exceeds the *gap*, and the relevant *FRF* carries energy over the higher frequencies.

Fig. C.2 reports the results of further nonlinear transient analysis with single harmonic excitations.

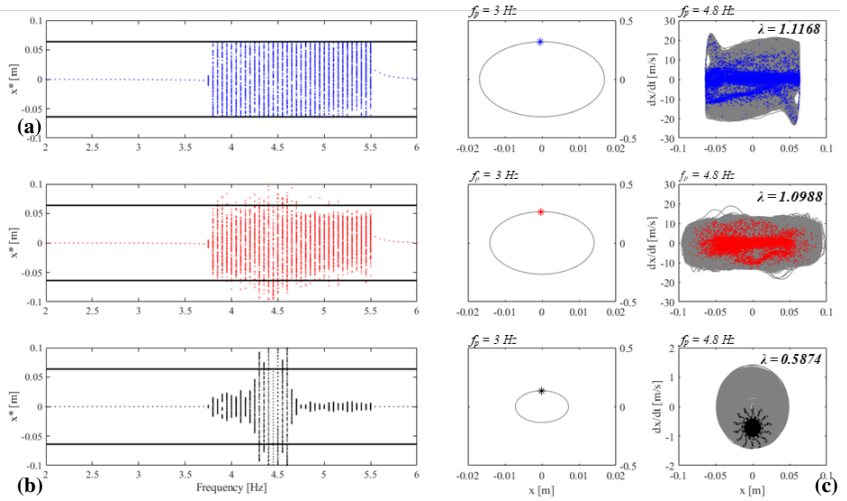

Figure C.2: From the left to the right-side, respectively: bifurcation diagrams, closed orbits for f_p = 3Hz, and phase portraits for f_p = 4.8 Hz of (a) Node g-5, (b) Node f-3, and (c) Node f-1. The stars in the closed orbits as well as the dots in the phase portraits report the Poincaré sections. In the phase portraits, the relevant largest Lyapunov exponents λ are reported.

In-depth characterization of the dynamics of the system requires single harmonic excitations with multiple amplitudes, since the dispersion features of a nonlinear system are amplitude and frequency dependent, and the nonlinear dynamics of the SS is beyond the scope of this paper. However, periodic forcing of the system has been considered for a limited range of frequencies, to test the existence of chaotic motion. The input acceleration reads , where $A_p = 3$ m/s^2 and f_p ranges from 2 to 6 Hz, and i is the imaginary unit. The bifurcation diagrams in Fig. B2 report the stable values x* that are approached asymptotically. When the impact does not occur, the system is linear and periodic, for example for $f_p = 3$ Hz; see Eqs. (5.12), (5.13) and (5.14). Whenever the impact occurs, as for f_p = *4.8* Hz, non-periodic solutions are found, and the attractors are chaotic. The nodes f-1 and f-3, that are not constrained,

also experience a chaotic response. We calculated the largest Lyapunov exponent λ of the trajectories of Fig. C.2 (a), (b) and (c), as follows:

$$\lambda_{\mathrm{i}} = \frac{1}{(K_{\max} - K_{\min} + 1)\mathrm{dt}} \sum_{K=K_{\min}}^{K_{\max}} \frac{\Lambda_{\mathrm{i,K}}}{K}, \tag{C.19}$$

where K_{min} and K_{max} represent the range of expansion used to estimate the local expansion rate and dt is the sampling time. $\Lambda_{i,K}$ is the logarithmic convergence or divergence of each point in the expansion range, and it reads:

$$\Lambda_{i,K} = \ln \frac{\|Y_{i,K} - Y_{i*,K}\|}{\|Y_i - Y_{i*}\|}, \tag{C.20}$$

where Y is the delayed reconstruction of the original signal, with an embedding dimension equal to 4 and a time lag equal to 8. The i indicates that the algorithm seeks for the nearest neighbor $i*$ that minimizes the denominator of Eq. (26) such that $|i\text{-}i*| \; 1/f_m$, where f_m is the mean frequency of the signal. For detailed information about the algorithm, see Rosenstein et al. [168]. We found the Lyapunov exponents λ for the nodes *g-5*, *f-3* and *f-1* to be equal to *1.1168*, *1.0988* and *0.5874*, respectively.

Bibliography

[1] Viktor G Veselago. The electrodynamics of substances with simultaneously negative values of ϵ and μ. *Soviet Physics Uspekhi*, 10(4):509, apr 1968. doi: 10.1070/PU1968v010n04ABEH003699. URL https://dx.doi.org/10.1070/PU1968v010n04ABEH003699.

[2] Katia Bertoldi, Pedro M Reis, Stephen Willshaw, and Tom Mullin. Negative poisson's ratio behavior induced by an elastic instability. *Advanced materials*, 22(3):361–366, 2010.

[3] Roderic S Lakes, T Lee, A Bersie, and Yun-Che Wang. Extreme damping in composite materials with negative-stiffness inclusions. *Nature*, 410(6828):565–567, 2001.

[4] Xiao-Ning Liu, Geng-Kai Hu, Guo-Liang Huang, and Chin-Teh Sun. An elastic metamaterial with simultaneously negative mass density and bulk modulus. *Applied physics letters*, 98(25):251907, 2011.

[5] Yiqun Ding, Zhengyou Liu, Chunyin Qiu, and Jing Shi. Metamaterial with simultaneously negative bulk modulus and mass density. *Physical review letters*, 99(9):093904, 2007.

[6] Ping Sheng, XX Zhang, Zhengyou Liu, and Che Ting Chan. Locally resonant sonic materials. *Physica B: Condensed Matter*, 338 (1-4):201–205, 2003.

[7] Myung Hwan Bae and Joo Hwan Oh. Amplitude-induced bandgap: New type of bandgap for nonlinear elastic metamaterials. *Journal of the Mechanics and Physics of Solids*, 139:103930, 2020.

[8] Bolei Deng, Pai Wang, Qi He, Vincent Tournat, and Katia Bertoldi. Metamaterials with amplitude gaps for elastic solitons. *Nature communications*, 9(1):1–8, 2018.

[9] Neel Nadkarni, Chiara Daraio, and Dennis M Kochmann. Dynamics of periodic mechanical structures containing bistable elastic elements: From elastic to solitary wave propagation. *Physical Review E*, 90(2):023204, 2014.

[10] Vicente Romero-García, A Krynkin, LM Garcia-Raffi, O Umnova, and Juan Vicente Sánchez-Pérez. Multi-resonant scatterers

in sonic crystals: Locally multi-resonant acoustic metamaterial. *Journal of Sound and Vibration*, 332(1):184–198, 2013.

[11] Romik Khajehtourian and Mahmoud I. Hussein. Dispersion relation for harmonic generation in nonlinear elastic waves. *The Journal of the Acoustical Society of America*, 151(4):A40–A40, 2022. doi: 10.1121/10.0010587. URL `https://doi.org/10.1121/10.0010587`.

[12] Raj K Narisetti, Michael J Leamy, and Massimo Ruzzene. A perturbation approach for predicting wave propagation in one-dimensional nonlinear periodic structures. *Journal of Vibration and Acoustics*, 132(3), 2010.

[13] Xin Fang, Jihong Wen, Jianfei Yin, Dianlong Yu, and Yong Xiao. Broadband and tunable one-dimensional strongly nonlinear acoustic metamaterials: Theoretical study. *Physical Review E*, 94(5):052206, 2016.

[14] Roberto Zivieri, Francesca Garesci, Bruno Azzerboni, Massimo Chiappini, and G Finocchio. Nonlinear dispersion relation in anharmonic periodic mass-spring and mass-in-mass systems. *Journal of Sound and Vibration*, 462:114929, 2019.

[15] Pierre Margerit, Arthur Lebée, Jean-François Caron, Kerem Ege, and Xavier Boutillon. The high-resolution wavevector analysis for the characterization of the dynamic response of composite plates. *Journal of Sound and Vibration*, 458:177–196, 2019.

[16] J Gregory McDaniel and W Steve Shepard Jr. Estimation of structural wave numbers from spatially sparse response measurements. *The Journal of the Acoustical Society of America*, 108(4):1674–1682, 2000.

[17] J Berthaut, MN Ichchou, and L Jezequel. K-space identification of apparent structural behaviour. *Journal of Sound and Vibration*, 280(3-5):1125–1131, 2005.

[18] Jia Liu and Katia Bertoldi. Bloch wave approach for the analysis of sequential bifurcations in bilayer structures. *Proceedings of the Royal Society A: Mathematical, Physical and Engineering Sciences*, 471(2182):20150493, 2015.

[19] Marc-Antoine Campana, Morvan Ouisse, Emeline Sadoulet-Reboul, Massimo Ruzzene, S Neild, and Fabrizio Scarpa. Impact

of non-linear resonators in periodic structures using a perturbation approach. *Mechanical Systems and Signal Processing*, 135: 106408, 2020.

[20] Sarah Benchabane, Abdelkrim Khelif, J-Y Rauch, Laurent Robert, and Vincent Laude. Evidence for complete surface wave band gap in a piezoelectric phononic crystal. *Physical Review E*, 73(6):065601, 2006.

[21] Oliver B Wright and Osamu Matsuda. Watching surface waves in phononic crystals. *Philosophical Transactions of the Royal Society A: Mathematical, Physical and Engineering Sciences*, 373 (2049):20140364, 2015.

[22] Younes Achaoui, Abdelkrim Khelif, Sarah Benchabane, Laurent Robert, and Vincent Laude. Experimental observation of locally-resonant and bragg band gaps for surface guided waves in a phononic crystal of pillars. *Physical Review B*, 83(10):104201, 2011.

[23] Alessandro Spadoni and Chiara Daraio. Generation and control of sound bullets with a nonlinear acoustic lens. *Proceedings of the National Academy of Sciences*, 107(16):7230–7234, 2010.

[24] EB Herbold, J Kim, VF Nesterenko, SY Wang, and C Daraio. Pulse propagation in a linear and nonlinear diatomic periodic chain: effects of acoustic frequency band-gap. *Acta Mechanica*, 205(1):85–103, 2009.

[25] N Boechler, J Yang, G Theocharis, PG Kevrekidis, and C Daraio. Tunable vibrational band gaps in one-dimensional diatomic granular crystals with three-particle unit cells. *Journal of Applied Physics*, 109(7):074906, 2011.

[26] Luca Bonanomi, Georgios Theocharis, and Chiara Daraio. Wave propagation in granular chains with local resonances. *Physical Review E*, 91(3):Art–No, 2015.

[27] Antonio Palermo, Yifan Wang, Paolo Celli, and Chiara Daraio. Tuning of surface-acoustic-wave dispersion via magnetically modulated contact resonances. *Physical Review Applied*, 11(4): 044057, 2019.

[28] Osama R Bilal, André Foehr, and Chiara Daraio. Bistable metamaterial for switching and cascading elastic vibrations. *Proceed-*

ings of the National Academy of Sciences, 114(18):4603–4606, 2017.

[29] Neil Boechler, Georgios Theocharis, and C Daraio. Bifurcation-based acoustic switching and rectification. *Nature materials*, 10 (9):665–668, 2011.

[30] Anne-Christine Hladky-Hennion and Michel de Billy. Experimental validation of band gaps and localization in a one-dimensional diatomic phononic crystal. *The Journal of the Acoustical Society of America*, 122(5):2594–2600, 2007.

[31] N Boechler, G Theocharis, Stéphane Job, Panayotis G Kevrekidis, Mason A Porter, and C Daraio. Discrete breathers in one-dimensional diatomic granular crystals. *Physical review letters*, 104(24):244302, 2010.

[32] Gaofeng Jia and Zhifei Shi. A new seismic isolation system and its feasibility study. *Earthquake Engineering and Engineering Vibration*, 9(1):75–82, 2010.

[33] ZB Cheng and ZF Shi. Composite periodic foundation and its application for seismic isolation. *Earthquake Engineering & Structural Dynamics*, 47(4):925–944, 2018.

[34] Tugberk Guner, Oreste S Bursi, and Silvano Erlicher. Optimization and performance of metafoundations for seismic isolation of small modular reactors. *Computer-Aided Civil and Infrastructure Engineering*, 2022.

[35] Vincenzo La Salandra, Moritz Wenzel, Oreste S Bursi, Giorgio Carta, and Alexander B Movchan. Conception of a 3d metamaterial-based foundation for static and seismic protection of fuel storage tanks. *Frontiers in Materials*, 4:30, 2017.

[36] Francesco Basone, Moritz Wenzel, Oreste S Bursi, and Marinella Fossetti. Finite locally resonant metafoundations for the seismic protection of fuel storage tanks. *Earthquake Engineering & Structural Dynamics*, 48(2):232–252, 2019.

[37] Andrea Franchini, Oreste S Bursi, Francesco Basone, and Feifei Sun. Finite locally resonant metafoundations for the protection of slender storage tanks against vertical ground accelerations. *Smart Materials and Structures*, 29(5):055017, 2020.

[38] Antonio Palermo, Sebastian Krödel, Alessandro Marzani, and Chiara Daraio. Engineered metabarrier as shield from seismic surface waves. *Scientific reports*, 6(1):1–10, 2016.

[39] Andrea Colombi, Rachele Zaccherini, Giulia Aguzzi, Antonio Palermo, and Eleni Chatzi. Mitigation of seismic waves: metabarriers and metafoundations bench tested. *Journal of Sound and Vibration*, 485:115537, 2020.

[40] DJ Colquitt, A Colombi, RV Craster, P Roux, and SRL Guenneau. Seismic metasurfaces: Sub-wavelength resonators and rayleigh wave interaction. *Journal of the Mechanics and Physics of Solids*, 99:379–393, 2017.

[41] Xingbo Pu, Antonio Palermo, Zhibao Cheng, Zhifei Shi, and Alessandro Marzani. Seismic metasurfaces on porous layered media: Surface resonators and fluid-solid interaction effects on the propagation of rayleigh waves. *International Journal of Engineering Science*, 154:103347, 2020.

[42] Giorgio Carta, Gian Felice Giaccu, and Michele Brun. A phononic band gap model for long bridges. the 'brabau'bridge case. *Engineering Structures*, 140:66–76, 2017.

[43] Mohd Iqbal, Mahesh Murugan Jaya, Oreste Salvatore Bursi, Anil Kumar, and Rosario Ceravolo. Flexural band gaps and response attenuation of periodic piping systems enhanced with localized and distributed resonators. *Scientific Reports*, 10(1):1–11, 2020.

[44] Zheng Lu, Zixin Wang, Ying Zhou, and Xilin Lu. Nonlinear dissipative devices in structural vibration control: A review. *Journal of Sound and Vibration*, 423:18–49, 2018.

[45] P Bin and PS Harvey Jr. A dual-mode floor isolation system to achieve vibration isolation and absorption: Experiments and theory. *Journal of Sound and Vibration*, 525:116757, 2022.

[46] Mohan M Murudi and Sharadchandra M Mane. Seismic effectiveness of tuned mass damper (tmd) for different ground motion parameters. In *13th World Conference on Earthquake Engineering*, volume 2, pages 1–8, 2004.

[47] Georgia Efthymiou and Christos Vrettos. Vibration reduction effects of pile group foundations during the passage of nearby moving surface loads. *3rd International Conference on Natural Hazards and Infrastructure*, ICONHIC, Athens 2022.

[48] Constantinos Kanellopoulos, Nikolaos Psycharis, Han Yang, Boris Jeremić, Ioannis Anastasopoulos, and Božidar Stojadinović. Seismic resonant metamaterials for the protection of an elastic-plastic sdof system against vertically propagating seismic shear waves (sh) in nonlinear soil. *Soil Dynamics and Earthquake Engineering*, 162:107366, 2022.

[49] Z Chatzopoulos, A Palermo, S Guenneau, and A Marzani. Cloaking strategy for love waves. *Extreme Mechanics Letters*, 50: 101564, 2022.

[50] Xingbo Pu, Antonio Palermo, and Alessandro Marzani. Lamb's problem for a half-space coupled to a generic distribution of oscillators at the surface. *International Journal of Engineering Science*, 168:103547, 2021.

[51] Xingbo Pu, Antonio Palermo, and Alessandro Marzani. A multiple scattering formulation for finite-size flexural metasurfaces. *Proceedings of the Royal Society A*, 478(2262):20210669, 2022.

[52] Xingbo Pu, Antonio Palermo, and Alessandro Marzani. Topological edge states of quasiperiodic elastic metasurfaces. *arXiv preprint arXiv:2205.00531*, 2022.

[53] R. Sabat, Y. Pennec, G. Lévêque, D. Torrent, C. Ding, and B. Djafari-Rouhani. Single and coupled helmholtz resonators for low frequency sound manipulation. *Journal of Applied Physics*, 132(6):064505, 2022.

[54] Marina E Kalogerakou, Konstantinos A Kapasakalis, Ioannis A Antoniadis, and Evangelos J Sapountzakis. Vertical seismic protection of structures with inerter-based negative stiffness absorbers. *Bulletin of Earthquake Engineering*, pages 1–42, 2022.

[55] Antonios G Mantakas, Konstantinos A Kapasakalis, Antonios E Alvertos, Ioannis A Antoniadis, and Evangelos J Sapountzakis. A negative stiffness dynamic base absorber for seismic retrofitting of residential buildings. *Structural Control and Health Monitoring*, 29(12):e3127, 2022.

[56] Moris Kalderon, Antonios Mantakas, Andreas Paradeisiotis, Ioannis Antoniadis, and Evangelos J Sapountzakis. Locally resonant metamaterials utilizing dynamic directional amplification: an application for seismic mitigation. *Applied Mathematical Modelling*, 2022.

[57] Panagiotis Koutsogiannakis, Davide Bigoni, and Francesco Dal Corso. Double restabilization and design of force–displacement response of the extensible elastica with movable constraints. *European Journal of Mechanics-A/Solids*, page 104745, 2022.

[58] Nikolin Hima, Francesco D'Annibale, and Francesco Dal Corso. Non-smooth dynamics of buckling based metainterfaces: Rocking-like motion and bifurcations. *International Journal of Mechanical Sciences*, page 108005, 2022.

[59] Kyriakos Alexandros Chondrogiannis, Vasilis Dertimanis, and Eleni Chatzi. Application of geometrically nonlinear metamaterial device forstructural vibration mitigation. In *Nonlinear Structures & Systems, Volume 1*, pages 109–118. Springer, 2023.

[60] Slimane Ouakka, Olivier Verlinden, and Georges Kouroussis. Railway ground vibration and mitigation measures: benchmarking of best practices. *Railway Engineering Science*, 30(1):1–22, 2022.

[61] Francesco Basone, Oreste S Bursi, Fabrizio Aloschi, and Günter Fischbach. Vibration mitigation of an mdof system subjected to stochastic loading by means of hysteretic nonlinear locally resonant metamaterials. *Scientific reports*, 11(1):1–15, 2021.

[62] Fabrizio Aloschi, Roberto Andreotti, and Oreste S. Bursi. Damped pipeline attenuation zones and optimal stochastic dynamic performance through an impact device. *submitted to Scientific reports*, 2022.

[63] Miltiadis Kontogeorgos and Clemente Fuggini. Meta-material layout for the protection of buried steel pipes against surface explosion. *Geotechnics*, 2(2):427–440, 2022.

[64] Maria Antoniou, Rallis Kourkoulis, Fani Gelagoti, and Ioannis Anastasopoulos. Simplified method for performance-based seismic design of suction caissons supporting jacket offshore wind turbines. *Soil Dynamics and Earthquake Engineering*, 155: 107169, 2022.

[65] Sebastian Krödel, Nicolas Thomé, and Chiara Daraio. Wide band-gap seismic metastructures. *Extreme Mechanics Letters*, 4:111–117, 2015.

[66] Mahmoud I Hussein, Michael J Leamy, and Massimo Ruzzene. Dynamics of phononic materials and structures: Historical origins, recent progress, and future outlook. *Applied Mechanics Reviews*, 66(4), 2014.

[67] Arnab Banerjee, Raj Das, and Emilio P Calius. Waves in structured mediums or metamaterials: a review. *Archives of Computational Methods in Engineering*, 26(4):1029–1058, 2019.

[68] Di Mu, Haisheng Shu, Lei Zhao, and Shuowei An. A review of research on seismic metamaterials. *Advanced Engineering Materials*, 22(4):1901148, 2020.

[69] LHMS Ribeiro, VF Dal Poggetto, BN Huallpa, and JRF Arruda. Bloch wavenumber identification of periodic structures using prony's method. *Mechanical Systems and Signal Processing*, 178:109242, 2022.

[70] Xin Fang, Jihong Wen, Bernard Bonello, Jianfei Yin, and Dianlong Yu. Wave propagation in one-dimensional nonlinear acoustic metamaterials. *New journal of physics*, 19(5):053007, 2017.

[71] Michael Stephen Patrick Eastham. *The spectral theory of periodic differential equations*. Scottish Academic Press [distributed by Chatto & Windus, London, 1973.

[72] Massimo Ruzzene, Fabrizio Scarpa, and Francesco Soranna. Wave beaming effects in two-dimensional cellular structures. *Smart materials and structures*, 12(3):363, 2003.

[73] Manuel Collet, Morvan Ouisse, Massimo Ruzzene, and MN Ichchou. Floquet–bloch decomposition for the computation of dispersion of two-dimensional periodic, damped mechanical systems. *International Journal of Solids and Structures*, 48(20): 2837–2848, 2011.

[74] L Junyi and DS Balint. An inverse method to determine the dispersion curves of periodic structures based on wave superposition. *Journal of Sound and Vibration*, 350:41–72, 2015.

[75] Jie Zhang, Edwin Reynders, Guido De Roeck, and Geert Lombaert. Model updating of periodic structures based on free wave characteristics. *Journal of Sound and Vibration*, 442:281–307, 2019.

[76] Leon Brillouin. *Wave propagation in periodic structures: electric filters and crystal lattices*, volume 2. Dover publications, 1953.

[77] A Srikantha Phani and Mahmoud I Hussein. *Dynamics of lattice materials*. John Wiley & Sons, 2017.

[78] Jorge J Moré. *The Levenberg-Marquardt algorithm: implementation and theory*. Springer, 1978.

[79] Chris Linton. *Wave Propagation. From Electrons to Photonic Crystals and Left-Handed Materials, by P. Markoš and CM Soukoulis: Scope: textbook. Level: final year undergraduates and first year postgraduates*. Taylor & Francis, 2009.

[80] Mihail Sigalas, Manvir S Kushwaha, Eleftherios N Economou, Maria Kafesaki, Ioannis E Psarobas, and Walter Steurer. Classical vibrational modes in phononic lattices: theory and experiment. *Zeitschrift für Kristallographie-Crystalline Materials*, 220(9-10): 765–809, 2005.

[81] LN Virgin and RH Plaut. Postbuckling and vibration of linearly elastic and softening columns under self-weight. *International Journal of Solids and Structures*, 41(18-19):4989–5001, 2004.

[82] Nan Hu and Rigoberto Burgueño. Buckling-induced smart applications: recent advances and trends. *Smart Materials and Structures*, 24(6):063001, 2015.

[83] Ali H Nayfeh, W Kreider, and TJ Anderson. Investigation of natural frequencies and mode shapes of buckled beams. *AIAA journal*, 33(6):1121–1126, 1995.

[84] Ali H Nayfeh and Samir A Emam. Exact solution and stability of postbuckling configurations of beams. *Nonlinear Dynamics*, 54: 395–408, 2008.

[85] Cyril Touzé, Alessandra Vizzaccaro, and Olivier Thomas. Model order reduction methods for geometrically nonlinear structures: a review of nonlinear techniques. *Nonlinear Dynamics*, 105(2): 1141–1190, 2021.

[86] Arthur Givois, Aurélien Grolet, Olivier Thomas, and Jean-François Deü. On the frequency response computation of geometrically nonlinear flat structures using reduced-order finite element models. *Nonlinear Dynamics*, 97(2):1747–1781, 2019.

[87] Bolei Deng, Yuning Zhang, Qi He, Vincent Tournat, Pai Wang, and Katia Bertoldi. Propagation of elastic solitons in chains of pre-deformed beams. *New Journal of Physics*, 21(7):073008, 2019.

[88] Florian Paul Robert Maurin and Alessandro Spadoni. Low-frequency wave propagation in post-buckled structures. *Wave Motion*, 51(2):323–334, 2014.

[89] Jack Ertle Oliver, Frank Press, and William Maurice Ewing. Two-dimensional model seismology. *Geophysics*, 19(2):202–219, 1954.

[90] Maria V Wilde, Mikhail V Golub, and Artem A Eremin. Experimental and theoretical investigation of transient edge waves excited by a piezoelectric transducer bonded to the edge of a thick elastic plate. *Journal of Sound and Vibration*, 441:26–49, 2019.

[91] Karl F Graff. *Wave motion in elastic solids*. Courier Corporation, 2012.

[92] D Bigoni, F Bosi, D Misseroni, F Dal Corso, and G Noselli. New phenomena in nonlinear elastic structures: from tensile buckling to configurational forces. *Extremely deformable structures*, pages 55–135, 2015.

[93] Steven L Garrett. *Understanding Acoustics: An Experimentalist's View of Sound and Vibration*. Springer Nature, 2020.

[94] Samuel P Wallen, Alexei A Maznev, and Nicholas Boechler. Dynamics of a monolayer of microspheres on an elastic substrate. *Physical Review B*, 92(17):174303, 2015.

[95] Davide Cardella, Paolo Celli, and Stefano Gonella. Manipulating waves by distilling frequencies: a tunable shunt-enabled rainbow trap. *Smart Materials and Structures*, 25(8):085017, 2016.

[96] Paolo Celli, Behrooz Yousefzadeh, Chiara Daraio, and Stefano Gonella. Bandgap widening by disorder in rainbow metamaterials. *Applied Physics Letters*, 114(9):091903, 2019.

[97] SJ Calhoun, MH Tehrani, and PS Harvey Jr. On the performance of double rolling isolation systems. *Journal of Sound and Vibration*, 449:330–348, 2019.

[98] Orazio Casablanca, G Ventura, F Garescì, Bruno Azzerboni, Bernardino Chiaia, Massimo Chiappini, and G Finocchio. Seismic isolation of buildings using composite foundations based on metamaterials. *Journal of Applied Physics*, 123(17):174903, 2018.

[99] AH Schellenberg, A Sarebanha, MJ Schoettler, G Mosqueda, G Benzoni, and SA Mahin. Hybrid simulation of seismic isolation systems applied to an apr-1400 nuclear power plant. *PEER Reports, Headquarters at the University of California*, 2015.

[100] Giorgio Carta, Alexander B Movchan, Luca P Argani, and Oreste S Bursi. Quasi-periodicity and multi-scale resonators for the reduction of seismic vibrations in fluid-solid systems. *International Journal of Engineering Science*, 109:216–239, 2016.

[101] Ministero dell'Interno e delle Infrastrutture. *Nuove norme tecniche per le costruzioni*. Decreto Ministeriale, 2018.

[102] F Paolacci and R Giannini. Study of the effectiveness of steel cable dampers for the seismic protection of electrical equipment. *Proceedings of 14th World Conference on Earthquake Engineering*, pages 12–17, 2008.

[103] S Alessandri, R Giannini, F Paolacci, and M Malena. Seismic retrofitting of an hv circuit breaker using base isolation with wire ropes. part 1: Preliminary tests and analyses. *Engineering Structures*, 98:251–262, 2015.

[104] P S Balaji, L Moussa, M E Rahman, and L H Ho. An analytical study on the static vertical stiffness of wire rope isolators. *Journal of Mechanical Science and Technology*, 30:287–295, 2016.

[105] Yi-Kwei Wen. Method for random vibration of hysteretic systems. *Journal of the engineering mechanics division*, 102(2):249–263, 1976.

[106] WJ Zhou, XP Li, YS Wang, WQ Chen, and GL Huang. Spectro-spatial analysis of wave packet propagation in nonlinear acoustic metamaterials. *Journal of Sound and Vibration*, 413:250–269, 2018.

[107] G Chakraborty and AK Mallik. Dynamics of a weakly non-linear periodic chain. *International Journal of Non-Linear Mechanics*, 36(2):375–389, 2001.

[108] Xin Fang, Jihong Wen, Bernard Bonello, Jianfei Yin, and Dianlong Yu. Ultra-low and ultra-broad-band nonlinear acoustic metamaterials. *Nature communications*, 8(1):1–11, 2017.

[109] Valentina Zega, Priscilla B Silva, Marc GD Geers, and Varvara G Kouznetsova. Experimental proof of emergent subharmonic attenuation zones in a nonlinear locally resonant metamaterial. *Scientific reports*, 10(1):1–11, 2020.

[110] Vivek Gupta, Sondipon Adhikari, and Bishakh Bhattacharya. Exploring the dynamics of hourglass shaped lattice metastructures. *Scientific reports*, 10(1):1–12, 2020.

[111] Thomas K Caughey. Equivalent linearization techniques. *The Journal of the Acoustical Society of America*, 35(11):1706–1711, 1963.

[112] Anil Kumar, Sandip Kumar Saha, and Vasant A Matsagar. Stochastic response analysis of elastic and inelastic systems with uncertain parameters under random impulse loading. *Journal of Sound and Vibration*, 461:114899, 2019.

[113] L Socha and M Pawleta. Are statistical linearization and standard equivalent linearization the same methods in the analysis of stochastic dynamic systems? *Journal of sound and vibration*, 248 (2):387–394, 2001.

[114] Praveen K Malhotra, Thomas Wenk, and Martin Wieland. Simple procedure for seismic analysis of liquid-storage tanks. *Structural engineering international*, 10(3):197–201, 2000.

[115] George W Housner. The dynamic behavior of water tanks. *Bulletin of the seismological society of America*, 53(2):381–387, 1963.

[116] Kiyoshi Kanai. Semi-empirical formula for the seismic characteristics of the ground. *Bulletin of the Earthquake Research Institute, University of Tokyo*, 35(2):309–325, 1957.

[117] W Clough, R, J Penzien, and S Griffin, D. Dynamics of structures. In *Engineering*, 1975.

[118] John C O'CALLAHAN. System equivalent reduction expansion process. In *Proc. of the 7th Inter. Modal Analysis Conf., 1989*, 1989.

[119] A Bonelli and OS Bursi. Generalized-α methods for seismic structural testing. *Earthquake engineering & structural dynamics*, 33(10):1067–1102, 2004.

[120] Michalakis C Constantinou and MA Adnane. *Evaluation of two models for yielding systems*. Drexel University, 1987.

[121] Gustavo Omar Maldonado. *Stochastic response of single degree of freedom hysteretic oscillators*. PhD thesis, Virginia Tech, 1987.

[122] Pol D Spanos and Agathoklis Giaralis. Third-order statistical linearization-based approach to derive equivalent linear properties of bilinear hysteretic systems for seismic response spectrum analysis. *Structural safety*, 44:59–69, 2013.

[123] Richard H. Bartels and George W Stewart. Solution of the matrix equation ax+ xb= c [f4]. *Communications of the ACM*, 15(9): 820–826, 1972.

[124] John Brian Roberts and Pol D Spanos. *Random vibration and statistical linearization*. Courier Corporation, 2003.

[125] Oreste S Bursi, Rocco di Filippo, Vincenzo La Salandra, Massimiliano Pedot, and Md S Reza. Probabilistic seismic analysis of an lng subplant. *Journal of Loss Prevention in the Process Industries*, 53:45–60, 2018.

[126] Ana Maria Cruz, Laura J Steinberg, and Ana Lisa Vetere-Arellano. Emerging issues for natech disaster risk management in europe. *Journal of Risk Research*, 9(5):483–501, 2006.

[127] Laura J Steinberg, Hatice Sengul, and Ana Maria Cruz. Natech risk and management: an assessment of the state of the art. *Natural Hazards*, 46(2):143–152, 2008.

[128] Douglas G Honegger, Douglas J Nyman, Elden R Johnson, Lloyd S Cluff, and Steve P Sorensen. Trans-alaska pipeline system performance in the 2002 denali fault, alaska, earthquake. *Earthquake spectra*, 20(3):707–738, 2004.

[129] Luigi Di Sarno and George Karagiannakis. On the seismic fragility of pipe rack—piping systems considering soil–structure interaction. *Bulletin of earthquake engineering*, 18(6):2723–2757, 2020.

[130] Oreste S Bursi, Fabrizio Paolacci, Md Shahin Reza, Silvia Alessandri, and Nicola Tondini. Seismic assessment of petrochemical piping systems using a performance-based approach. *Journal of Pressure Vessel Technology*, 138(3), 2016.

[131] Izumi Nakamura and Naoto Kasahara. Excitation tests on elbow pipe specimens to investigate failure behavior under excessive seismic loads. *Journal of Pressure Vessel Technology*, 139 (6), 2017.

[132] Izumi Nakamura, Akihito Otani, and Masaki Shiratori. Comparison of failure modes of piping systems with wall thinning subjected to in-plane, out-of-plane, and mixed mode bending under seismic load: an experimental approach. *Journal of pressure vessel technology*, 132(3), 2010.

[133] Fabian Dwenger, Klaus Kerkhof, Veit Birtel, and Thilo Froehlich. Experiments on seismic performance of piping mounted to a concrete floor by post-installed anchors. In *Pressure Vessels and Piping Conference*, volume 57034, page V008T08A019. American Society of Mechanical Engineers, 2015.

[134] Daniel G Gorman, Jason M Reese, and YL Zhang. Vibration of a flexible pipe conveying viscous pulsating fluid flow. *Journal of Sound and Vibration*, 230(2):379–392, 2000.

[135] L Enrique Ortiz-Vidal, Njuki W Mureithi, and Oscar MH Rodriguez. Vibration response of a pipe subjected to two-phase flow: Analytical formulations and experiments. *Nuclear Engineering and Design*, 313:214–224, 2017.

[136] Yu Zhang, Lei Sun, and Chao He. Flow induced vibration investigation of a main steam pipe suffering from high temperature steam flow. *Progress in Nuclear Energy*, 143:104040, 2022.

[137] Robert P Evans, Jonathan D Blotter, and Alan G Stephens. Flow rate measurements using flow-induced pipe vibration. *J. fluids Eng.*, 126(2):280–285, 2004.

[138] Michele Brun, Gian Felice Giaccu, AB Movchan, and NV Movchan. Asymptotics of eigenfrequencies in the dynamic response of elongated multi-structures. *Proceedings of the Royal Society A: Mathematical, Physical and Engineering Sciences*, 468 (2138):378–394, 2012.

[139] Feng Liang and Xiao-Dong Yang. Wave properties and band gap analysis of deploying pipes conveying fluid with periodic varying parameters. *Applied Mathematical Modelling*, 77:522–538, 2020.

[140] Huijie Shen, Michael P Païdoussis, Jihong Wen, Dianlong Yu, and Xisen Wen. The beam-mode stability of periodic functionally-graded-material shells conveying fluid. *Journal of Sound and Vibration*, 333(10):2735–2749, 2014.

[141] Leonard Meirovitch. *Principles and techniques of vibrations*, volume 1. Prentice Hall New Jersey, 1997.

[142] AL Kimball and DE Lovell. Internal friction in solids. *Physical Review*, 30(6):948, 1927.

[143] GB Song, P Zhang, LY Li, M Singla, D Patil, HN Li, and YL Mo. Vibration control of a pipeline structure using pounding tuned mass damper. *Journal of Engineering Mechanics*, 142 (6):04016031, 2016.

[144] Kaiming Bi and Hong Hao. Using pipe-in-pipe systems for subsea pipeline vibration control. *Engineering Structures*, 109:75–84, 2016.

[145] Abdullah Cheraghi and Seyed Mehdi Zahrai. Cyclic testing of multilevel pipe in pipe damper. *Journal of Earthquake Engineering*, 23(10):1695–1718, 2019.

[146] Seongkyu Chang, Weipeng Sun, Sung Gook Cho, and Dookie Kim. Vibration control of nuclear power plant piping system using stockbridge damper under earthquakes. *Science and Technology of Nuclear Installations*, 2016, 2016.

[147] Arnab Banerjee, Avishek Chanda, and Raj Das. Historical origin and recent development on normal directional impact models for rigid body contact simulation: a critical review. *Archives of Computational Methods in Engineering*, 24(2):397–422, 2017.

[148] Vitalyi Gusev, Hélène Bailliet, Pierrick Lotton, and Michel Bruneau. Interaction of counterpropagating acoustic waves in media with nonlinear dissipation and in hysteretic media. *Wave Motion*, 29(3):211–221, 1999.

[149] K Zhou, FR Xiong, NB Jiang, HL Dai, H Yan, L Wang, and Q Ni. Nonlinear vibration control of a cantilevered fluid-conveying pipe

using the idea of nonlinear energy sink. *Nonlinear Dynamics*, 95 (2):1435–1456, 2019.

[150] Ali Ebrahimi Mamaghani, SE Khadem, and Saeed Bab. Vibration control of a pipe conveying fluid under external periodic excitation using a nonlinear energy sink. *Nonlinear Dynamics*, 86(3):1761–1795, 2016.

[151] Vitor Schwenck Franco Maciel, Mojtaba Kheiri, and Guilherme Rosa Franzini. Passive suppression of flow-induced vibrations of a cantilevered pipe discharging fluid using non-linear vibration absorbers. *International Journal of Non-Linear Mechanics*, 144:104053, 2022.

[152] Tatiana Ueno and Guilherme Rosa Franzini. Numerical studies on passive suppression of one and two degrees-of-freedom vortex-induced vibrations using a rotative non-linear vibration absorber. *International Journal of Non-Linear Mechanics*, 116:230–249, 2019.

[153] Goro Kuwabara and Kimitoshi Kono. Restitution coefficient in a collision between two spheres. *Japanese journal of applied physics*, 26(8R):1230, 1987.

[154] Yutaka Tsuji, Toshitsugu Tanaka, and T Ishida. Lagrangian numerical simulation of plug flow of cohesionless particles in a horizontal pipe. *Powder technology*, 71(3):239–250, 1992.

[155] S Lo Feudo, Stéphane Job, Miriam Cavallo, Aguinaldo Fraddosio, Mario Daniele Piccioni, and Alessandro Tafuni. Finite contact duration modeling of a vibro-impact nonlinear energy sink to protect a civil engineering frame structure against seismic events. *Engineering Structures*, 259:114137, 2022.

[156] D Gugan. Inelastic collision and the hertz theory of impact. *American Journal of Physics*, 68(10):920–924, 2000.

[157] Ch Glocker. Concepts for modeling impacts without friction. *Acta Mechanica*, 168(1):1–19, 2004.

[158] SW Shaw. Forced vibrations of a beam with one-sided amplitude constraint: theory and experiment. *Journal of Sound and Vibration*, 99(2):199–212, 1985.

[159] Fulei Chu and Zhengsong Zhang. Bifurcation and chaos in a rub-impact jeffcott rotor system. *Journal of Sound and Vibration*, 210 (1):1–18, 1998.

[160] Dimitri Costa, Vahid Vaziri, Marcin Kapitaniak, Stephane Kovacs, Ekaterina Pavlovskaia, Marcelo A Savi, and Marian Wiercigroch. Chaos in impact oscillators not in vain: Dynamics of new mass excited oscillator. *Nonlinear Dynamics*, 102(2):835–861, 2020.

[161] Stefano Marelli and Bruno Sudret. *UQLab: A framework for uncertainty quantification in Matlab*. American Society of Civil Engineers, 2014.

[162] Timothy Simpson, Farrokh Mistree, John Korte, and Timothy Mauery. Comparison of response surface and kriging models for multidisciplinary design optimization. In *7th AIAA/USAF/-NASA/ISSMO Symposium on Multidisciplinary Analysis and Optimization*, page 4755, 1998.

[163] Enrica Bernardini, Seymour MJ Spence, Daniel Wei, and Ahsan Kareem. Aerodynamic shape optimization of civil structures: A cfd-enabled kriging-based approach. *Journal of Wind Engineering and Industrial Aerodynamics*, 144:154–164, 2015.

[164] Lei Zheng, Zonghui Liu, Hongwei Dang, Xin Guo, and Yonghua Wu. Seismic performance of super high-rise building structure with dual lines of defense based on response surface optimization algorithm. *Shock & Vibration*, 2022.

[165] Saber Moradi and Henry V Burton. Response surface analysis and optimization of controlled rocking steel braced frames. *Bulletin of Earthquake Engineering*, 16(10):4861–4892, 2018.

[166] Parishad Rahbari, Nadarajah Ravichandran, and C Hsein Juang. Seismic geotechnical robust design of cantilever retaining wall using response surface approach. *J GeoEng*, 12(4):147–155, 2017.

[167] Gerhard Venter, Raphael T Haftka, and James H Starnes Jr. Construction of response surface approximations for design optimization. *AIAA journal*, 36(12):2242–2249, 1998.

[168] Michael T Rosenstein, James J Collins, and Carlo J De Luca. A practical method for calculating largest lyapunov exponents from small data sets. *Physica D: Nonlinear Phenomena*, 65(1-2):117–134, 1993.

[169] Jack W Baker. Efficient analytical fragility function fitting using dynamic structural analysis. *Earthquake Spectra*, 31(1):579–599, 2015.

[170] Keith Porter, Robert Kennedy, and Robert Bachman. Creating fragility functions for performance-based earthquake engineering. *Earthquake Spectra*, 23(2):471–489, 2007.

[171] Dimitrios Vamvatsikos and C Allin Cornell. Incremental dynamic analysis. *Earthquake engineering & structural dynamics*, 31(3): 491–514, 2002.

[172] MA Hariri-Ardebili and VE Saouma. Probabilistic seismic demand model and optimal intensity measure for concrete dams. *Structural Safety*, 59:67–85, 2016.

[173] Ali H Nayfeh and Dean T Mook. *Nonlinear oscillations*. John Wiley & Sons, 2008.

[174] Peter Van Overschee and BL0888 De Moor. *Subspace identification for linear systems: Theory—Implementation—Applications*. Springer Science & Business Media, 2012.

[175] Lennart Ljung. *System identification*. Springer, 1998.

[176] Stefano Marchesiello and Luigi Garibaldi. A time domain approach for identifying nonlinear vibrating structures by subspace methods. *Mechanical Systems and Signal Processing*, 22(1):81–101, 2008.

[177] Edoardo Gandino and Stefano Marchesiello. Identification of a duffing oscillator under different types of excitation. *Mathematical Problems in Engineering*, 2010, 2010.

[178] Björn Wittenmark, Karl Johan Åström, and Karl-Erik Årzén. Computer control: An overview. *IFAC Professional Brief*, 1:2, 2002.

[179] Yuzhu Guo, Ling Zhong Guo, Stephen A Billings, and Hua-Liang Wei. Identification of nonlinear systems with non-persistent excitation using an iterative forward orthogonal least squares regression algorithm. *International Journal of Modelling, Identification and Control*, 23(1):1–7, 2015.

[180] Jie Tan, Siu Chun Michael Ho, Peng Zhang, and Jinwei Jiang. Experimental study on vibration control of suspended piping system

by single-sided pounding tuned mass damper. *Applied Sciences*, 9(2):285, 2019.

The mechanical and structural engineering community are increasingly resorting to the use of periodic metamaterials and metastructures to mitigate high amplitude vibrations; and nonlinearities are also an active area of research because they potentially provide different methods for controlling elastic waves. While the theory of propagation of linear elastic waves seems to be fairly complete and has led to remarkable discoveries in a variety of disciplines, there is still much to investigate about nonlinear waves, both in terms of their dispersion analytical description and their numerical characterization. This thesis mainly relies on the latter aspect and focuses on the analysis of nonlinear metamaterials and metastructures for both the mitigation and control of elastic waves. In particular, the thesis covers four main topics, each associated with a different nonlinearity: i) dispersion curves and mechanical parameters identification of a weakly nonlinear cubic 1D locally resonant metamaterial; ii) manipulation of surface acoustic waves through a postbuckling-based switching mechanism; iii) seismic vibration mitigation of a multiple-degrees-of-freedom system, the so-called metafoundation, by means of hysteretic nonlinear lattices; iv) seismic vibration mitigation of a periodic coupled system pipeline-pipe rack, by means of a vibro-impact system.

Fabrizio Aloschi